

UNIVERSITY OF OKLAHOMA  
GRADUATE COLLEGE

MACHINE LEARNING AND THE CONSTRUCTION OF A SEISMIC  
ATTRIBUTE-SEISMIC FACIES ANALYSIS DATA BASE

A THESIS  
SUBMITTED TO THE GRADUATE FACULTY  
in partial fulfillment of the requirements for the  
Degree of  
MASTER OF SCIENCE

By  
MURPHY CASSEL  
Norman, Oklahoma  
2018

MACHINE LEARNING AND THE CONSTRUCTION OF A SEISMIC  
ATTRIBUTE-SEISMIC FACIES ANALYSIS DATA BASE

A THESIS APPROVED FOR THE  
CONOCOPHILLIPS SCHOOL OF GEOLOGY AND GEOPHYSICS

BY

---

Dr. Kurt Marfurt, Chair

---

Mrs. Gerilyn Soreghan

---

Dr. John Pigott

© Copyright by MURPHY CASSEL 2018  
All Rights Reserved.

I dedicate this thesis to God, my family, friends, and dogs, Tortuga and Honey.



## **Acknowledgements**

Firstly, I would like to thank God for all his gifts. I was lead down a path full of different challenges that have prepared me for this accomplishment. I was able to finish this task and live the life given to me by him. Without Gods guidance and love I would not have the appreciation and love for life as I do now.

I would like to acknowledge my very committed advisor who helped me through this time with great patience, kindness and understanding. Dr. Marfurt lead me through some of my undergraduate and finally got me through my masters. He guided me through my educational career with great compassion and tenacity to leave me with as much knowledge as he could. I aspire to be as great of a scientist and mentor in the future.

To my committee members, Gerilyn Soreghan and John Pigott, I express my sincere appreciation for every ounce of knowledge they instilled in me. Without their guidance through my master's program I would not be where I am today. As well as my chair members I would like to thank all my educators that have guided me through this, Dr. Brad Wallet, Dr. Roger Slatt, Dr. Randy Keller, Dr. Shannon Dulin, Dr. Doug Elmore, Dr. Matthew Pranter, Dr. Shankar Mitra and to all my professors from undergraduate. I would also like to acknowledge the main office ladies, Ginny Gandy-Guedes, Ginger Leivas, Leah Moser, Ashley Tullius, Rebecca Fay, and Donna Mullins. They kept in line when it came to paperwork and due dates. I would also like to thank the various companies for their support and technologies; to Schlumberger for Petrel, to Marathon Oil and Gas for access to 3D seismic data, and to the sponsors AASPI research consortium.

Finally, I would like to thank with all my heart my family and friends. Without my families' love, compassion and drive I would not be where I am today. To my friends, David Lubo, Gabriel Machado, Emilio Torres, Saurabh Sinha, Javier Tellez, Thang Ha, Rafael Pires-De Lima, Folarin Kolawole, Abdulmohsen Alali, Cecilia Lopez-Gamundi, Tengfei Wu, Bin Lyu, Suriamin, Swetal Patel, David Duarte, Benmadi Milad, Sumit Verma, Lennon Infante, Allison Nepomnick, Sheridan Mullins and Joyce Stiehler. Thank you everyone for your help, guidance and advise.

# Table of Contents

Acknowledgements .....	iv
List of Tables .....	viii
List of Figures.....	x
Abstract.....	xvii
Chapter 1: Introduction.....	1
1.1 Outline .....	4
Chapter 2: Attribute Taxonomy.....	5
2.1 Overview of Attributes .....	5
Chapter 3. Multiattribute Application .....	12
3.1 Multiattribute Review.....	12
3.1.1 Interpreter Driven Workflows .....	13
3.1.2 Algorithmically (or machine-driven) workflows .....	14
3.2 Multiattribute Application .....	16
Chapter 4. Seismic Expression of Karst and Mass Transport Deposits .....	31
4.1 Karst Geologic Feature .....	31
4.1.1 Seismic Amplitude Expression of Karst Features .....	32
4.1.2 Seismic Attribute Expression of Karst Features .....	33
4.2 Mass Transport Deposits Feature .....	34
4.2.1 Seismic Amplitude Expression of Mass Transport Deposits Features .....	36
4.2.2 Seismic Attribute Expression of Mass Transport Deposits Features .....	38
Chapter 5. Web-Application .....	64

Chapter 6. Decision Tree Application	69
6.1 Decision Tree Overview	70
6.1.1 Random Forest Decision Tree Application	71
Chapter 7. Limitations and Conclusions	77
References	79
Appendix	84
Data Conditioning	84
Attribute Expression of a Mass Transport Deposit	88
Attribute Expression of a Karst	103

## List of Tables

<b>Table 1.</b> Barnes’ (2016) taxonomy containing three main categories for seismic attribute application. ....	9
<b>Table 2.</b> Marfurt’s (2018) taxonomy showing seven attribute families. ....	10
<b>Table 3.</b> A table of reflector configuration attributes that I will use in my web-based application for each seismic facies. Attributes that effectively differentiate some facies of interest will appear in a green box, those that are less generally effective in a yellow box, and those are generally of limited use in a white box. For each facies, clicking the box will display vertical and time slices through one or more data examples. ....	11
<b>Table 4.</b> In the left column Zhao’s et al. (2018) list of attributes useful in delineating karst features. The right column provides a geologic and/or a seismic imaging justification that a given attribute differentiates a karst feature from a background composed of laterally coherent, smoothly varying conformal reflectors .....	22
<b>Table 5.</b> Left side of table lists external and internal features seen in a karst environment. Right side of table lists attributes that quantify the internal configuration. ....	49
<b>Table 6.</b> Summary of the seismic attribute expression of karst collapse features seen the previous figures. ....	50
<b>Table 7.</b> Moscardelli and Wood (2008) description and classification of gravity flow MTDs seen in seismic data. ....	51
<b>Table 8.</b> A comparison of attached versus detached mass transport complexes characterized by the location and mechanism of slope failure (After Moscardelli and Wood, 2008). ....	52

**Table 9.** Left side of table details MTD seismic facies summation of external and internal features for facies identification. Right side of table lists attributes that quantify the internal configuration of the internal configuration. .... 62

**Table 10.** Summary of seismic attribute expression of the MTD seismic facies shown in the previous figures. .... 63

## List of Figures

- Figure 1.** Amtmann et al. (2013) data base of attributes provided by multiple technology suppliers. In this work they do not attempt to define which attribute might be “best” for a specific objective. .... 8
- Figure 2.** Vertical slices and a time slice at  $t= 1.80$  (s) through coherence, dip magnitude and dip azimuth volumes. Low coherence discontinuities appear black. A layer of conformal sediments dipping to the NE appears as magenta on the SW edge of the minibasin while those dipping to the SW appear as green on the NE side of the minibasin. The chaotic, rotated blocks within the MTD dip in all directions therefore the response is polychromatic, separated by low coherence. .... 18
- Figure 3.** 2D Histogram of the seismic attribute coherence and convergence magnitude highlighting the relationship between the two attributes with MTDs. The defined convergence (non-parallel) incoherent yellow polygonal voxels exhibiting incoherent reflections, representative of MTDs and salt shown in the next figure. .... 19
- Figure 4.** Such crossplots facilitate geobody extraction of MTDs and salt within the 3D seismic volume. Voxels (in yellow) defined by the polygon shown in the previous figure. .... 20
- Figure 5.** dGB’s OpenDtect’s subset of plugin applications that pre-selects the appropriate attributes to delineate specific seismic facies using a multilinear feed forward neural network. (dGB Earth Sciences, 2018). .... 21
- Figure 6.** Qi et al.’s (2016) workflow to identify the most useful attributes to differentiate salt, shale, and mass transport deposits. Highlighted in red, they compute histograms of the attribute distribution for each of the selected facies as a measure of

similar or dissimilar attribute response for each seismic facies discarding attributes that provide little discrimination. .... 23

**Figure 7.** Qi et al.'s (2016) seismic facies expression of salt, mass transport deposits and conformal sediments. Shown on the vertical slices along line B-B' and time slices at  $t=1.172$  s through seismic amplitude co-rendered with Kuwahara filtered attributes, (a) coherence, (b) magnitude of reflector convergence, (c) GLCM entropy, (d) GLCM dissimilarity, and (e) coherent energy. .... 24

**Figure 8.** Qi et al.'s (2016) 3D geobody of salt, mass transport complexes and conformal sediments obtained by drawing polygons on the 2D GTM latent space. Vertical slices along line B-B' and time slices at  $t=1.172$  s through (a) seismic amplitude and amplitude co-rendered (b) with salt facies (in red), (c) MTD facies (in yellow), (d) sediment facies (in green), and (e) with all three facies. .... 25

**Figure 9.** Vertical slices and a time slice at  $t= 1.80$  (s) through seismic amplitude volume with highlighted interpreted facies. Gray arrows and the yellow polygon areas identify MTDs within the seismic data volume. Surrounding the MTDs are conformal sediments, as well as salt diapirs creating the minibasins. Salt withdrawal formed minibasins resulting in sediment instability and mass transport deposits. .... 26

**Figure 10.** Vertical slices and a time slice at  $t= 1.80$  (s) through seismic coherence volume. This figure displays the same vertical slices as the previous figures. The gray arrows identify the MTD facies. The MTDs display low coherent values due to the large variation of sediment content and internal structures. .... 27

**Figure 11.** Vertical slices and a time slice at  $t= 1.80$  (s) through seismic total energy volume. The gray arrows identify the interpreted MTDs. The MTDs express high to low



chaotic energy responses. This is due to the varying sediment content of the MTDs. The conformal sediments express laterally extensive and layered low to moderate energy responses..... 28

**Figure 12.** A conceptual Venn diagram showing the observation that curvature artifacts are more likely to occur in areas that exhibit low energy and low coherence. In a decision tree, such a combination would indicate that any curvature anomalies in such an area are noise, rather than signal and should not be used for structural or stratigraphic analysis. .... 29

**Figure 13.** Loucks’ (2008) cartoon of karst features within the Ellenburger formation in Texas. This shows the type of faults that occur with karst as well as the type of fill, cave formation and sink holes. .... 39

**Figure 14.** Cross section of well logs with stratigraphic interpretation of the Woodford, Hunton and the Sylvan groups. The red arrow shows the karst feature as seen in the gamma ray log and in stratigraphic interpretation where there is a paleogeographic low allowing more accommodation space for the Woodford Shale to be deposited (Milad and Slatt, 2017)..... 40

**Figure 15.** Vertical slices and time slice at  $t=0.75s$  through the seismic volume. The teal polygons highlight the karst facies within the Ellenburger Formation. These facies display circular collapse features as well as faulting near the collapse clusters (Data courtesy of Marathon Oil Co.)..... 41

**Figure 16.** Vertical slice A-A’ through the seismic amplitude volume where the karst features from the previous figure are indicated by the gray arrows. The seismic amplitude cross section displays the karst show curved reflector expression and

polygonal faulting. The light gray arrow indicates a karst defined by polygonal faulting. The darker gray arrows indicate karst with a more curved reflector expression..... 42

**Figure 17.** Vertical slices through seismic amplitude volume and a phantom horizon 25 ms below the top of the Ellenburger formation through the seismic coherence volume.

The karst features exhibit a low coherence response and are structurally low..... 43

**Figure 18.** Vertical seismic amplitude slices and a phantom horizon 25 ms below the top of the Ellenburger formation through the corendered seismic coherence and

curvature volumes. Gray arrows indicate karst features. The vertical slices express the amplitude co-rendered with the most-positive and most-negative curvature to delineate the karst collapse features. The bowl-shaped karst features exhibit a strong negative .. 44

**Figure 19.** Horizon slice along the top Ellenburger formation through co-rendered dip azimuth and dip magnitude volumes. The karst features display high dip magnitude values as well as variable dip azimuth. Curvilinear faults strike toward the northeast.. 45

**Figure 20.** Vertical seismic amplitude slices and a phantom horizon 25 ms below the top of the Ellenburger formation through corendered seismic coherence and spectral magnitude volumes. Karst features display low spectral magnitude within the collapse feature. .... 46

**Figure 21.** Vertical seismic amplitude slices and a phantom horizon slice 25 ms below the top of the Ellenburger formation through the corendered seismic amplitude and GLCM dissimilarity volumes. Karst features display high dissimilarity values. .... 47

**Figure 22.** Vertical seismic amplitude slices and a phantom horizon slice 25 ms below the top of the Ellenburger formation through the corendered seismic amplitude and GLCM contrast volumes. Karst features exhibit high contrast values. .... 48

**Figure 23.** Vertical slices and a time slice at  $t=1.180$  s through the seismic amplitude volume. The MTDs exhibit chaotic reflectors within the structure as well as pinch out features at the toe of the MTD. The external features of the MTD include conformal sediment deposits both on the top and the bottom of the feature. .... 53

**Figure 24.** Vertical slices and a time slice at  $t=1.180$  s through the seismic amplitude and seismic coherence volume. The MTDs exhibit chaotic reflectors that are highlighted by low coherence. The salt exhibits the same coherence expression whereas the conformed sediments are high coherence..... 54

**Figure 25.** Vertical slices and a time slice at  $t=1.180$  s through corendered coherence, dip magnitude, and dip azimuth volumes. Low coherence discontinuities appear black. A layer of conformal sediments dipping to the NE appears as magenta on the SW edge of the minibasin while those dipping to the SW appear as green on the NE side of the minibasin. The chaotic, rotated blocks within the MTD dip in all directions so appear polychromatic, separated by low coherence discontinuities. .... 55

**Figure 26.** Vertical slices and a time slice at  $t=1.180$  s through corendered coherence, convergence magnitude, and convergence azimuth volumes. Low coherence values as well as chaotic convergence azimuth delineate the MTDs and the salt structures. The MTDs express variable convergence directions in the internal structure due to rotated blocks. The conformal sediments exhibit continuous convergence. The NW layered sediments converge toward the NE and the layers on the NE side of the minibasin converge SW. .... 56

**Figure 27.** Vertical slices and a time slice at  $t=1.180$  s through corendered coherence, convergence magnitude, and convergence azimuth volumes. Low coherence values as

well as chaotic convergence azimuth delineate the MTDs and the salt structures. The MTDs express variable convergence directions in the internal structure due to rotated blocks. The layered sediment exhibits continuous convergence. The NW conformal sediments converge toward the NE and the layers on the NE side of the minibasin converge SW. .... 57

**Figure 28.** Vertical slices and a time slice at  $t=1.180$  s through the corendered most-positive and most-negative curvature ( $k_1$  and  $k_2$ ) volumes. Gray arrows indicate MTDs. The MTDs display large variations in the internal structure with the response of  $k_1$  and  $k_2$  expressed throughout the feature. The salt diapirs respond with the strongest structural anomalies internally, but in general correspond to mismigrated noise. .... 58

**Figure 29.** Vertical slices and a time slice at  $t=1.180$  s through total energy volume. Gray arrows indicate MTD facies that exhibit high coherent energy. In contrast, the incoherent salt diapirs exhibit low total energy. .... 59

**Figure 30.** Vertical slices and a time slice at  $t=1.180$  s through corendered envelope and coherence volumes. Gray arrows indicate MTD facies which exhibit low to high envelope values. The conformal sediments and salt exhibit low envelope values. .... 60

**Figure 31.** Vertical slices and a time slice at  $t=1.180$  s through corendered GLCM homogeneity and amplitude volumes. The GLCM homogeneity attribute highlights chaotic features particularly well. The MTD facies exhibit low homogeneity response within the data. The salt diapirs exhibit the same expression as the MTD as they are variable internally. The conformal sediments display high homogeneity. .... 61

**Figure 32.** The legal language from the Wix website stating all intellectual property rights. .... 66

**Figure 33.** This is an image of the directory menu. The image reflects the lack of multiple internal directories..... 67

**Figure 34.** The menu of the seismicfacies.org website..... 67

**Figure 35.** This figure is a database diagram of the facies and the attributes that best suit them. At present, the only facies investigated in this thesis are karst and MTDs. More geologic features will be added in the future. .... 68

**Figure 36.** A simplified example of a decision tree to identify the root node, the internal nodes, and the leaf node. .... 74

**Figure 37.** A simplified decision tree for MTD identification within seismic datasets. The decision tree in this figure depicts the nature of a decision tree as well as the thought processes of a seismic interpreter to identify the geologic feature of interest utilizing seismic attributes. .... 75

**Figure 38.** A chart of the normalized features regarding the attributes. The best attribute identified by Kim (2018) are total energy, peak magnitude, chaos, RMS (root mean square) amplitude, absolute magnitude and GLCM entropy and homogeneity. .... 76

## **Abstract**

Currently, seismic facies and structural analysis requires a significant amount of time and effort by skilled interpreters. With the advances made by companies such as Amazon and Google with AI (artificial intelligence) and machine learning, many geoscientists (and perhaps more so, many geoscience managers) have identified the application of such technologies to the seismic interpretation workflow. Advancements of such technologies, such as machine learning based interpretation like self-organizing maps (SOM), principle component analysis (PCA) and independent component analysis (ICA), will both accelerate and quantify the seismic interpretation process.

Seismic attributes highlight subtle features in the seismic data that help identify architectural elements that can be used to further define the environment of deposition. Likewise, seismic attributes delineate subtle faults, folds, and flexures that better define the history of tectonic deformation. However, the understanding of “which attribute best illuminates which feature” requires either considerable experience or a tedious search process over years for published analogues. The objective of this thesis is to identify the seismic facies of interest through a prototype a web-based seismic attribute-seismic facies analysis database that can be used not only as a guide for human interpreters, but also to select attributes for machine learning. I propose a rule-based decision tree application that suggests which attributes are good candidates for machine learning applications.

There are many seismic facies. This thesis illustrates the objectives and a prototype web application using only two seismic facies: marine mass transport deposits and karst collapses. After initial validation, this product can then be improved and

expanded upon by a larger user community to provide an interactive attribute selection platform for interpreters at large.

## Chapter 1: Introduction

Taner (2003) noted that seismic attributes provide “qualitative information on geologic facies, geometry and rock physics”. Chopra and Marfurt (2007) stated that a “seismic attribute is any measure of seismic data that helps us visually enhance or quantify features of interest.” Barnes (2016) viewed attributes as “quantifying properties of seismic data that can then be interpreted to determine geologic relevance.” Overall, a good seismic attribute helps identify subtle features that might otherwise be overlooked, quantifies the seismic amplitude expression of geologic features of interest for both subsequent risk analysis and machine learning, and provides images that may be more easily understood by colleagues or business investors with limited experience in 3D interpretation of seismic amplitude volumes.

The first step in an attribute-assisted 3D seismic facies analysis is a conventional interactive interpretation of each target seismic facies on a few vertical and time slices through the seismic amplitude volume. The second step is to then identify which features internal to the target facies differentiate it from surrounding conformal, continuous reflectors. The third step is to then determine which attributes quantitatively measure these features.

The term facie was first coined by Gressly (1838) to describe the aspects or “faces” of a geologic terrain. Walker (1993) defines facies as “A body of rock characterized by particular combination of lithology, physical and biological structures that bestow an aspect different from the bodies of rock above, below and laterally adjacent.”



The term “seismic facies” is less precise than geologic facies and used by geophysicists (Alexander et al. 1985; Qi et al. 2017, Zhao et al. 2018; Marfurt, 2018) to describe the seismic expression of geologic features of interest. Seismic facies are mappable, three-dimensional seismic units composed of groups of reflections whose parameters differ from those of adjacent reflectors. Seismic facies analysis requires the description and interpretation of seismic reflection parameters including configuration, continuity, amplitude, and frequency within the stratigraphic framework of the depositional sequence unit. Seismic attributes measure these same reflection parameters and are key to quantifying the facies with machine learning. Barnes and Laughlin (2002) find that the choice of attributes is more important to effective machine learning than the machine learning algorithm used.

Pigott et al. (2013) identified two common analytical methods for attribute application. The first analysis method is *stochastic*, whereby the candidate seismic attributes are statistically correlated to a given geologic property or zone of interest. The stochastic approach requires an understanding of the attribute-to-facies relationship but can suffer from false positive correlations (Kalkomey, 1997). Pigott et al. (2013) found the stochastic analysis to be relatively fast, without requiring a deep understanding of the dataset; however, spurious seismic attribute correlations can lead to misinterpreting the geology. Modern “deep learning” algorithms based on convolutional neural networks are stochastic (Qi, 2018).

The second method is *deterministic* and involves more planning but may save the interpreter time and computational cost in the end. In the deterministic method, the interpreter has a predefined understanding of the geologic features of interest and has a

working knowledge of which attributes can be used to delineate relevant features within the basin (Pigott et al., 2013; Chopra and Marfurt, 2007). In general, the deterministic approach requires a deeper understanding of seismic attributes, the seismic expression of geologic features, and an appropriate depositional, diagenetic, or tectonic model. A pitfall of the deterministic analysis is “confirmation bias,” whereby we ignore alternative interpretations in favor of a preconceived geologic model and exploration objective (Infante-Paez, 2018; Posamentier, 2018).

The deterministic method requires background knowledge and either a skilled (more experienced) geoscientist, costing more money, or a less experienced interpreter, costing more time. My goal is to capture some of the knowledge of a skilled interpreter and create an attribute-to-seismic-facies database that is more accessible to an interpreter than using a general-purpose search engine to find published papers. Capturing this information and accessing it in a web-based application may not impart interpreter expertise but can be used to select a subset of attributes for subsequent stochastic evaluation based on their previous performance.

There are four advantages to a web-based system. First, a web-based system is not limited to a 2-dimensional table but rather can sort  $n$ -dimensional tables by seismic facies, by attribute, by depositional environment or (in a corporate environment) by exploration objective. Second, a web-based system can contain modern interactive capabilities such as animation, 3-dimensional rotation, fade-in overlays, and gliding options to give more dimension to the information that is not possible in printed media. A web-based application provides the links available to online publications, including attribute definitions, software documentation, and links to algorithmic details and

relevant case studies. Third, a web-based system can be linked to a decision tree whereby the interpreter examines features in the seismic data, compares it to similar features on the web site and then clicks candidate attributes to be computed and evaluates either interactively using 3D visualization, or as input to a machine learning algorithm. Fourth, and finally, a successful web-based application can grow into a “wiki,” providing a platform for enhanced information sharing.

### **1.1 Strategy**

I begin my thesis in Chapter 2 with a review of alternative seismic attribute taxonomies, providing a framework for a web-based application. Then, in Chapter 3, I briefly review modern practices in multi-attribute analysis, beginning with interactive 3D multi-attribute visualization, progressing into unsupervised classification, and ending with supervised machine learning algorithms. In chapter 4, I analyze two seismic facies: mass transport deposits and karst collapse features, defining not only their appearances on seismic amplitude data, but also their appearance on seismic attributes. To be useful, this suite of images should be as comprehensive as possible, including attributes that don't help differentiate the target feature from the background conformal, coherent reflectors. In chapter 5, I use these two examples to provide the data needed to populate my prototype web application. In chapter 6, I use this (highly pruned) decision tree to define which attributes should be considered for delineation of these two facies. I then insert these attribute volumes into modern machine learning algorithms developed by my colleagues at the University of Oklahoma. Finally, In Chapter 7 I conclude with a summary of my findings, assessing current limitations, and defining future steps towards building a more comprehensive attribute selection decision tree.

## **Chapter 2: Attribute Taxonomy**

The goal of this thesis is to build a more modern version of a seismic interpretation “attribute handbook,” focusing on only a few branches (seismic facies) (mass transport deposits and karst collapse) of the tree. My ultimate goal is to emulate Amtmann et al.’s (2013) software database and create web-based application that applies previous and current work that is user friendly and available to the public at large (Figure 1).

### **2.1 Overview of Attributes**

Seismic attribute application began in 1940s with sonograms and directional reception (Taner, 2003). The definition of a seismic attribute has changed from the 1970s and evolved from just seismic attribute application to seismic structural mapping, stratigraphic analysis, lithologic characterization and reservoir monitoring (Chen, 1997). Since the 1970s, the diversity of attributes and seismic attribute applications have expanded significantly. Although these attributes provide new methods to interpret seismic data, many interpreters feel they have too many choices. Interpreters commonly question which attribute to use to identify a given feature. There are few publications that identify this problem and even fewer that give a solution to the question, “Which attribute is best suited for my data?” This thesis is a step towards answering that question as it will cover which attributes can be used for specific seismic facies using a web-based decision tree for easy user application.

Chopra and Marfurt (2007) stated that a “seismic attribute is any measure of seismic data that helps us visually enhance or quantify features of interest.” Barnes (2016) views attributes as a means to quantifying properties of seismic data that can

then be interpreted to determine the geologic relevance. Taner (2003) noted that the study of seismic attributes is meant to give qualitative information on geologic facies, geometry and rock physics. Overall, seismic attributes are meant to help quantify geologic features that are not identified by the seismic amplitude data alone.

Barnes (2016) and Marfurt (2018) provided more recent taxonomies that emphasize structural, stratigraphic, or lithological properties of the subsurface geology (Tables 1 and 2). Barnes' (2016) *geologic* seismic attributes include lithological and reflection patterns which are subdivided into structural and stratigraphic subcategories. Structural seismic attributes include dip magnitude and dip azimuth, curvature, shape indices, aberrancy, reflector convergence and parallelism, and alternative measures of discontinuities and other fault indicators. The same structural attributes can be applied to stratigraphy, thereby mapping the discontinuity of channel edges, or the curvature expression of differential compaction, while spectral components provide measures of thickness within the structure. Barnes' (2016) *mathematical* attributes overlap with Marfurt's (2018) *textural* attributes and quantify statistical patterns within the data. Likewise, Barnes' (2016) *lithologic* attributes include Marfurt's (2018) impedance attributes. The work done in this thesis builds on these two taxonomies and present an applied taxonomy to the seismic facies studied in this work including karst and MTDs, where the emphasis envisions multiattribute machine learning as well as 3D multiattribute visualization.

In some cases, different attributes provide the same (or redundant) results (Barnes, 2007). Barnes (2017) also identifies attributes that are useless for geologic interpretation but have been retained in commercial software for historical reasons.

Selecting the best attributes is invaluable to the interpreter as it saves time and computational cost. Some attributes are easy to understand. Dip azimuth, dip magnitude, most-positive and most-negative curvature, and coherence (dissimilarity) are concepts fundamental to geologic mapping. Geomechanical attributes such as P-wave impedance, Poisson's ratio, and azimuthal anisotropy are also clearly defined. Attributes that are more statistical include root-mean-squared amplitude, chaos, parallelism, and gray level co-occurrence matrix texture attributes such as entropy (Marfurt, 2018).

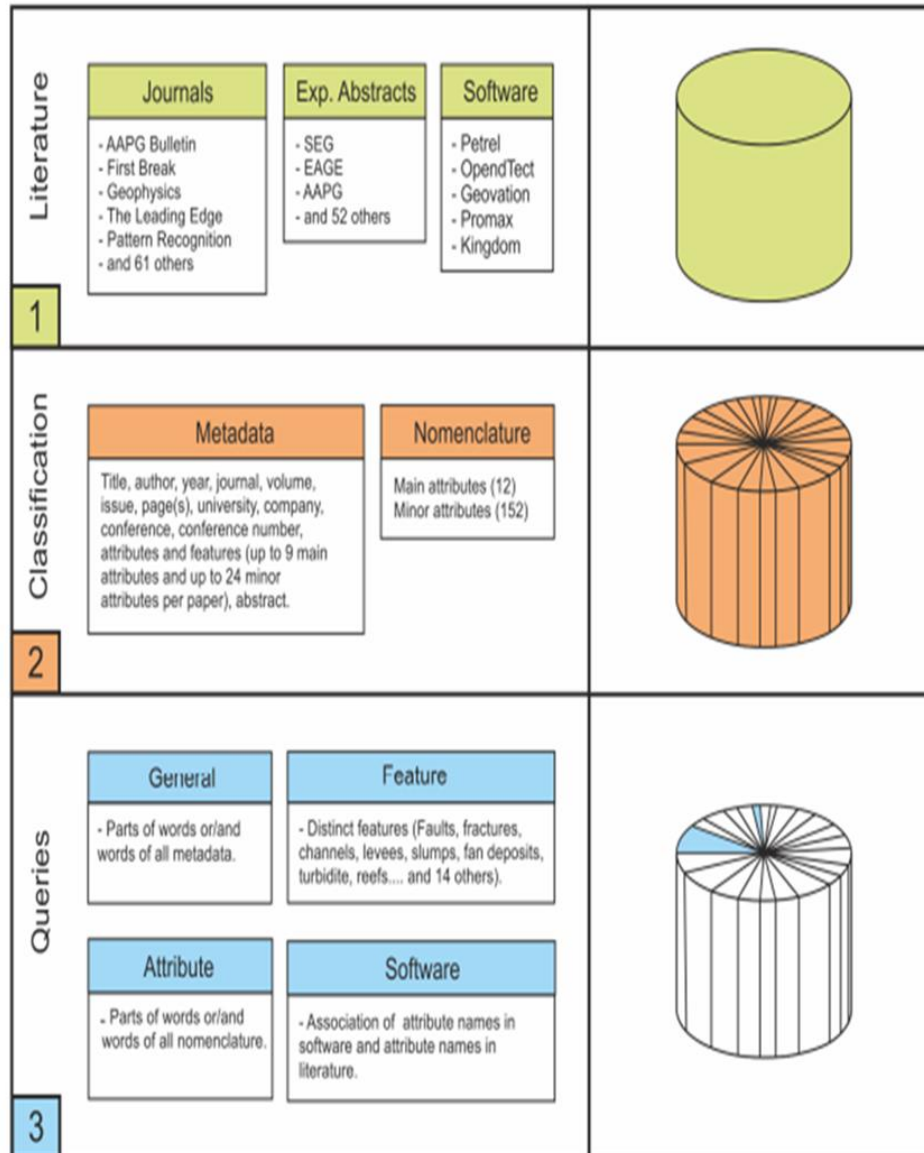


**Figure 1.** Amtmann et al. (2013) data base of attributes provided by multiple technology suppliers. In this work they do not attempt to define which attribute might be “best” for a specific objective.

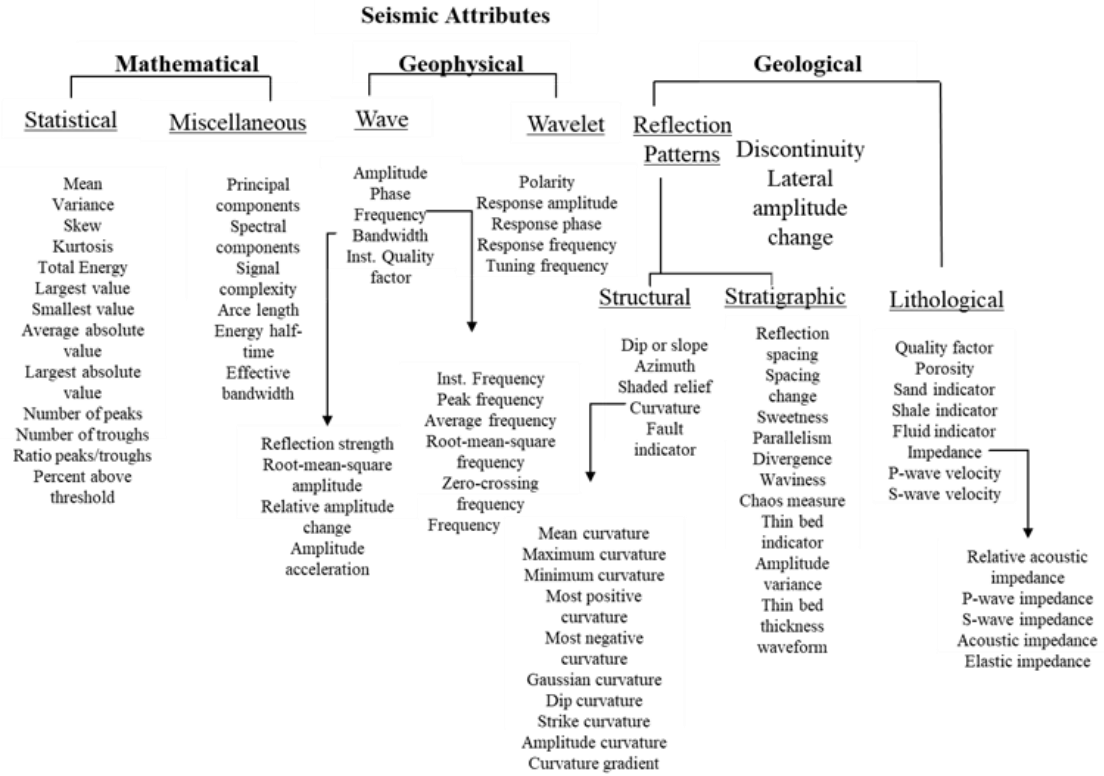


**Table 1.** Barnes’ (2016) taxonomy containing three main categories for seismic attribute application.



<p><b>Reflector configuration attributes</b></p> <ul style="list-style-type: none"> <li>• Time-structure</li> <li>• Dip azimuth and dip magnitude</li> <li>• Curvature</li> <li>• Aberrancy</li> <li>• Reflector convergence or parallelism</li> <li>• Reflector rotation</li> </ul> <p><b>Texture attributes</b></p> <ul style="list-style-type: none"> <li>• Amplitude gradient</li> <li>• Gray-level co-occurrence matrix textures</li> </ul> <p><b>Discontinuity attributes</b></p> <ul style="list-style-type: none"> <li>• Coherence</li> <li>• Amplitude curvature</li> <li>• Diffraction imaging</li> </ul> <p><b>Spectral attributes</b></p> <ul style="list-style-type: none"> <li>• Voice, magnitude and phase components</li> <li>• Peak frequency, peak magnitude, and bandwidth</li> <li>• Attenuation</li> </ul> <p><b>Impedance attributes</b></p> <ul style="list-style-type: none"> <li>• Acoustic impedance</li> <li>• Angle-limited stacks and elastic impedance</li> <li>• AVO slope and intercept</li> <li>• Elastic parameters:</li> <li>• Elastic impedance and extended elastic impedance</li> </ul> <p><b>Anisotropy attributes</b></p> <ul style="list-style-type: none"> <li>• Velocity variation with azimuth</li> <li>• Amplitude variation with azimuth</li> <li>• Impedance variation with azimuth</li> <li>• Frequency variation with azimuth</li> <li>• Discontinuity with azimuth</li> </ul> <p><b>Time-lapse attributes</b></p> <ul style="list-style-type: none"> <li>• Amplitude changes</li> <li>• Traveltime changes</li> <li>• Spectral changes</li> </ul>
---

**Table 2.** Marfurt’s (2018) taxonomy showing seven attribute families.

<b>Reflector Configuration Attributes</b>
<i>Reflector dip vector</i>
<i>Most-positive curvature value, <math>k_1</math></i>
<i>Most-negative curvature value, <math>k_2</math></i>
<i>Most-positive curvature vector, <math>k_1</math> and <math>\psi_1</math></i>
<i>Most-negative curvature vector, <math>k_2</math> and <math>\psi_2</math></i>
<i>Shape index and curvedness</i>
<i>Reflector convergence vector</i>
<i>Reflector nonparallelism</i>
<i>Reflector rotation</i>
<i>Reflector aberrancy (flexure) vector</i>
<i>Apparent dip</i>
<i>Apparent (Euler) curvature</i>
<i>Apparent aberrancy (flexure)</i>

**Table 3.** A table of reflector configuration attributes that I will use in my web-based application for each seismic facies. Attributes that effectively differentiate some facies of interest will appear in a green box, those that are less generally effective in a yellow box, and those are generally of limited use in a white box. For each facies, clicking the box will display vertical and time slices through one or more data examples.

## **Chapter 3. Integrating the Information Content of Multiple Attribute Volumes**

### **3.1 Multiattribute Review**

Russell (1997) defines multiattribute seismic analysis as a wide-ranging term that incorporates all methods that utilize more than one attribute to predict some physical property of the sub-surface. There are three common workflows to integrate the information content of multiple attribute volumes. The first workflow is to co-render three and sometimes four attribute volumes using HLS, RGB, or CMY color models coupled with alpha-blending (also called opacity or transparency) (e.g. Marfurt, 2015). The second workflow is to combine two and sometimes three attributes using crossplotting tools. The third is to extract the information content of three or more attributes using projection techniques including principal component analysis, self-organizing maps, and generative topologic maps, or machine learning algorithms such as multilayer feed forward neural networks and random forest decision trees. (Qi et al., 2017; Zhao et al., 2018; Kim, 2018; Lubo-Robles, 2018; Infante-Paez, 2018). The key to attribute-assisted facies identification is to find attributes that differentiate one facies from another. The numerical values resulting from seismic attribute computations can be used in machine learning to not only identify which facies is more likely at a given voxel, but also to quantitatively estimate the confidence that one has in a given prediction.

### *3.1.1 Interpreter Driven Workflows*

Seismic attributes are chosen by the interpreter's based on previous knowledge, publications or from experience. A common interpreter-driven multiattribute analysis workflow includes multiattribute display and cross plotting. Most modern interpretation workstations provide some form of multiattribute co-rendering using transparency, which is alternatively called opacity and alpha-blending (Marfurt, and Alves 2015; Marfurt, 2015; Marfurt, 2018; Henderson, 2008). Figure 2 shows a co-rendered image of dip-azimuth, dip-magnitude, and coherence volumes, which is utilized to identify the MTD. A second interpreter-driven workflow is cross plotting, where the interpreter defines polygons around "clusters" of points seen in a 2D histogram, Figure 3 shows a 2D histogram of reflector convergence magnitude and coherence for the data volume shown in Figure 2. The 2D histogram is then used to correlate the attributes with the seismic facies by drawing a yellow polygon around areas of low coherence and high reflector convergence magnitude, thereby highlighting zones of that behavior in the 3D volume (Figure 4) Unfortunately, current commercial software does not allow the definition of polygons for more than two attributes. While at least one software package allows the definition of a 3D hexahedron (simple limits along each attribute axis), cross plotting is underdeveloped as a tool for three attributes and not developed at all for more than three attributes.

Cross-correlation of multiple attributes has been of great interest as the relationship between attributes facilitates quantification of the seismic facies of interest. Attribute correlation to seismic facies helps the interpreter and the machine to quantify the facies with the applied attributes. Therefore, attribute selection is critical to

quantification of the seismic facies, as not all attributes are created equal when it comes to facies quantification. The identification of both useful and useless attributes further facilitates machine learning by editing the attributes for specific facies of interest (Barnes, 2007).

### *3.1.2 Algorithmically (or machine-driven) workflows*

Unlike multiattribute visualization and crossplotting, machine-driven workflows can easily analyze patterns lying in high dimensional spaces. There are three broad cases of machine-driven workflows: projection algorithms, unsupervised learning algorithms, and supervised learning algorithms. Projection algorithms define a plane or surface in some lower-dimensional space onto which the higher dimensional input data are projected. The most common projection algorithm is principal component analysis (e.g. Roden et al., 2015; Zhao et al., 2015) where the resulting projections are analyzed using either 2D crossplots or 3D red-green-blue (RGB) color-blending. A more recent variation on this is independent component analysis (e.g. Lubo, 2018) where the data are projected onto non-orthogonal basis functions that attempt to separate one type of “signal” from another using non-Gaussian statistics.

Unsupervised learning techniques include k-means (Coleou et al., 2013), Gaussian mixture models (Hardesty, 2017), self-organizing mapping or *SOM* (Coleou et al., 2013, Roden et al., 2015; Zhao et al., 2016, 2017)), generative topological mapping or *GTM* (Roy et al., 2015; Qi et al., 2016), and random forest decision trees (Kim, 2018). *SOM* and *GTM* project the high dimensional data onto a lower dimensional manifold. Both *SOM* and *GTM* both start with PCA as an additional projection, such that both are unsupervised learning projection methods.

Supervised learning techniques include probabilistic neural networks (Russel, 1997), multilevel feedforward neural networks (Russel, 1997) convolutional neural networks (Qi, 2018), and proximal support vector machines (Zhao et al., 2018). At least one commercial software package, OpendTect, provides a preselected suite of attributes that have proven to be appropriate to map gas chimneys, salt diapirs, or karst collapse and other features used in subsequent neural network analysis (Figure 5).

Zhao et al. (2018) utilized the multiattribute application to confirm the most useful attributes for karst features within a Fort Worth Basin seismic survey. Zhao et al. (2018) identified the best attributes by using attributes that users and algorithms utilize to define patterns within seismic data volumes. Zhao et al. (2018) augmented a qualitative attribute selection process with quantitative measures to differentiate features of interest. Zhao et al. (2018) then assigned weights to the attributes and the interpreters favored attributes as well as the attributes that the learning algorithm favor to create a SOM that best delineates the facies. These attributes highlight the features associated with karst facies, these include peak spectral magnitude, peak spectral frequency, most positive and most negative curvature, most positive and negative amplitude curvature, energy-ratio similarity (coherence) and GLCM (texture) homogeneity (Table 4). Zhao et al. (2018) then applied these attributes to create a self-organizing map

Qi (2016) applied multiattribute methods to create a seismic clustering algorithm to delineate seismic facies packages within the Gulf of Mexico 3D seismic dataset. The first step in this clustering technique is to identify the best attributes that identify the facies of interest. The facies of interest in this case include salt, mass transport

complexes and shale deposits. His workflow for identifying the best attributes that delineate these features included a large-scale attribute application process and applied Kuwahara filter to those attributes to gain a smoother image for complete segregation of the facies (Qi et al., 2016) (Figure 6). After computing the histogram of the correlation coefficients between the attributes applied to the seismic data, Qi et al. (2016) identified the best attributes that differentiate the selected facies. The attributes best suited for this method are coherence, reflector convergence, GLCM entropy, and GLCM dissimilarity (Figure 7). He then clustered these attributes to obtain a 3D view of the facies (Figure 8).

### **3.2 Multiattribute Application**

I investigate an example of structural deformation in a survey dominated by salt tectonics to better understand the concept of multiattribute analysis and which attributes to use to investigate the geologic features of interest, MTDs. The survey used to investigate MTDs was acquired in the late 1990s and imaged using prestack time migrated. Figure 9 shows vertical slices and a time slices at  $t=1.180$  (s) through the seismic amplitude volume. Figure 9 highlights an MTD within the seismic volume. The MTD shows highly chaotic amplitude responses.

Figures 10 and 11 show corresponding slices through coherence and the total energy (within a 5 trace by 20 ms analysis window) used in the energy ratio coherence algorithm. Note that the salt and the MTDs exhibits both low energy and low coherence. Figure 11 shows corresponding time slices through co-rendered most-positive and most-negative structural curvature. Although the curvature images clearly delineate faults and flexures of interest within the minibasin, the strongest anomalies occur internal to the

salt and the MTDs, where the low-amplitude chaotic events also exhibit chaotic dip. This rapid change in dip gives rise to high-amplitude curvature artifacts which was filtered out using a structure-oriented filter. Although these artifacts were filtered out, usually a human interpreter has no problem “ignoring” such artifacts; however, a simple threshold-based computer algorithm would give erroneous results to a voxel-by-voxel interpretation.

Consciously or subconsciously, a human interpreter is using a Venn diagram, such as that shown in Figure 12. The Venn diagram shows three attributes that when they overlap identify an MTD. This is the same process a human takes to determine the seismic facies of interest. A decision tree would implement the same construct algorithmically rather than visually.



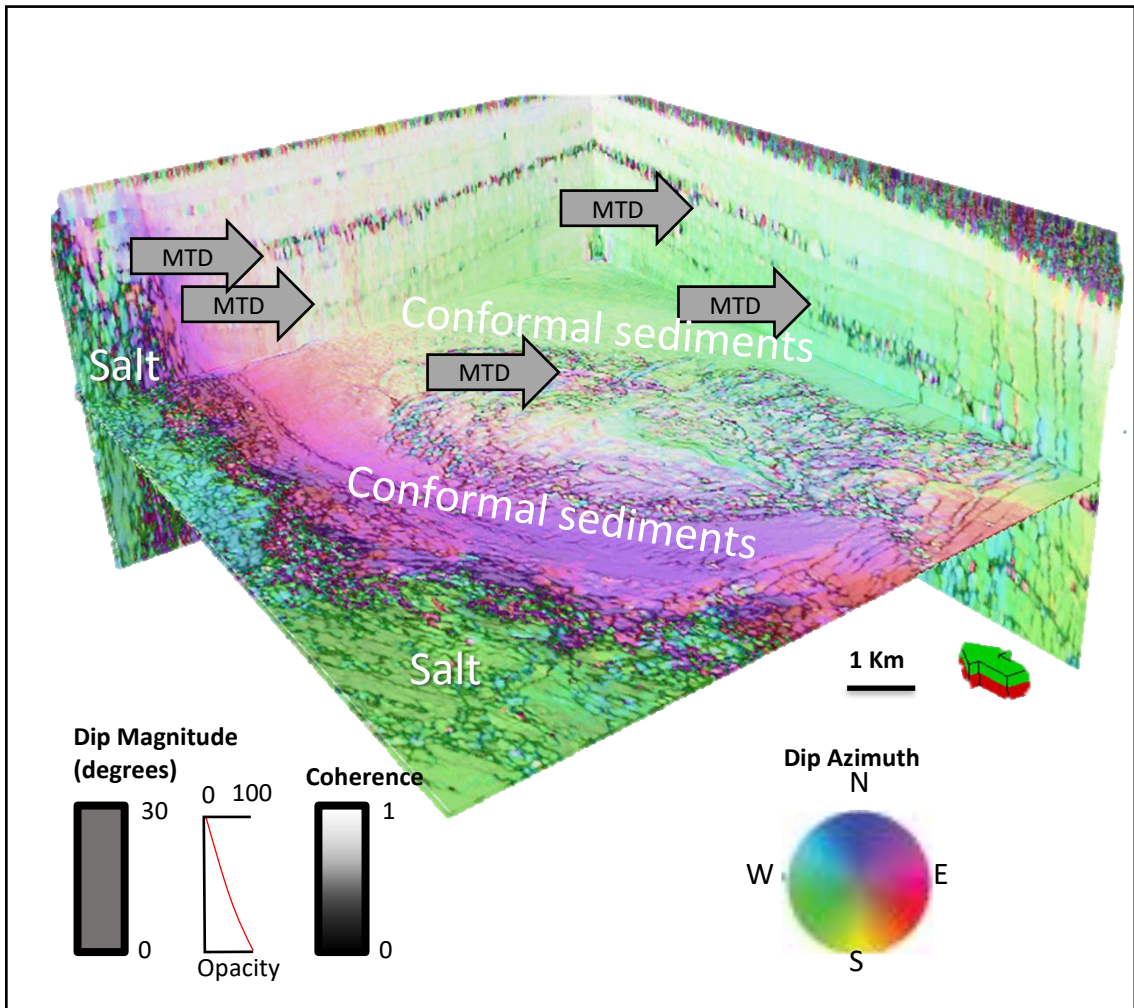


**Figure 2.** Vertical slices and a time slice at  $t= 1.80$  (s) through coherence, dip magnitude and dip azimuth volumes. Low coherence discontinuities appear black. A layer of conformal sediments dipping to the NE appears as magenta on the SW edge of the minibasin while those dipping to the SW appear as green on the NE side of the minibasin. The chaotic, rotated blocks within the MTD dip in all directions therefore the response is polychromatic, separated by low coherence.

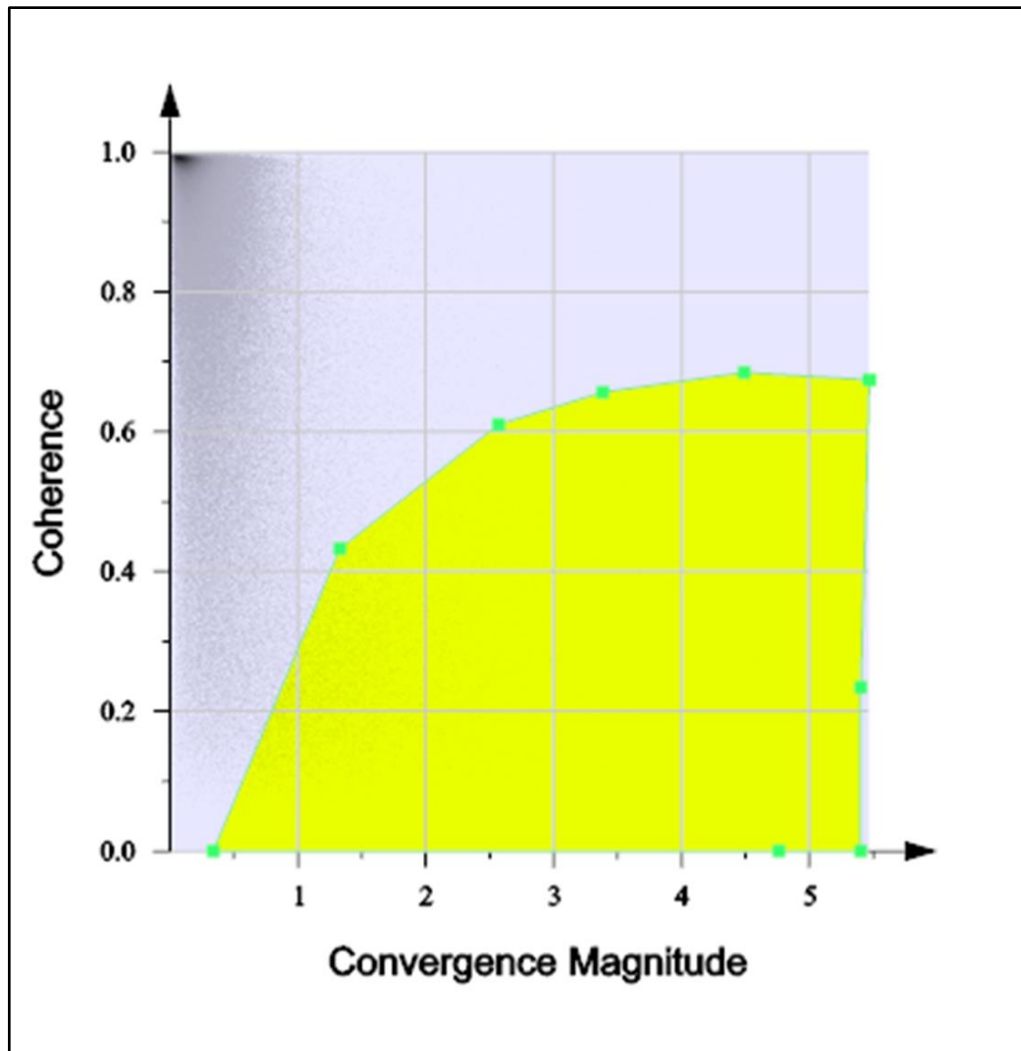


**Figure 3.** 2D Histogram of the seismic attribute coherence and convergence magnitude highlighting the relationship between the two attributes with MTDs. The defined convergence (non-parallel) incoherent yellow polygonal voxels exhibiting incoherent reflections, representative of MTDs and salt shown in the next figure.

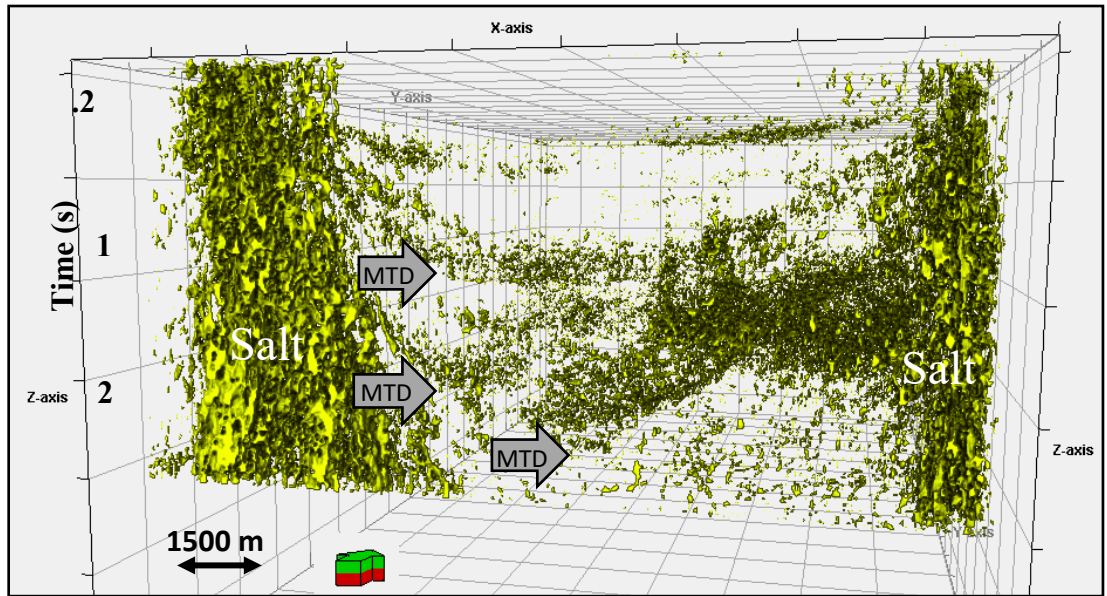


**Figure 4.** Such crossplots facilitate geobody extraction of MTDs and salt within the 3D seismic volume. Voxels (in yellow) defined by the polygon shown in the previous figure.



**Figure 5.** dGB’s OpenDtect’s subset of plugin applications that pre-selects the appropriate attributes to delineate specific seismic facies using a multilinear feed forward neural network. (dGB Earth Sciences, 2018).

**Table 1. Attributes used in this study and why we are using them.**

Attribute	Why using this attribute
Peak spectral magnitude	Due to nonspecular reflection, substantial amount of the reflected energy is not properly received by the receivers within the migration aperture.
Peak spectral frequency	Destructive interference at karsted and faulted regions exhibits lower spectral frequency.
Most positive principal curvature Most negative principal curvature	Many karst collapse caves are in bowl shape, which produce a strong positive anomaly along the perimeter and negative anomaly at the center.
Most positive amplitude curvature Most negative amplitude curvature	Karst collapse as well as diagenetically altered joints and faults generate lateral changes in amplitude.
Energy-ratio similarity (coherence)	Karsted and faulted regions are less coherent.
GLCM homogeneity	Karsted and faulted regions are less smooth.

**Table 4.** In the left column Zhao's et al. (2018) list of attributes useful in delineating karst features. The right column provides a geologic and/or a seismic imaging justification that a given attribute differentiates a karst feature from a background composed of laterally coherent, smoothly varying conformal reflectors

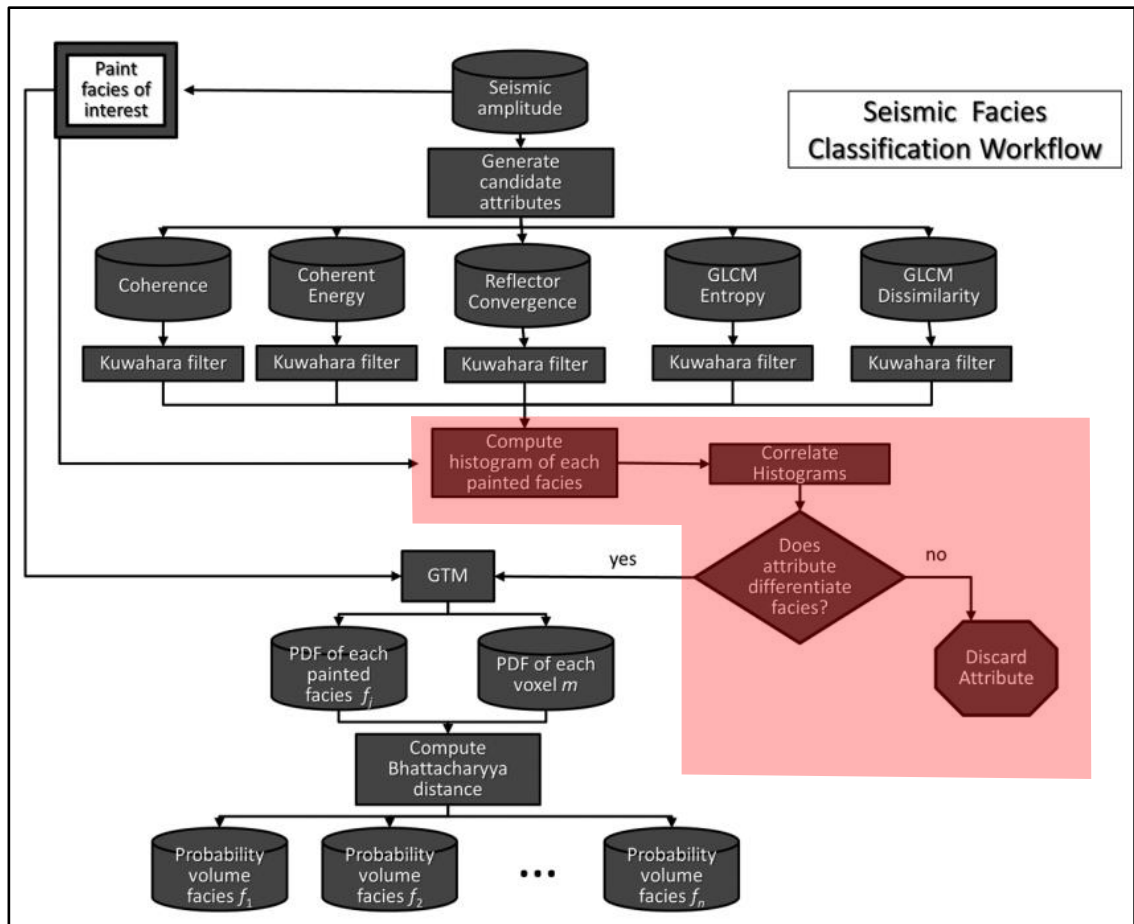


**Figure 6.** Qi et al.'s (2016) workflow to identify the most useful attributes to differentiate salt, shale, and mass transport deposits. Highlighted in red, they compute histograms of the attribute distribution for each of the selected facies as a measure of similar or dissimilar attribute response for each seismic facies discarding attributes that provide little discrimination.



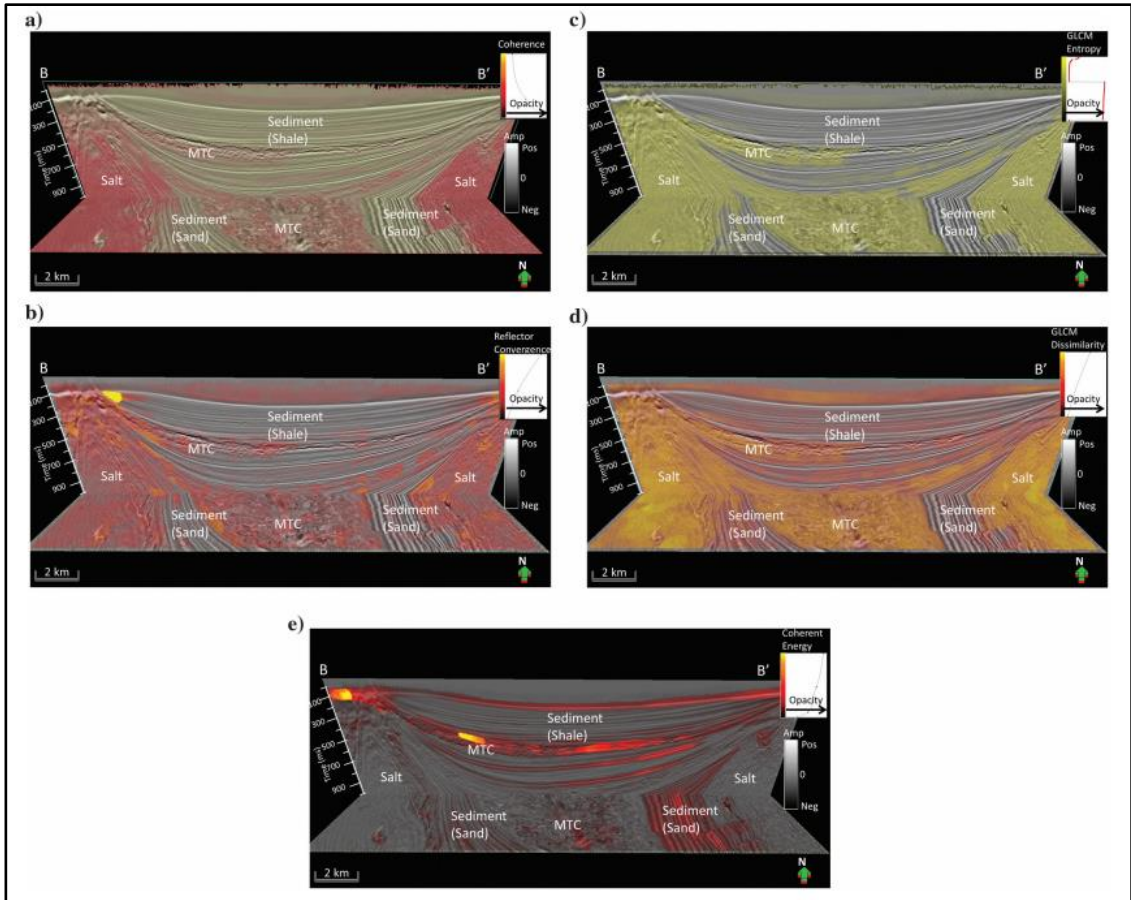


**Figure 7.** Qi et al.'s (2016) seismic facies expression of salt, mass transport deposits and conformal sediments. Shown on the vertical slices along line B-B' and time slices at  $t=1.172$  s through seismic amplitude co-rendered with Kuwahara filtered attributes, (a) coherence, (b) magnitude of reflector convergence, (c) GLCM entropy, (d) GLCM dissimilarity, and (e) coherent energy.

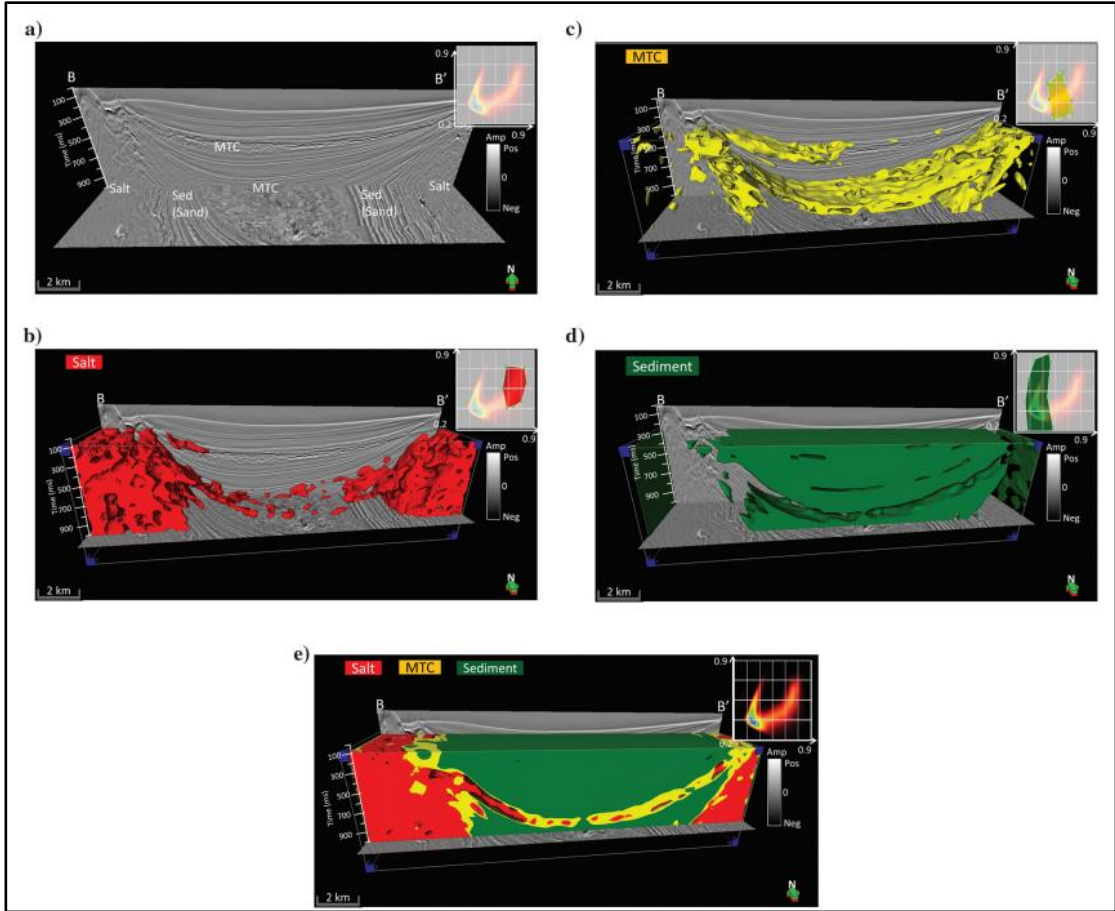


**Figure 8.** Qi et al.'s (2016) 3D geobody of salt, mass transport complexes and conformal sediments obtained by drawing polygons on the 2D GTM latent space. Vertical slices along line B-B' and time slices at  $t=1.172$  s through (a) seismic amplitude and amplitude co-rendered (b) with salt facies (in red), (c) MTD facies (in yellow), (d) sediment facies (in green), and (e) with all three facies.



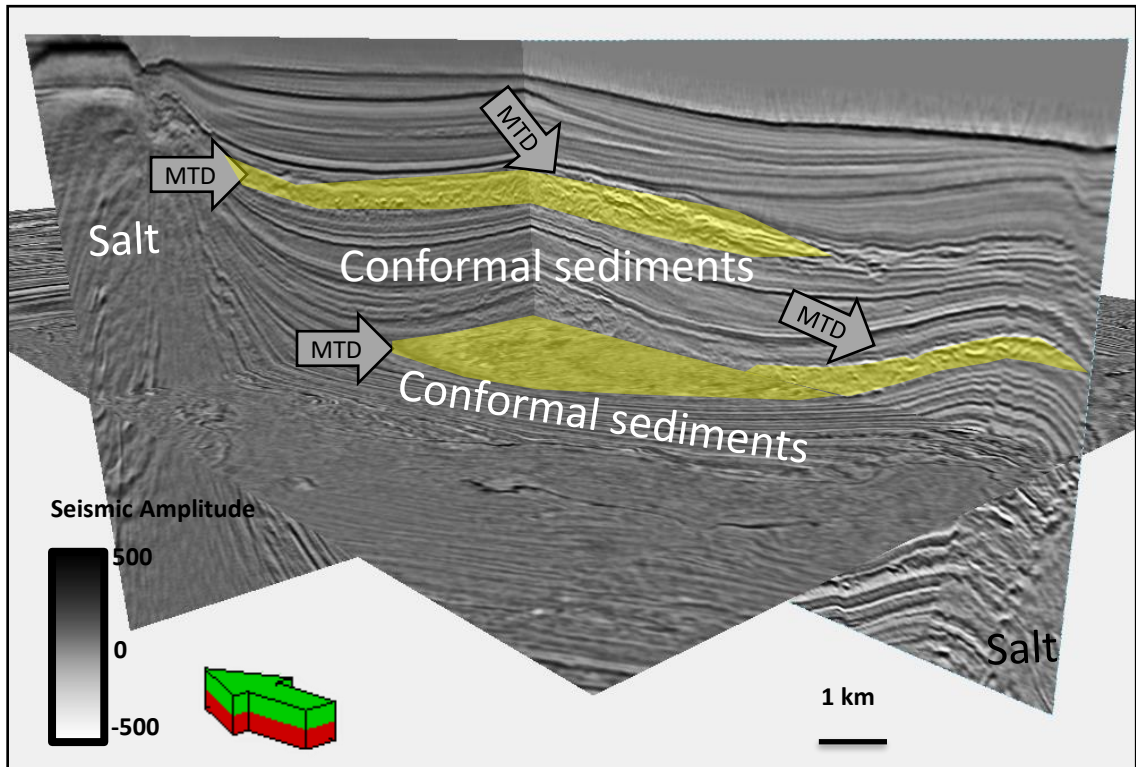


**Figure 9.** Vertical slices and a time slice at  $t= 1.80$  (s) through seismic amplitude volume with highlighted interpreted facies. Gray arrows and the yellow polygon areas identify MTDs within the seismic data volume. Surrounding the MTDs are conformal sediments, as well as salt diapirs creating the minibasins. Salt withdrawal formed minibasins resulting in sediment instability and mass transport deposits.

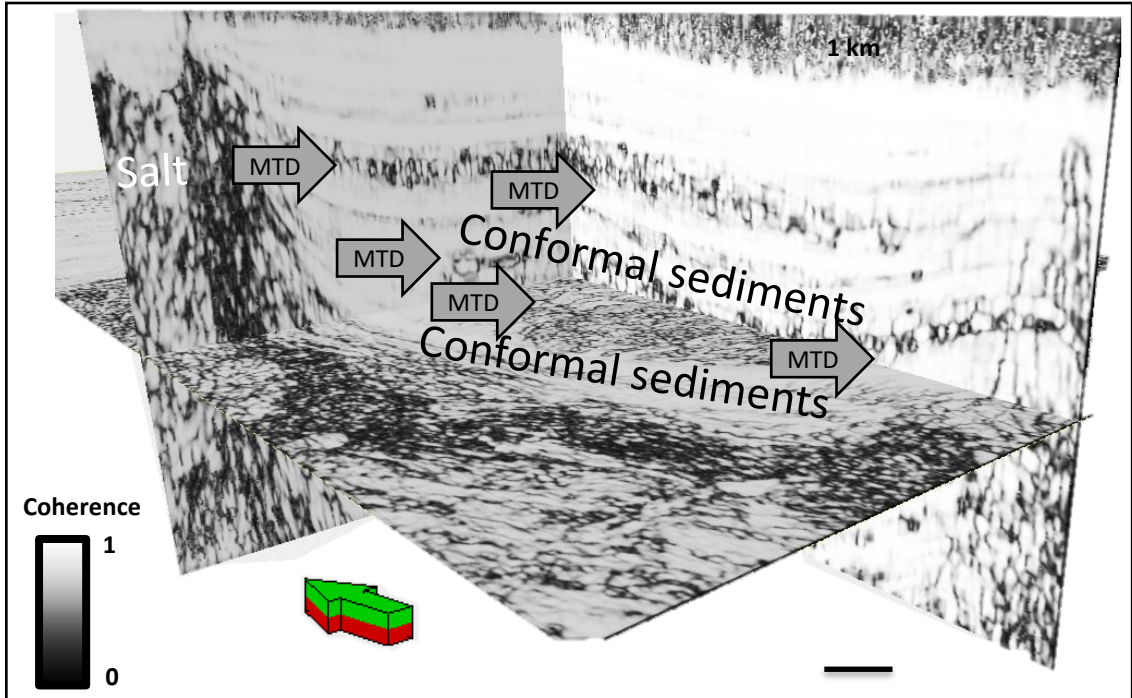


**Figure 10.** Vertical slices and a time slice at  $t= 1.80$  (s) through seismic coherence volume. This figure displays the same vertical slices as the previous figures. The gray arrows identify the MTD facies. The MTDs display low coherent values due to the large variation of sediment content and internal structures.

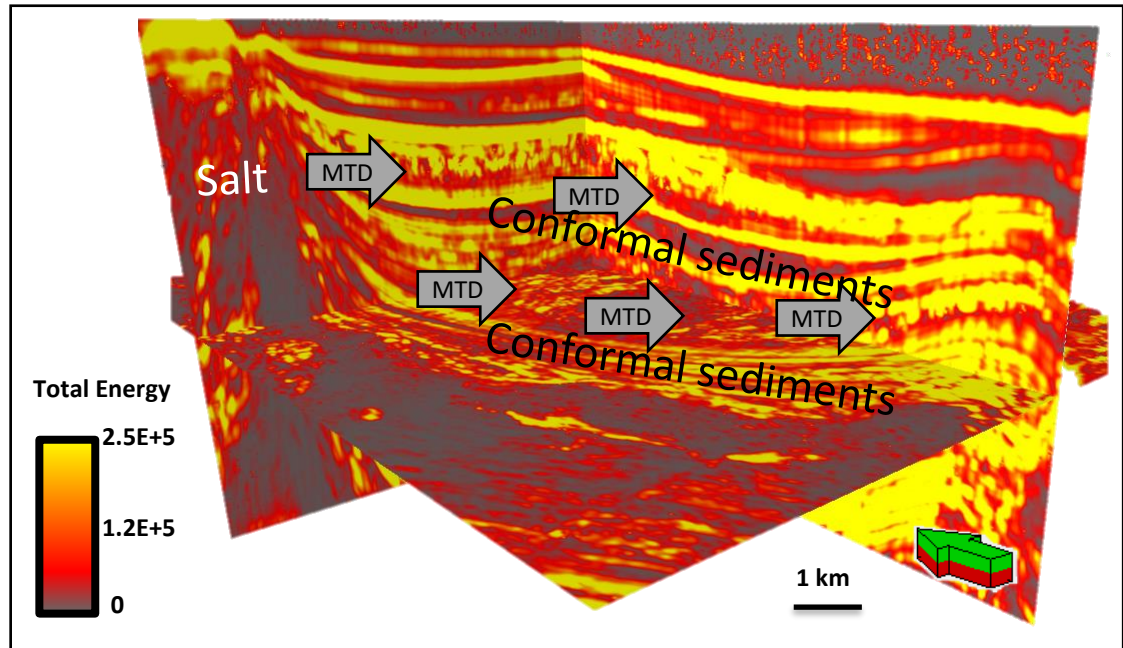


**Figure 11.** Vertical slices and a time slice at  $t= 1.80$  (s) through seismic total energy volume. The gray arrows identify the interpreted MTDs. The MTDs express high to low chaotic energy responses. This is due to the varying sediment content of the MTDs. The conformal sediments express laterally extensive and layered low to moderate energy responses.

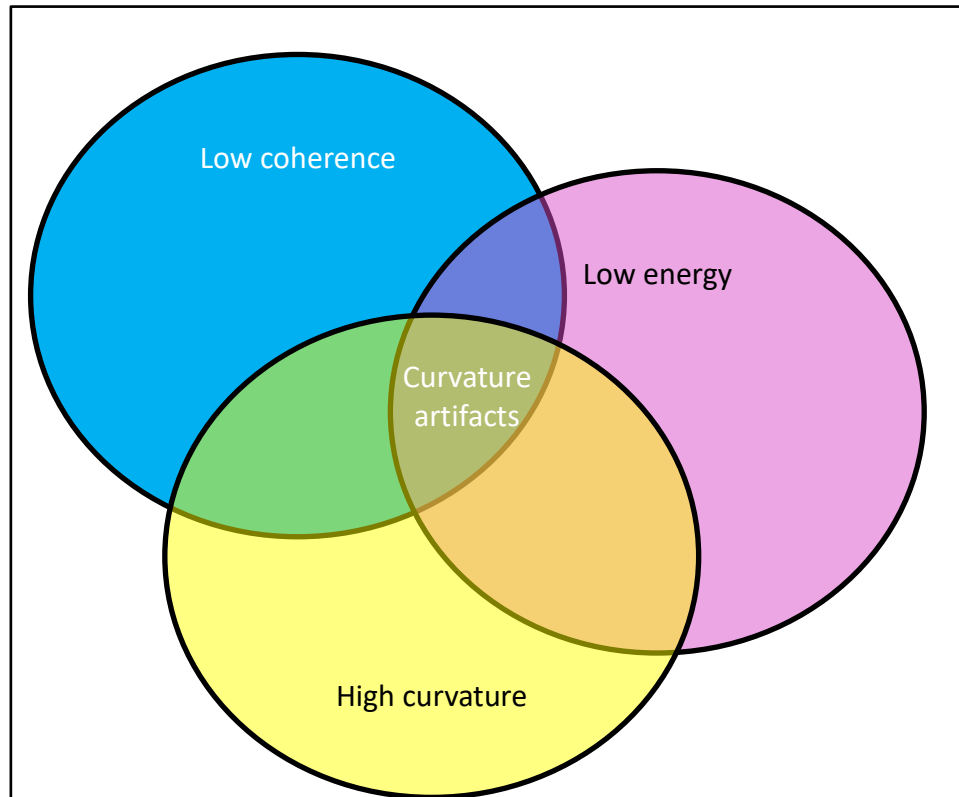


**Figure 12.** A conceptual Venn diagram showing the observation that curvature artifacts are more likely to occur in areas that exhibit low energy and low coherence. In a decision tree, such a combination would indicate that any curvature anomalies in such an area are noise, rather than signal and should not be used for structural or stratigraphic analysis.

## **Chapter 4: Seismic Expression of Karst and Mass Transport Deposits**

The initial goal of this thesis is to prototype a decision tree that represents a subset of commonly encountered geologic features. The longer-term goal is to build a web-based application to which other interpreters can add, attaining a more comprehensive seismic facies analysis tool at some future date which might be used by machine learning software. Using the pioneering work by West et al.'s (2002) analysis of channel systems, and Meldahl et al.'s (1999) analysis of gas chimneys as models, in this work it begins by documenting the attribute expression of just two seismic facies – karst collapse and mass transport deposits. Although these facies will vary greatly from basin to basin they are both amenable to a voxel-by-voxel analysis using seismic attributes. Infante-Paez (2018) calls the lateral, vertical, and scale consistency of such patterns *monogenetic*. The primary goal here is to capture their expression for at least one data volume, and thereby begin populating my website with images and recommendations. The application of seismic facies analysis will use Marfurt's (2018) attribute table (Table 2) to answer the questions that interpreters have for seismic facies analysis. The study of facies expression will further evolve into a decision tree of facies analysis and develop a database for users.

### **4.1 Karst Geologic Feature Summary**

Karst form by carbonate dissolution from the underlying soluble bedrock creating collapse features. There are two types of dissolution processes associated with karst processes, which are identified by the type of dissolution that occurs. The first type is hypogene where the dissolution of the bed rock occurs owing to non-meteoric solvent. The second type is owing to a meteoric based solvent (Cazarin et al., 2016;

Stafford et al. 2008). Common bedrocks associated with karsting are evaporites, dolomites, limestones, halite, and gypsum. The mineralogical makeup of the bedrock is one controlling factor of dissolution rates. For example, salt that has encountered the water table or is extruding at the surface due to diapirism allows the rate of karstification to occur more rapidly than a limestone under the same environmental conditions. The chemical diagenesis of carbonates occurs with dissolution, remobilization, and precipitation of calcium carbonate producing the karst features (Milad, 2017; Milad and Slatt, 2017). This in turn affects the overlying deposition which karst create diverse structures like sinkholes, underground river system, caverns, which in turn can be difficult to identify using seismic alone (Zhao et al., 2018). The identification of karst features can be difficult to determine in seismic because they may be under the tuning zone or resolution zone and they can be misinterpreted as other facies.

These collapse features can take a variety of forms including sinkholes, fractures, and subsurface caverns (Figure 13). Loucks (2008) defined karst as “the diagenetic features and drainage systems produced during chemical dissolution and associated modification of soluble rocks.” Karst structures can form where rain water or groundwater has dissolved the underlying carbonate or evaporite rock thereby d of the area such that basinal fluids such as H<sub>2</sub>S can rise and encounter oxidized groundwater (Natural Resource Report, (2007/003). The resulting sulfuric acid can then dissolve the carbonate rock like the Carlsbad Caverns in New Mexico (Natural Resource Report, (2007/003). These features are common within carbonate groups like the Hunton Limestone of Oklahoma where they enhance the permeability of fractures within

locations of interest (Milad and Slatt, 2018; Milad, 2017). Figure 14 shows sink hole features from karstification of the Hunton Group by the stratigraphic cross section of well logs where the thickness of the Hunton Group changes laterally, resulting in an increased thickness of the overlying Woodford Shale (Milad and Slatt, 2017). In this case, it is pertinent to know karst locations for Woodford sweet spots.

#### *4.1.1 Seismic Amplitude Expression of Karst Features*

Karst features will be encased by planes of curved and non-parallel reflectors with offset dependent on the extent of the collapse depth of the karst. In many cases multiple karst features developed in an area with similar seismic amplitude expression to one another (Figure 15 and 16). They exhibit continuous to semi-continuous reflector continuity within the collapse feature depending on the severity of the karst collapse. The collapse depth depends on the amount of dissolution, and collapse depth of the underlying bedrock. The karst feature can contain a variety of sedimentary rocks including the host carbonates or evaporites. The collapse is due to the overburden and the instability of the carbonate sediments owing to dissolution. The amplitude of the karst feature will be moderate to high impedance contrast as the sediment contents within the collapse feature varies from carbonates and evaporites to sand and mud (Figure 15). In the time or depth domain the karst feature will look like a pocket, in that it will be circular, or it will have polygonal shape with joint connectivity (Qi et al. 2018) (Figure 15). Seismic images may show sink features, polygonal faulting, and structural lows that delineate the joints, caves and collapse features of karstification (Qi et al. 2018). In vertical slices these features become evident in their amplitude expression (Figure 16). The cross-section of these features is shown in Figures 16. Karst form sinks

or collapse features that can be identified by the discontinuities of reflectors on vertical slices as seen in Figure 16.

#### *4.1.2 Seismic Attribute Expression of Karst Features*

The nature of a karst feature is more structural than stratigraphic, therefore the best type of seismic attribute to apply to a seismic data set with these features would be geometric attributes and spectral attributes which delineate the discontinuities and the spectral magnitudes identifying the lithological changes and the geometric changes in the deposits. The karst features can be differentiated from the surrounding less altered dolomite by multiple attributes that measure reflector configuration, discontinuity, texture and spectra (Figure 17-22). Sullivan et al. (2006) used curvature, coherence, and energy ratio similarity to map karst. Zhao et al. (2018) used peak spectral magnitude, peak frequency, most negative and positive curvature, coherence and GLCM textures (Qi et al. 2018; Zhao et al. 2018).

Karst features are identified as structured features with the collapse features encased by polygonal faults and outer edge collapse features and can therefore be firstly interpreted with the geometric attributes. These include the coherence where the coherence response is low due to the collapse feature (Figure 17) (Torres-Parada et al., 2017). Dip azimuth and dip magnitude are used in this facies example to express the dipping direction of the collapse features. The response from the dip magnitude and the dip azimuth (Figure 19) shows polychromatic responses from the internal structures of the karst. The dip azimuth response is due to the bowl shape of the karst features creating a multi-directional response within the karst. The most positive and negative curvature delineates change in the dip which expresses the karst features as they have



dip change within the collapse feature and the external edges of the collapsed feature (Figure 18). The most positive curvature response ( $k_1$ ) is exhibited on the outer rim of the karst facies and the internal structure is expressed by the most negative curvature ( $k_2$ ).

The lateral changes in layer thickness and impedance produce lateral variation in spectral components (Figure 20) (Qi et al. 2014; Torres-Parada et al., 2017). The chaotic collapse features and rugose surfaces give rise to non-specular scattering, which in turn gives rise to constructive interference at low frequencies and destructive interference and at high frequencies, resulting in lower bandwidth and lower peak frequency (Qi et al. 2014). Figure 20 is the spectral magnitude response co-rendered with coherence to highlight the spectral magnitude response of the karst feature expression. The spectral magnitude expression of the karst features are low values and highlight the expanse of the feature.

Karst features yield textural effects within the seismic data due to the chaotic amplitude response of the karst facies. The attributes that best delineate these features are GLCM dissimilarity and contrast (Figures 21-22). GLCM texture attributes are a suite of statistical measures that attempt to quantify lateral patterns in reflectivity along structural dip. These calculations are relatively insensitive to the amplitude magnitude. The attribute delineates the contrast of the karst to the sediments surrounding the feature (Figures 21-22) (Marfurt, 2018).

## **4.2 Mass Transport Deposits**

Mass transport deposits are defined as mass flow deposits that have occurred owing to slope failure, allowing sediment to move down the slope face and to be

deposited down dip. Mass transport deposits are sedimentary deposits that have exceeded the slope stability angle causing slope failures and gravity flow processes which can lead to amalgamation surfaces at the base, slump scars, large geomorphological structures and convoluted bedding (Slatt, 2006).

Mass transport deposit (MTD) is a simplistic term representing many depositional environments ranging from submarine fan clastics to sands and muds in the Gulf of Mexico (Oyedele, 2005) to the mixed lithologies containing Bone Springs in the Delaware Basin, slope carbonate aprons in the Midland Basin of Texas and New Mexico, chalk in the Danish section of the North Sea, and sand wedges in the South China Sea (Gong et al., 2014). Mass transport deposits travel basinward and can vary in size and shape based on the slope failure type and the sediment composition.

Moscardelli and Wood (2008) characterized the morphology of these deposits as a function of location and mechanics of failure (Table 7). (Moscardelli and Wood, 2008; Bull et al., 2009). There are many factors that control mass transport deposits including slope failure location, slope failure type, kinematic movement of the failure and the mass flow of the failure. The variable types of failure make delineating the MTD important for further determination of composition, internal and external structures that could be associated with the feature as well as the identification of depositional environments.

Depending on the lithology and location, MTDs can be reservoirs, seals, or drilling hazards (Bull et al., 2007; Gong et al., 2014). Slatt (2007) defines MTDs as “massive slope failures allowing sediment to flow down slope causing large-scale erosion on the underlying sediments”. The forms of these features and the lithology of

the MTD are dependent on the location of the slope failure within the basin and can range from inner shelf slopes to basinward valleys. MTDs often interact with previous mass transport deposits, giving a rise to the term mass transport complex (MTC).

Moscardelli and Wood (2008) divide MTDs into two classes determined by their slope failure mechanisms as well as their source area. The first class of MTD is by continued debris attachment to the slope failure. The slope failure attachment or detachment indicates the casual mechanisms as well as the source location (Table 6). The casual mechanism of the MTD can give information of the depositional environment at the time of failure and can help to identify the matrix of the MTD. The mechanisms of the MTD can also be a significant indicator to the erosional surface on the underlying sediment layer on which the MTD travels (Moscardelli and Wood, 2008). These MTDs contain chaotic, low-amplitude reflections with variable reflector continuity and contained irregularly shaped internal geometry caused by the internally rotated blocks (Gong et al., 2017). The same amplitude expression occurs within the MTDs in the Gulf of Mexico where minibasins are formed due to salt diapirism (Figure 22)

#### *4.2.1 Seismic Amplitude Expression of Mass Transport Complexes*

Mass transport deposits vary in seismic amplitude characteristics by their mechanism of transport, the stratigraphic structures and the seismic response in amplitude. The interpretation of these features is dependent on the resolution of the data and the size of the MTD. If the feature falls below the tuning limit then the features are not reliably interpreted; however, often the features are large enough to distinguish some of the common internal features (Gong et al., 2014; Moscardelli and Wood 2007).

The mechanism, sedimentary structures and the seismic expression delineate the type of MTD within the location of interest. MTDs are subdivided into the three types of transports, debris flow, slump, slide deposit, by their transport mechanisms, sedimentary structures and seismic expression. The mechanisms within the MTD is dependent on the rotation of the internal sediments or the internal deformation (Moscardelli, and Wood, 2007). The sedimentary structures are defined by the internal structures and the matrix of the MTD. The seismic features are the structures associated with the MTDs massive movement as well as the internal expression of the MTD.

In the northern Gulf of Mexico, the sediments transported consist primarily of sand and mud (Sarkar and Marfurt, 2017). Slope failures are initiated by both sea level fluctuation and salt diapirism. Due to these external factors that have caused slope structure instabilities within the Gulf of Mexico there are many MTDs (forming multiple MTCs) in our 3D seismic survey. Gong et al. (2014) described four types of MTDs utilizing the methods from Moscardelli and Wood (2008), Bull et al. (2009), and Olafiranye et al. (2002) within a large seismic data within the northern South China sea margin.

The seismic amplitude expression of mass transport deposits is often chaotic in nature on both vertical and time slices (gray arrows in Figure 22). In this image there are multiple MTDs stacked with conformal layered sediments separating them. The MTDs exhibit variable amplitudes within the structure and near the slope scarp location. Towards the toe of the MTD the amplitudes become less chaotic as the transport thins and the kinematic energy of the MTD flow dissipates (Figure 22).

Examining the surrounding context, the seismic expression about the MTD is in general more continuous, with less lateral variation than the internal MTD structure (Figure 22). The bottom of the MTD erodes the sediments below, truncating preexisting layered sediments, channels, faults, and other MTDs (Figure 23).

#### *4.2.2 Seismic Attribute Expression of Mass Transport Complexes*

Given this preliminary interpretation of the mass transport deposit, I evaluated a suite of twelve candidate geometric and spectral attributes with the goal of differentiating the MTDs from the surrounding facies. Based on previous experience by Qi et al. (2016) I generated the suite of attributes shown in Figures 22-31, where the relative value of each attribute is displayed in each caption. Note that while a given attribute, such as the vector dip, may be of significant value to a human (in context) interpreter examining the neighboring facies, it has only limited value if the goal is to construct a voxel-by-voxel classification using machine learning.

The list of attributes is not exhaustive; other GLCM texture attributes as well as the spectral bandwidth and peak frequencies can be used to differentiate the MTD from the surrounding facies. The inclusion of such an exhaustive analysis is well suited for a web application.

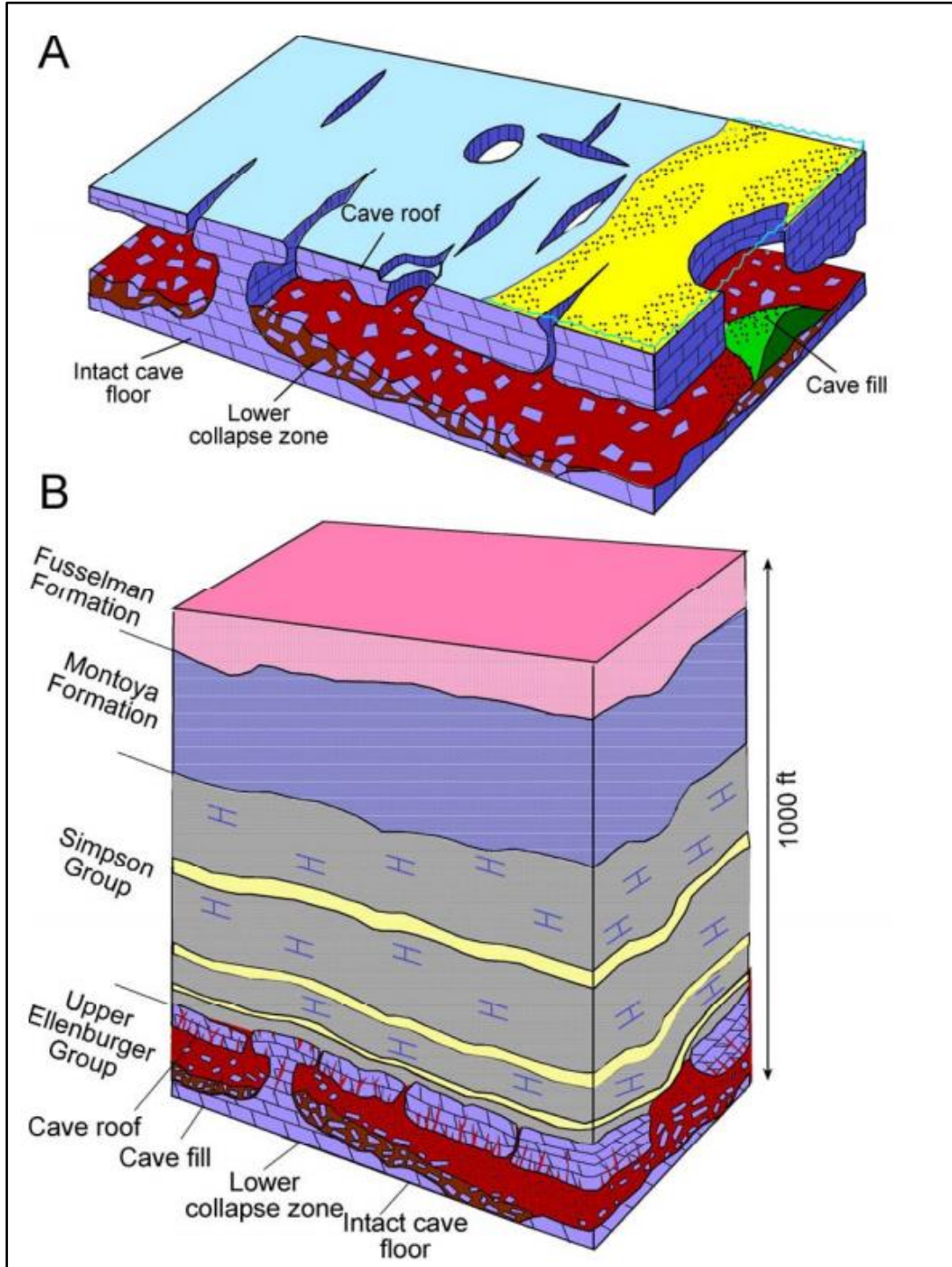


**Figure 13.** Loucks' (2008) cartoon of karst features within the Ellenburger formation in Texas. This shows the type of faults that occur with karst as well as the type of fill, cave formation and sink holes.

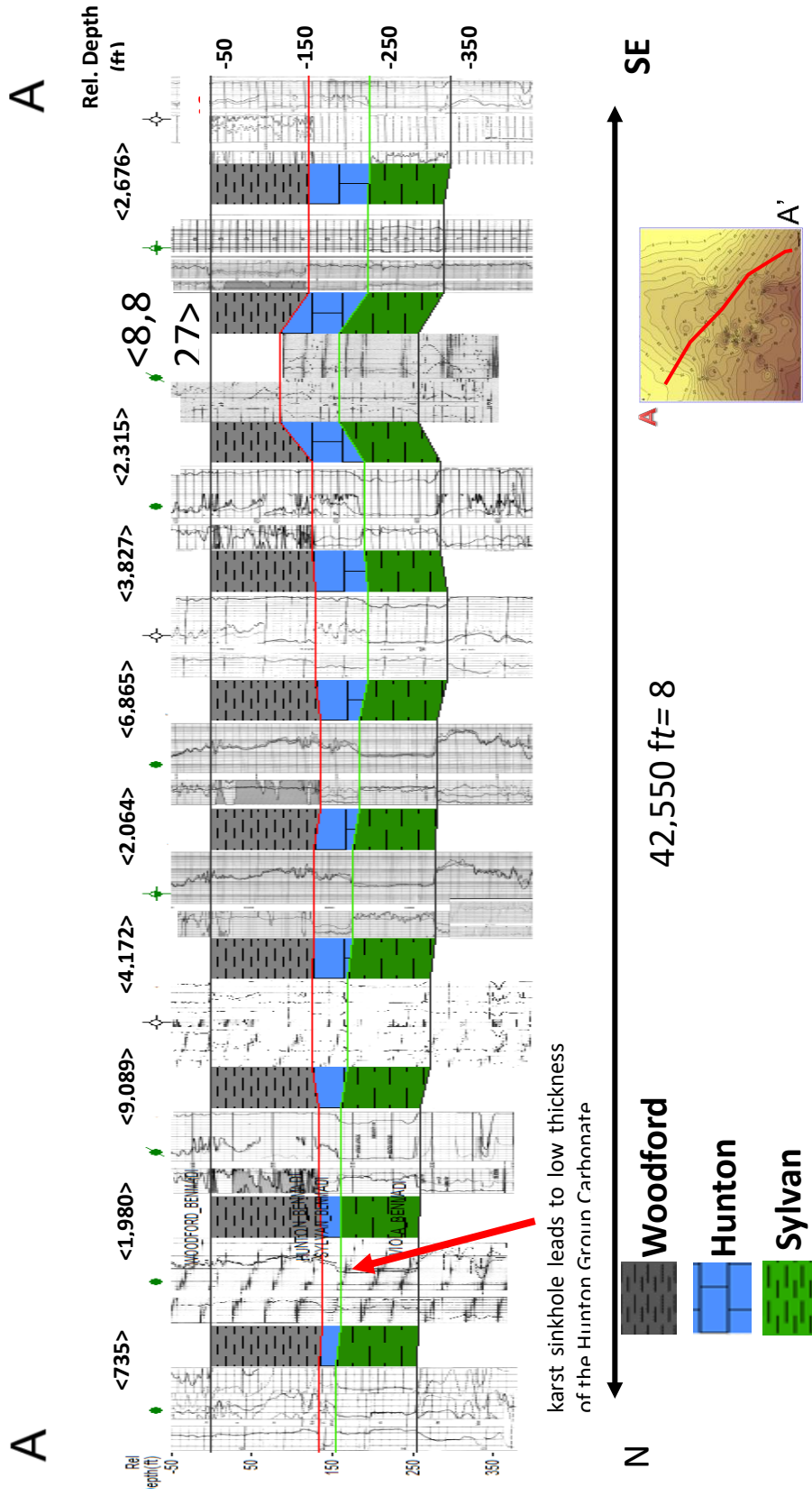


**Figure 14.** Cross section of well logs with stratigraphic interpretation of the Woodford, Hunton and the Sylvan groups. The red arrow shows the karst feature as seen in the gamma ray log and in stratigraphic interpretation where there is a paleogeographic low allowing more accommodation space for the Woodford Shale to be deposited (Milad and Slatt, 2017).

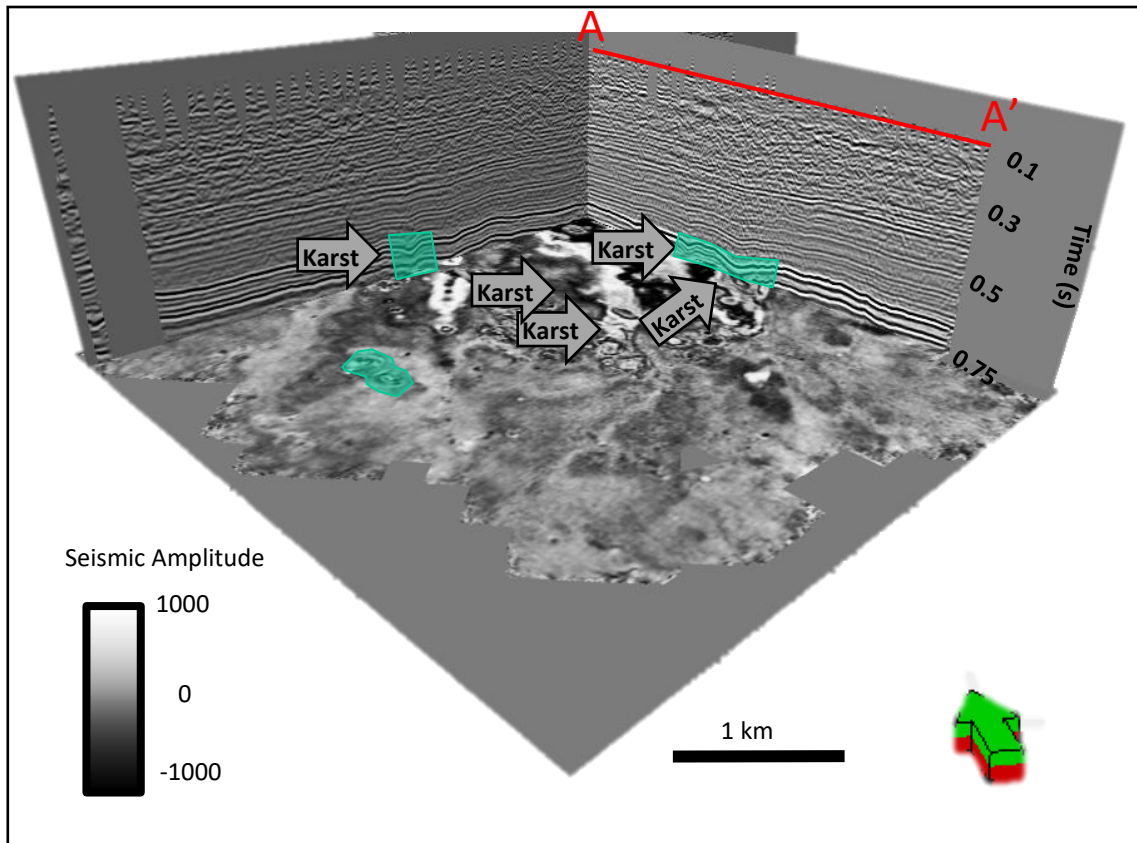


**Figure 15.** Vertical slices and time slice at  $t=0.75s$  through the seismic volume. The teal polygons highlight the karst facies within the Ellenburger Formation. These facies display circular collapse features as well as faulting near the collapse clusters (Data courtesy of Marathon Oil Co.).



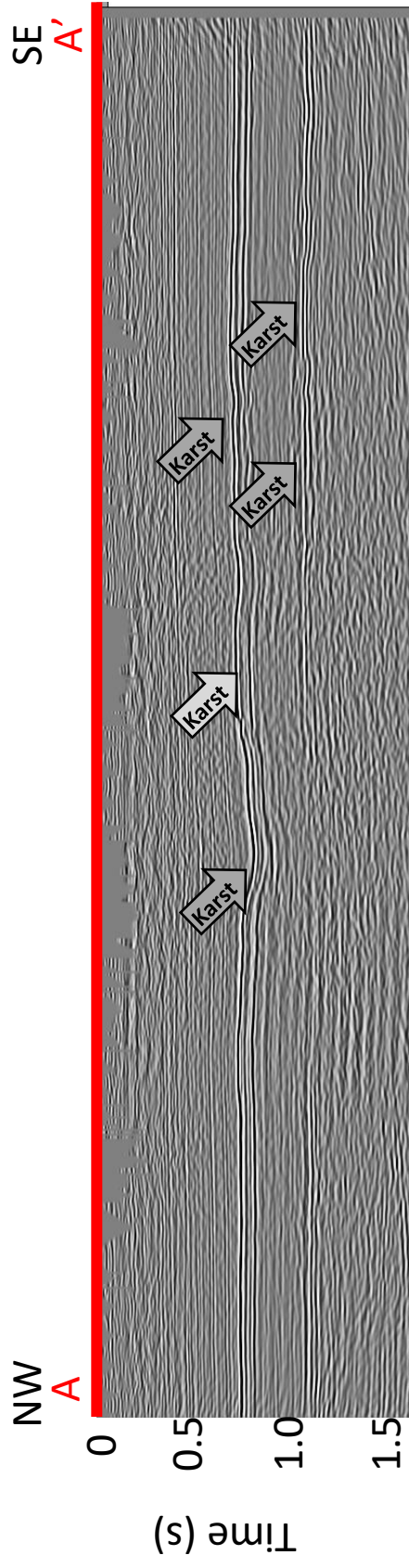


**Figure 16.** Vertical slice A-A' through the seismic amplitude volume where the karst features from the previous figure are indicated by the gray arrows. The seismic amplitude cross section displays the karst show curved reflector expression and polygonal faulting. The light gray arrow indicates a karst defined by polygonal faulting. The darker gray arrows indicate karst with a more curved reflector expression.

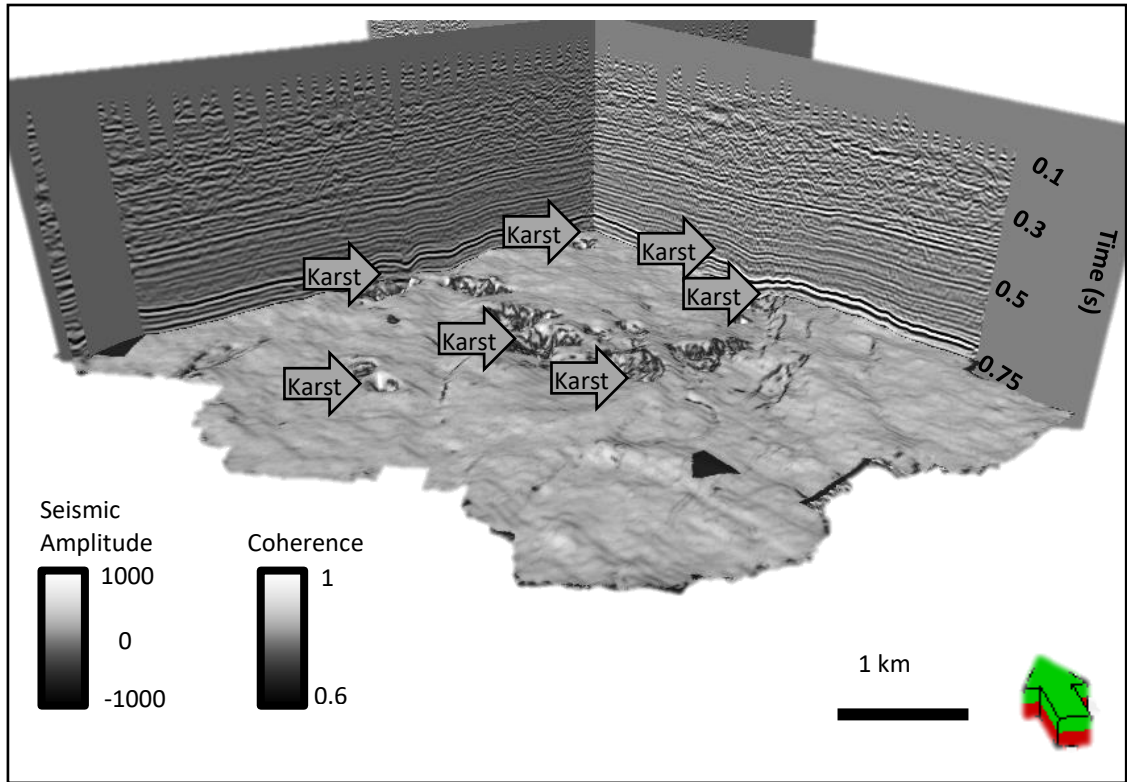


**Figure 17.** Vertical slices through seismic amplitude volume and a phantom horizon 25 ms below the top of the Ellenburger formation through the seismic coherence volume. The karst features exhibit a low coherence response.

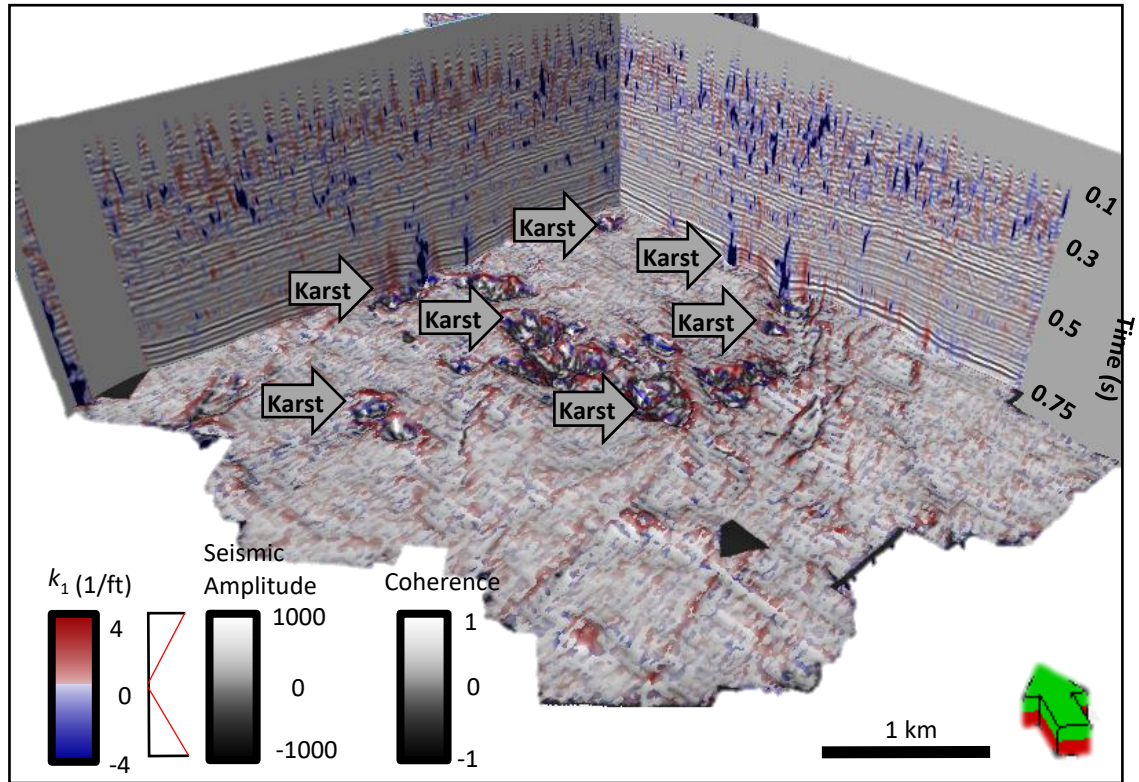


**Figure 18.** Vertical seismic amplitude slices and a phantom horizon 25 ms below the top of the Ellenburger formation through the corendered seismic coherence and curvature volumes. Gray arrows indicate karst features. The vertical slices express the amplitude co-rendered with the most-positive and most-negative curvature to delineate the karst collapse features. The bowl-shaped karst features exhibit a strong negative curvature internal response (in blue) a low-coherence internal response (in black) and a positive external response (in red).

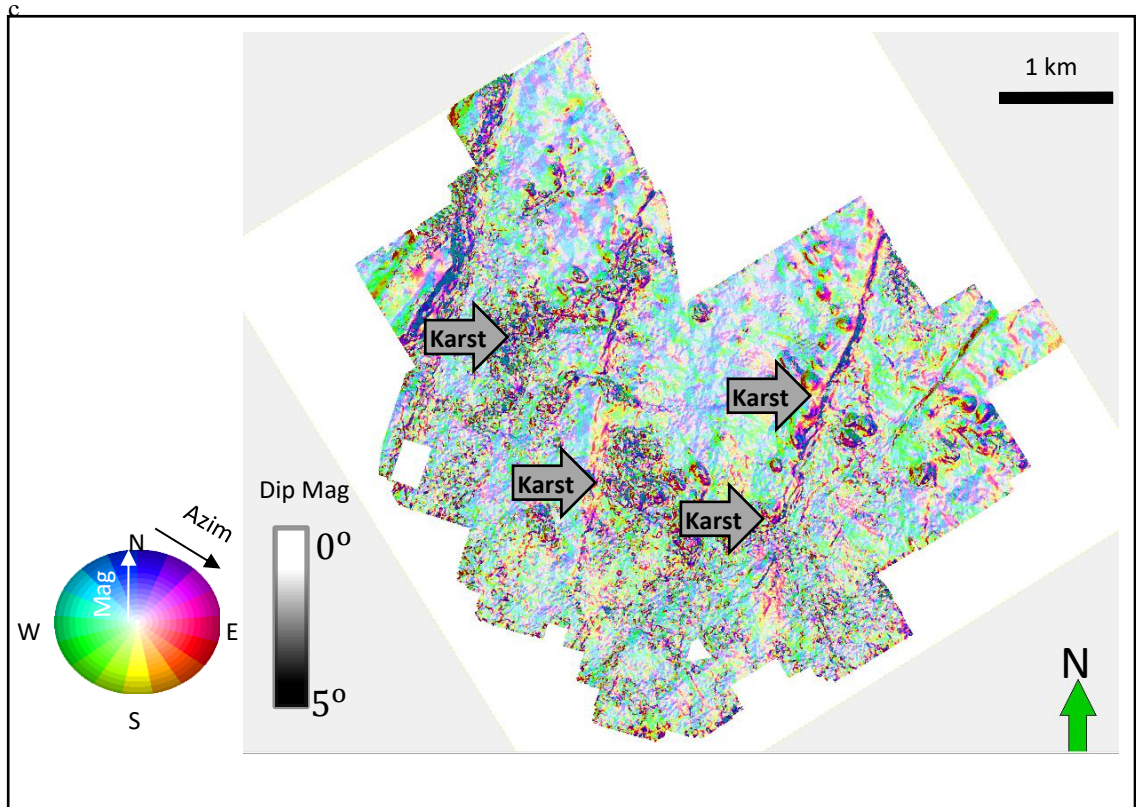


**Figure 19.** Horizon slice along the top Ellenburger formation through co-rendered dip azimuth and dip magnitude volumes. The karst features display high dip magnitude values as well as variable dip azimuth. Curvilinear faults strike toward the northeast.



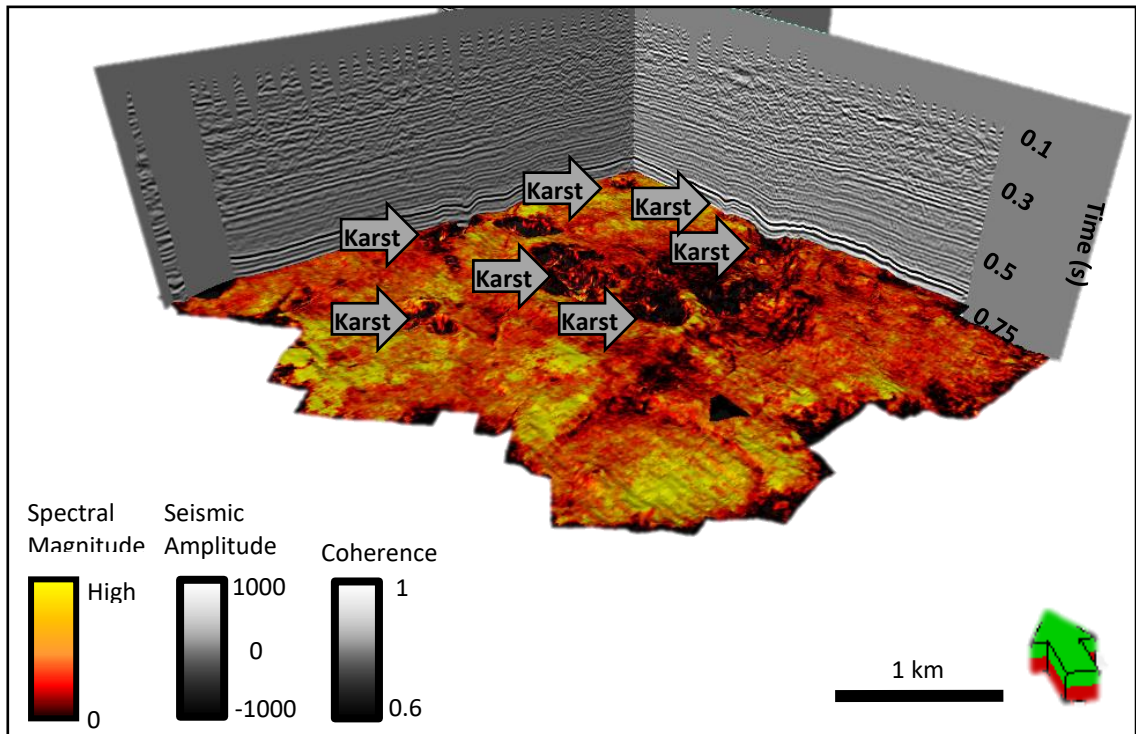


**Figure 20.** Vertical seismic amplitude slices and a phantom horizon 25 ms below the top of the Ellenburger formation through corendered seismic coherence and spectral magnitude volumes. Karst features display low spectral magnitude within the collapse feature.

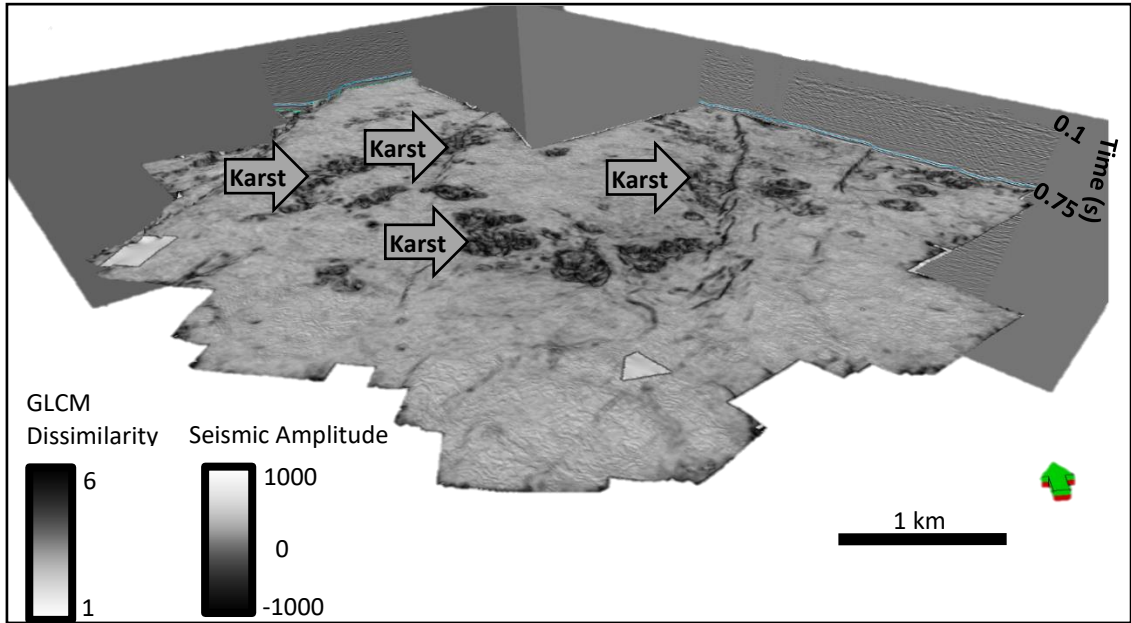


**Figure 21.** Vertical seismic amplitude slices and a phantom horizon slice 25 ms below the top of the Ellenburger formation through the corendered seismic amplitude and GLCM dissimilarity volumes. Karst features display high dissimilarity values.

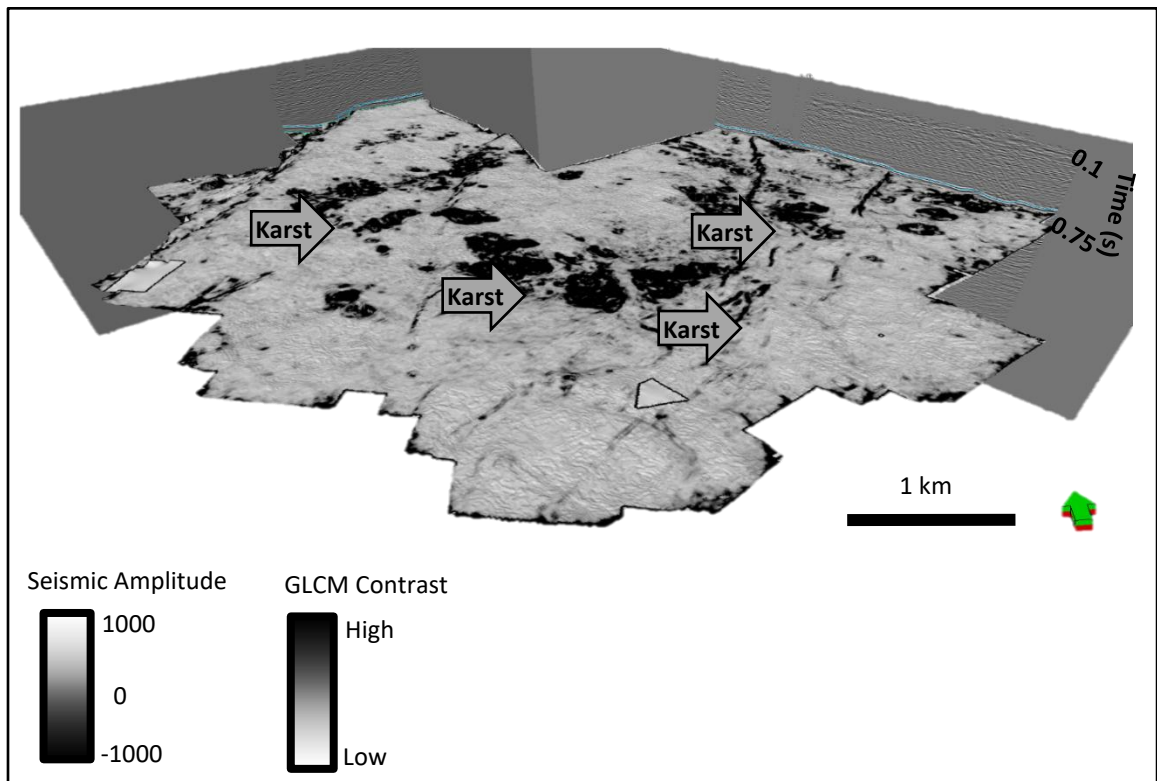


**Figure 22.** Vertical seismic amplitude slices and a phantom horizon slice 25 ms below the top of the Ellenburger formation through the corendered seismic amplitude and GLCM contrast volumes. Karst features exhibit high contrast values.

Reflector Response	Corresponding attribute
<p><b>Internal Reflector Configuration</b></p> <ul style="list-style-type: none"> <li>• Piecewise continuous to chaotic</li> <li>• Bowl-shaped</li> <li>• Non-parallel, thickening</li> <li>• Narrow band, lower frequency</li> </ul>	<p><b>Attributes for voxel by voxel quantification</b></p> <ul style="list-style-type: none"> <li>• Coherence, GLCM entropy, GLCM homogeneity</li> <li>• Structural curvature, Bowl shape index</li> <li>• Reflector convergence, Parallelism</li> <li>• Peak magnitude, peak frequency, Bandwidth</li> </ul>
<p><b>External Reflector Configuration</b></p> <ul style="list-style-type: none"> <li>• Sediment fill on top</li> <li>• Disrupted reflectors below</li> <li>• Edges often fault controlled</li> <li>• Broad band</li> </ul>	

**Table 5.** Left side of table lists external and internal features seen in a karst environment. Right side of table lists attributes that quantify the internal configuration.



<b>Seismic Attribute Expression: Karst</b>					
Amplitude	Coherence	Dip	Curvature	Spectra	Texture
Low Amplitude	Low Coherence	High variable dip patterns depending on the amount of karstification	High Negative response on "sink" structures with high positive values along edge of "sink" features. Within the faults associated with the karst there is a high curvature along the dip plane and a negative curvature response on the other side of the fault plane	Low Spectral response of spectral magnitude and spectral frequency	GLCM homogeneity highlight faulted and karsted locations with low GLCM expression

**Table 6.** Summary of the seismic attribute expression of karst collapse features seen the previous figures.

Gravity Induced Deposits	Genetic Classification Transport Mechanism	Descriptive Classification Sedimentary Structures	Seismically Recognizable Features
Slide	Shear Failure along discrete shear planes with little or no internal deformation or rotation	Essentially undeformed, continuous bedding	Continuous blocks without apparent internal deformation, High-amplitude, continuous reflectors.
Slump	Shear Failure accompanied by rotation along discrete shear surfaces with various degrees of internal deformation	Plastic deformation particularly at the toe or base. Flow structures, folds, tension faults, joints, slickensides, grooves, rotational	Compressional ridges, imbricate slides, irregular upper bedding contacts, duplex structures contorted layers, Low-and high amplitude reflections geometrically arranged as though deformed through compressive
Debris Flow	Shear distributed throughout the sediment mass. Strength is principally from cohesion due to clay content. Additional matrix support may come from buoyancy. Plastic rheology and laminar state.	Matrix supported, random fabric, clast size variable, matrix variable, Rip up clasts, rafts, inverse grading and flow structures possible.	Mega rafted and/or detached blocks, irregular upper bedding contacts, lateral pinch out geometries, orientated ridges and scours. Low amplitude, semitransparent chaotic reflectors.

**Table 7.** Moscardelli and Wood (2008) description and classification of gravity flow MTDs seen in seismic data.

Classification		Casual Mechanicms	Source Area
Attached MTCs	Shelf-attached	1)Relative sea-level Fluctuations 2) High sedimentation rates	Paleoshelf edge deltas
	Slope-attached	1)Tectonism 2)Volcanism 3)Gas Hydrate Dissociation 4)Longshore currents 5)Storms and hurricanes	Upper-slope collaspses
Detached MTCS		1)Gravitational instabilities on the flanks of mud-volcano ridges/salt mass and levee channel complexes 2)Tectonic Pulses 3) Oversteepening 4)Mud-volcano activity/methane release	Flanks mud-volcano ridges/salt diapirs/levees Flanks of collapsing mid-oceanic ridges

**Table 8.** A comparison of attached versus detached mass transport complexes characterized by the location and mechanism of slope failure (After Moscardelli and Wood, 2008).

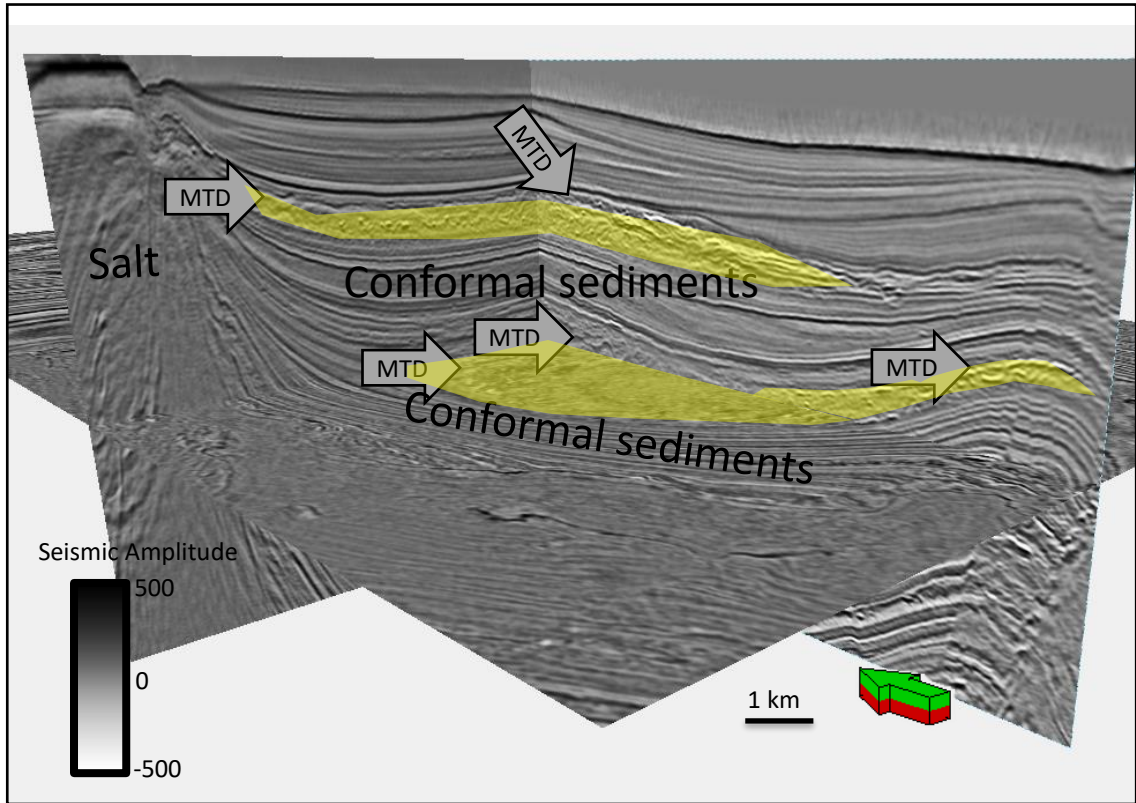


**Figure 23.** Vertical slices and a time slice at  $t=1.180$  s through the seismic amplitude volume. The MTDs exhibit chaotic reflectors within the structure as well as pinch out features at the toe of the MTD. The external features of the MTD include conformal sediment deposits both on the top and the bottom of the feature.

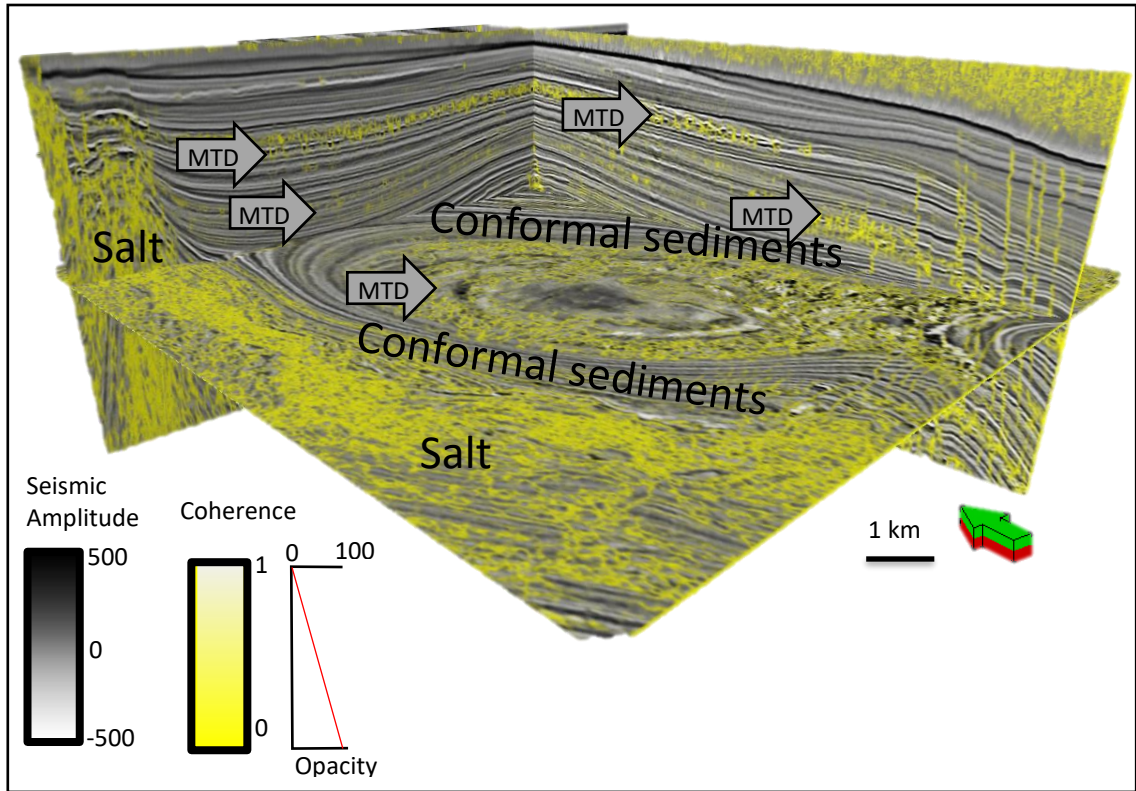


**Figure 24.** Vertical slices and a time slice at  $t=1.180$  s through the seismic amplitude and seismic coherence volume. The MTDs exhibit chaotic reflectors that are highlighted by low coherence. The salt exhibits the same coherence expression whereas the conformed sediments are high coherence.

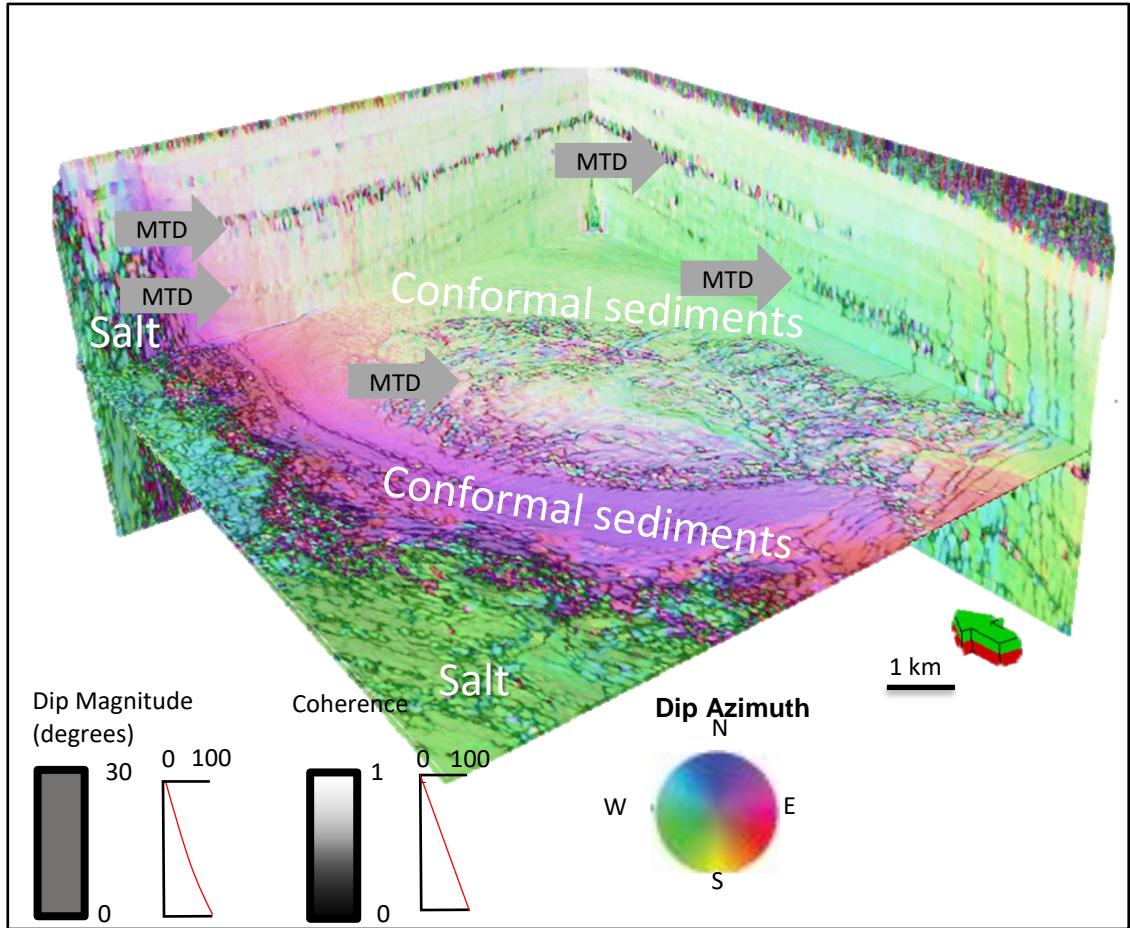


**Figure 25.** Vertical slices and a time slice at  $t=1.180$  s through corendered coherence, dip magnitude, and dip azimuth volumes. Low coherence discontinuities appear black. A layer of conformal sediments dipping to the NE appears as magenta on the SW edge of the minibasin while those dipping to the SW appear as green on the NE side of the minibasin. The chaotic, rotated blocks within the MTD dip in all directions so appear polychromatic, separated by low coherence discontinuities.



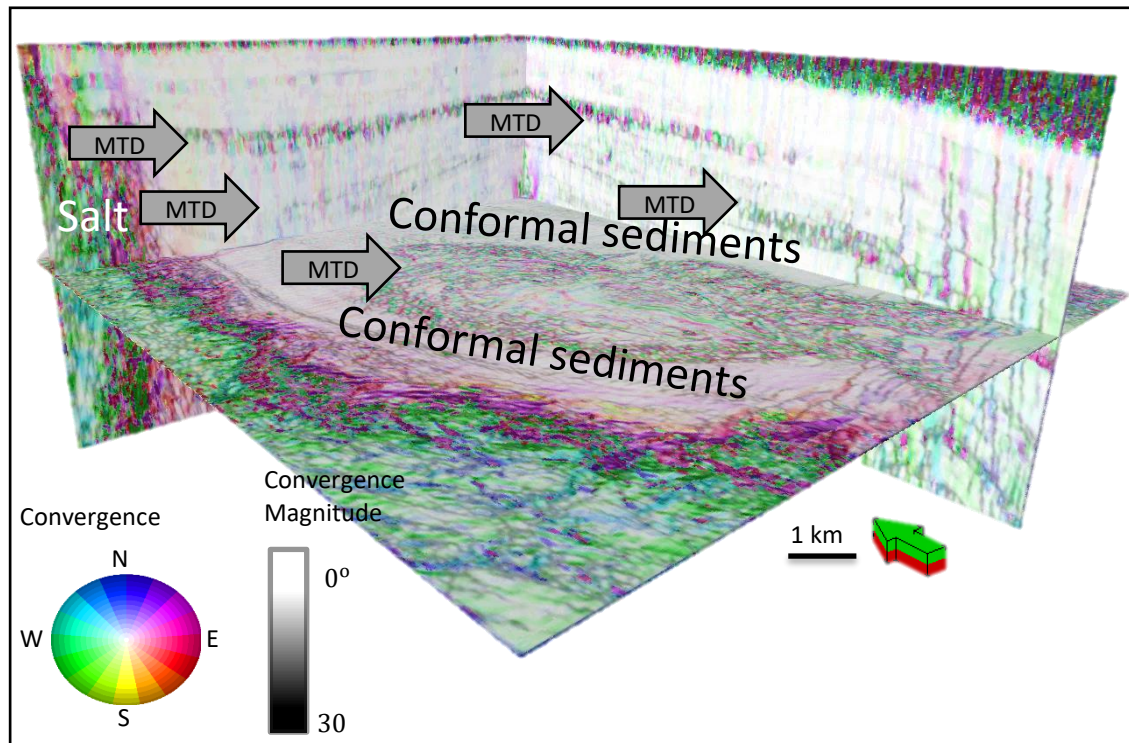


**Figure 26.** Vertical slices and a time slice at  $t=1.180$  s through corendered coherence, convergence magnitude, and convergence azimuth volumes. Low coherence values as well as chaotic convergence azimuth delineate the MTDs and the salt structures. The MTDs express variable convergence directions in the internal structure due to rotated blocks. The conformal sediments exhibit continuous convergence. The NW layered sediments converge toward the NE and the layers on the NE side of the minibasin converge SW.

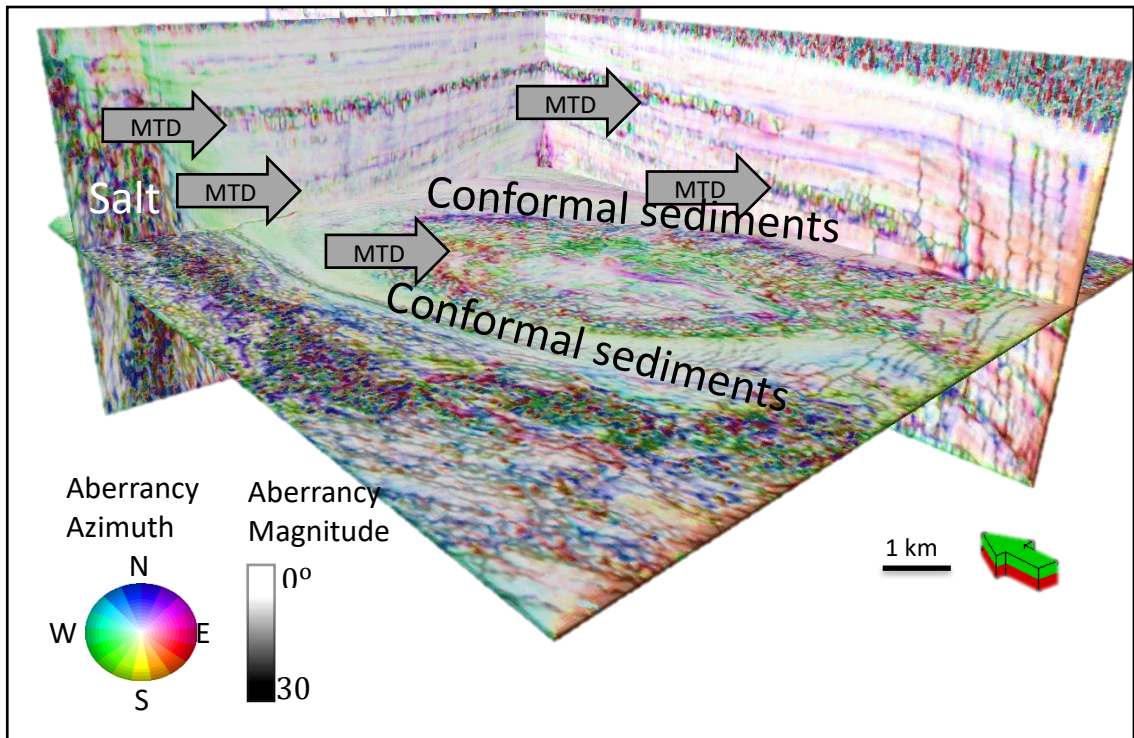


**Figure 27.** Vertical slices and a time slice at  $t=1.180$  s through corendered coherence, convergence magnitude, and convergence azimuth volumes. Low coherence values as well as chaotic convergence azimuth delineate the MTDs and the salt structures. The MTDs express variable convergence directions in the internal structure due to rotated blocks. The layered sediment exhibits continuous convergence. The NW conformal sediments converge toward the NE and the layers on the NE side of the minibasin converge SW.



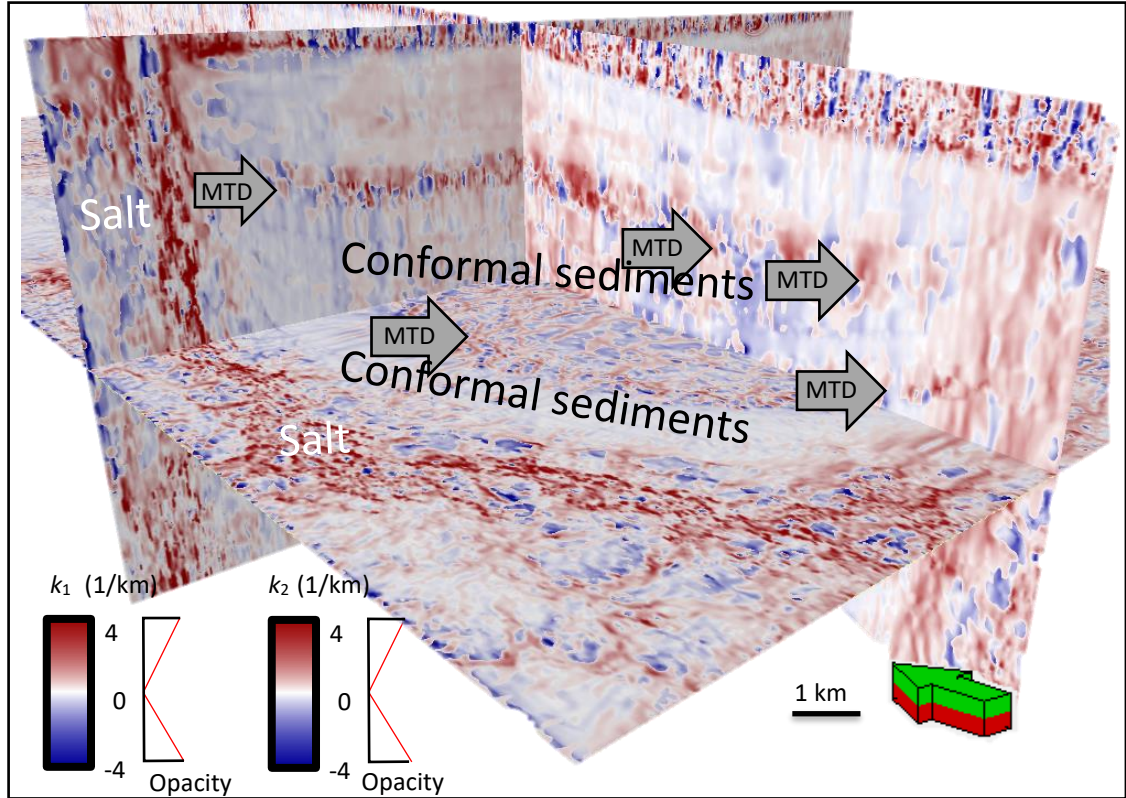


**Figure 28.** Vertical slices and a time slice at  $t=1.180$  s through the corendered most-positive and most-negative curvature ( $k_1$  and  $k_2$ ) volumes. Gray arrows indicate MTDs. The MTDs display large variations in the internal structure with the response of  $k_1$  and  $k_2$  expressed throughout the feature. The salt diapirs respond with the strongest structural anomalies internally, but in general correspond to mismigrated noise.

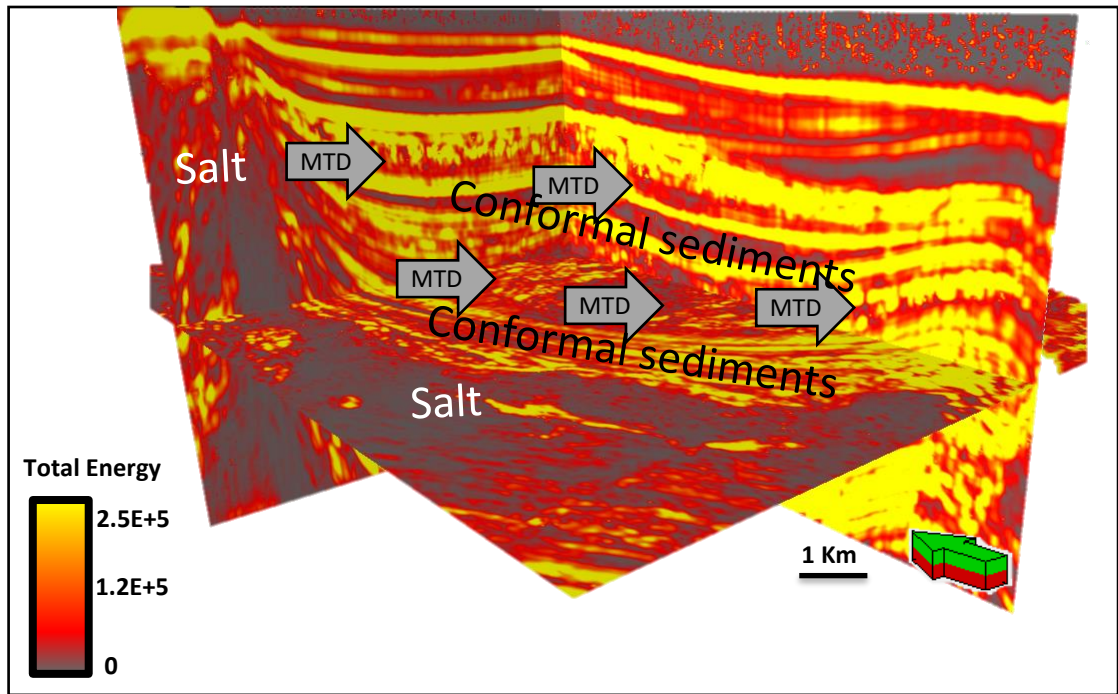


**Figure 29..** Vertical slices and a time slice at  $t=1.180$  s through total energy volume. Gray arrows indicate MTD facies that exhibit high coherent energy. In contrast, the incoherent salt diapirs exhibit low total energy.

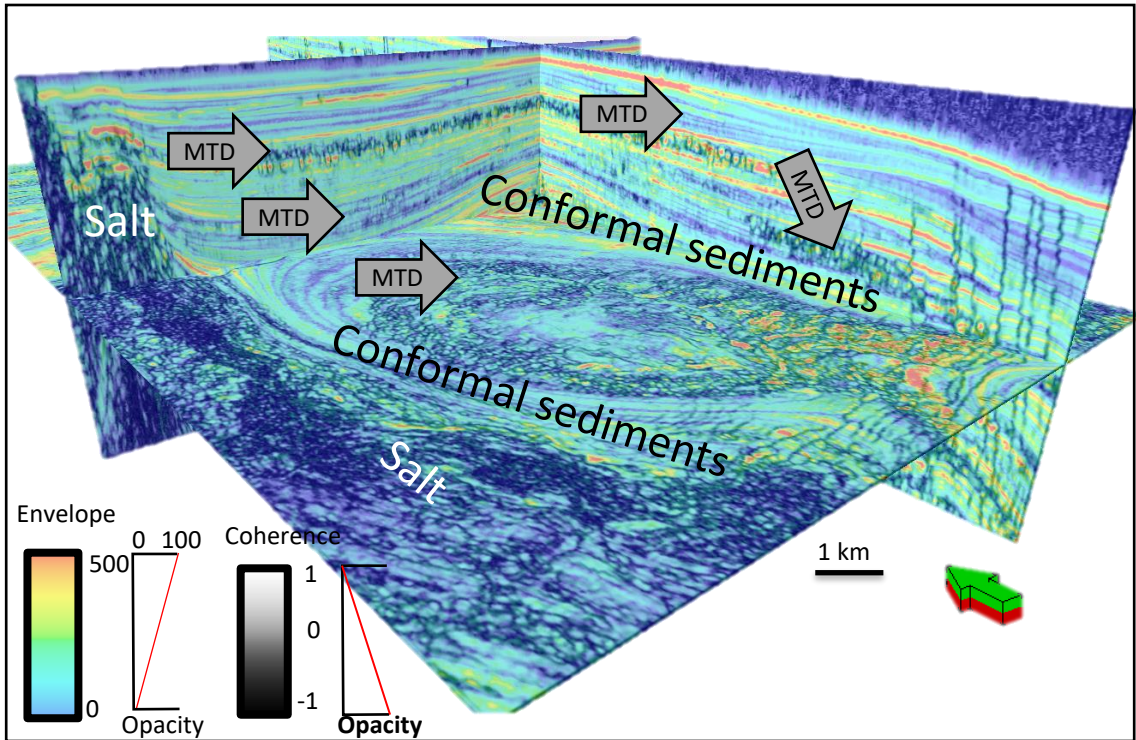


**Figure 30.** Vertical slices and a time slice at  $t=1.180$  s through corendered envelope and coherence volumes. Gray arrows indicate MTD facies which exhibit low to high envelope values. The conformal sediments and salt exhibit low envelope values.



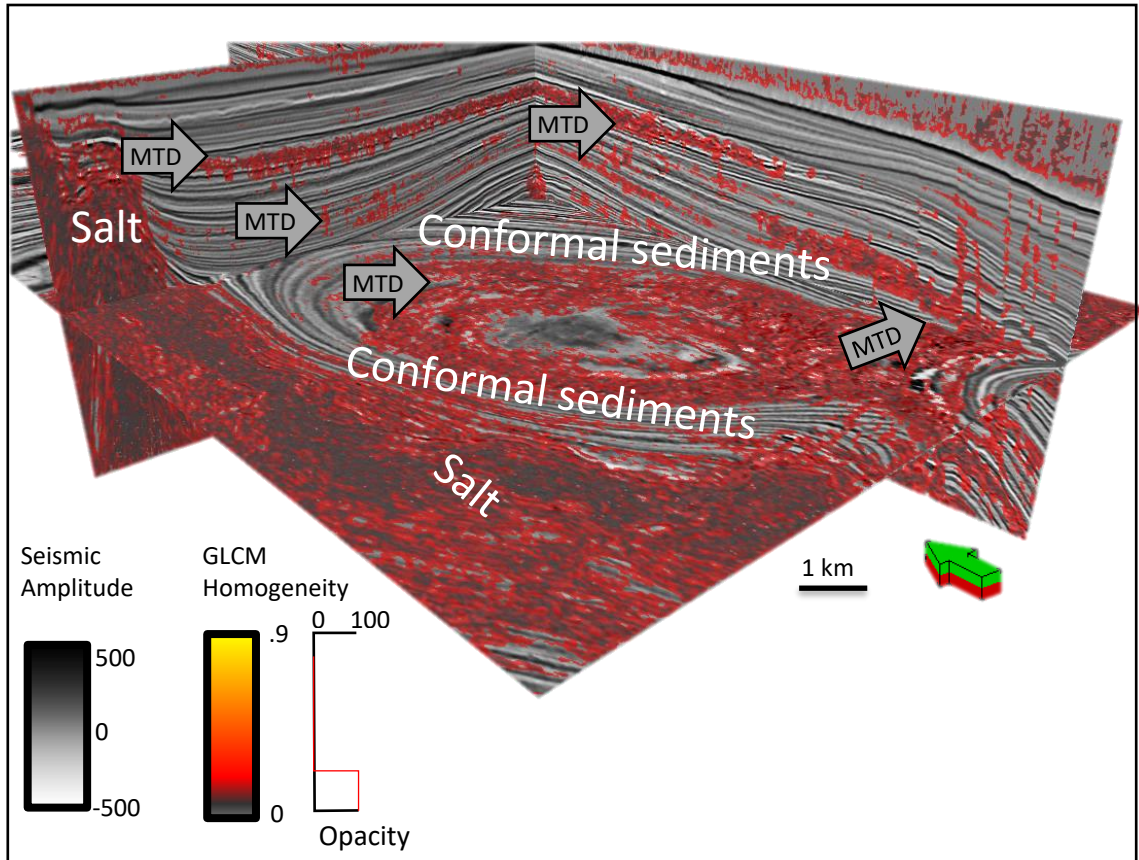


**Figure 31.** Vertical slices and a time slice at  $t=1.180$  s through corendered GLCM homogeneity and amplitude volumes. The GLCM homogeneity attribute highlights chaotic features particularly well. The MTD facies exhibit low homogeneity response within the data. The salt diapirs exhibit the same expression as the MTD as they are variable internally. The conformal sediments display high homogeneity.

<b>Reflector Response</b>	<b>Corresponding attribute</b>
<b>Internal Reflector Configuration</b> <ul style="list-style-type: none"> <li>• Discontinuous</li> <li>• Block rotation within matrix: Varying structure due to block rotation</li> <li>• Non-parallel</li> <li>• Chaotic amplitude</li> </ul>	<b>Attributes for voxel by voxel quantification</b> <ul style="list-style-type: none"> <li>• Coherence, GLCM entropy, GLCM homogeneity</li> <li>• Structural curvature</li> </ul>
<b>External Reflector Configuration</b> <ul style="list-style-type: none"> <li>• Scour surface at base</li> <li>• Impedance variation Edges often fault controlled</li> <li>• Broad band</li> </ul>	<ul style="list-style-type: none"> <li>• Dip, Reflector convergence, Parallelism</li> <li>• Peak magnitude, peak frequency, Bandwidth</li> </ul>

**Table 9.** Left side of table details MTD seismic facies summation of external and internal features for facies identification.

Right side of table lists attributes that quantify the internal configuration of the internal configuration.

### Seismic Attribute Expression: Karst

Amplitude	Coherence	Dip	Curvature	Spectra	Texture
Variable	Low Coherence	Variable dip : Degree of dip dependent on slope failure type	Variable curvature due to rotated blocks	<ul style="list-style-type: none"> <li>• Variable within the blocks</li> <li>• Upper and lower edges contain high spectra</li> </ul>	<ul style="list-style-type: none"> <li>• High dissimilarity</li> <li>• High entropy</li> <li>• Low homogeneity</li> </ul>

**Table 10.** Summary of seismic attribute expression of the MTD seismic facies shown in the previous figures.

## Chapter 5: Web-Application

The software package utilized for this thesis is called “Wix” to prototype my web application. Wix is an open platform that requires a domain name and some cost for additional functionality that are pre-defined by Wix within the platform signup. The legal terms of agreement do not provide Wix any ownership to the user data (i.e. images, videos, documents...) by the intellectual property clause within the contract in (Figure 35) where the user has complete ownership of the website (Figure 35).

The Wix platform is designer-friendly, where the Wix provides predefined templates that can be edited and applied to the web page without prior knowledge of html. The easy-to-follow guidelines within the application allow the designer to obtain help from the company at any time. The webpage is easily edited directly in the application rather than programming in html. If the user would like to program in html they may through the web-program. Within Wix the designer can import multiple files including images, tables, videos, and interactive applications. The only limitation found within the Wix web-platform is the main menu pages can only have one subdirectory page or sub-page (Figure 36).

The domain name of the website is [www.seismicfacies.org](http://www.seismicfacies.org) and the website is open to the public for usage. For editing purposes in the future, the user will have to login to the account associated with the website. Initially, editing capabilities will be limited to AASPI students and collaborators. The AASPI website is connected to this website by an internal link on the AASPI logo at the top of the menu. The user can always go to the AASPI website for additional information concerning the attributes or for an additional resource.

Within seimsicfacies.org I have created a menu consisting of *home*, *about*, *seismic facies*, *seismic amplitude* and *seismic attribute* (Figure 36). The main pages are *seismic facies*, *seismic amplitude* and *seismic attribute*. These menu pages consist of multiple sub-pages that distinguish either the feature of interest or the attribute of interest. The organization of the routing pages is for user-friendly access to the information of interest. The organization of the website such that it imitates a decision tree, based on user queries (Figure 37). For example, “I have an MTD. What will it look like in amplitude?” or “I have a chaotic feature that has low entropy values. Is it an MTD?” (Figure 38). These questions can be answered through the web-based application. This knowledge can then be applied to SOM, PCA, ICA, and neural network application.



## 3. Content and Ownership

### 3.1. Your Intellectual Property

As between Wix and you, you shall own all intellectual property pertaining to your User Content and to any other materials created by you, including to any designs, images, animations, videos, audio files, fonts, logos, illustrations, compositions, artworks, code, interfaces, text and literary works. Wix does not claim ownership rights on your content. For the sole purpose of granting you the service, You know and agree that we will need to access, upload and/or copy your User Content to our platform, including cloud services and CDN's, to make display adjustments, to duplicate for backup and perform any other technical actions and/or uses required to perform our services, as we deem fit.

### 3.2. Wix's Intellectual Property

All rights, title and interest in and to the Wix Services, including any and all copyrightable materials or any other content thereof which is or may be subject to any intellectual property rights under any applicable law (including any artwork, graphics, images, website templates and widgets, literary work, source and object code, computer code (including html), applications, audio, music, video and other media, designs, animations, interfaces, documentation, derivatives and versions thereof, the "look and feel" of the Wix Services, methods, products, algorithms, data, interactive features and objects, advertising and acquisition tools and methods, inventions, trade secrets, logos, domains, customized URLs, trademarks, service marks, trade names and other proprietary identifiers, whether or not registered and/or capable of being registered (collectively, "Intellectual Property"), and any derivations thereof, are owned by and/or licensed to Wix.

Subject to your full compliance with the Wix Terms and timely payment of all applicable Fees, Wix hereby grants you, upon creating your User Account and for as long as Wix wishes to provide you with the Wix Services, a non-exclusive, non-transferable, non-sublicensable, fully revocable, limited license to use the Wix Services and Licensed Content, for the purpose of generating and displaying your User Platform to End Users and offering your User Products (as defined below) therein, solely as expressly permitted under the Wix Terms, and solely within the Wix Services.

#### #ItsThatEasy

You own all rights to your content. We may handle your content in order to provide you with our services.

#### #ItsThatEasy

We own all rights in and to our services, content, data, technology and features.

You may use our services and content so long as you fully comply with these terms and ensure full and timely payments.

**Figure 32.** The legal language from the Wix website stating all intellectual property rights.

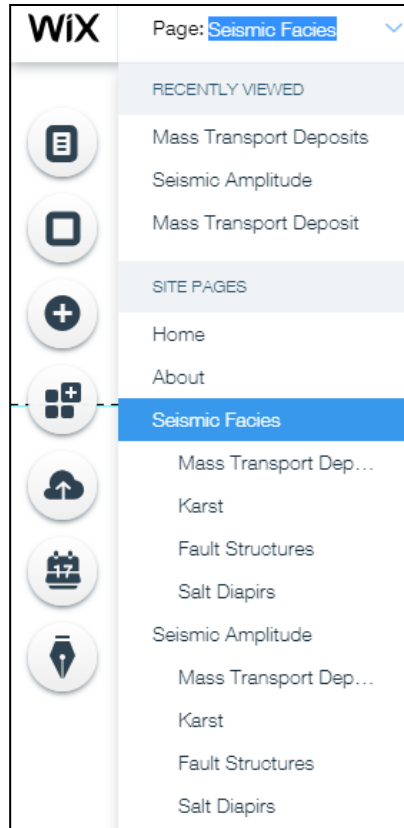


**Figure 33.** This is an image of the directory menu. The image reflects the lack of multiple internal directories.

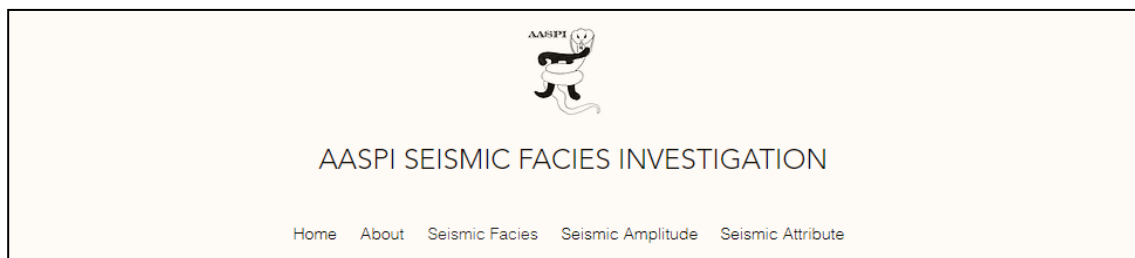


**Figure 34.** The menu of the seismicfacies.org website.

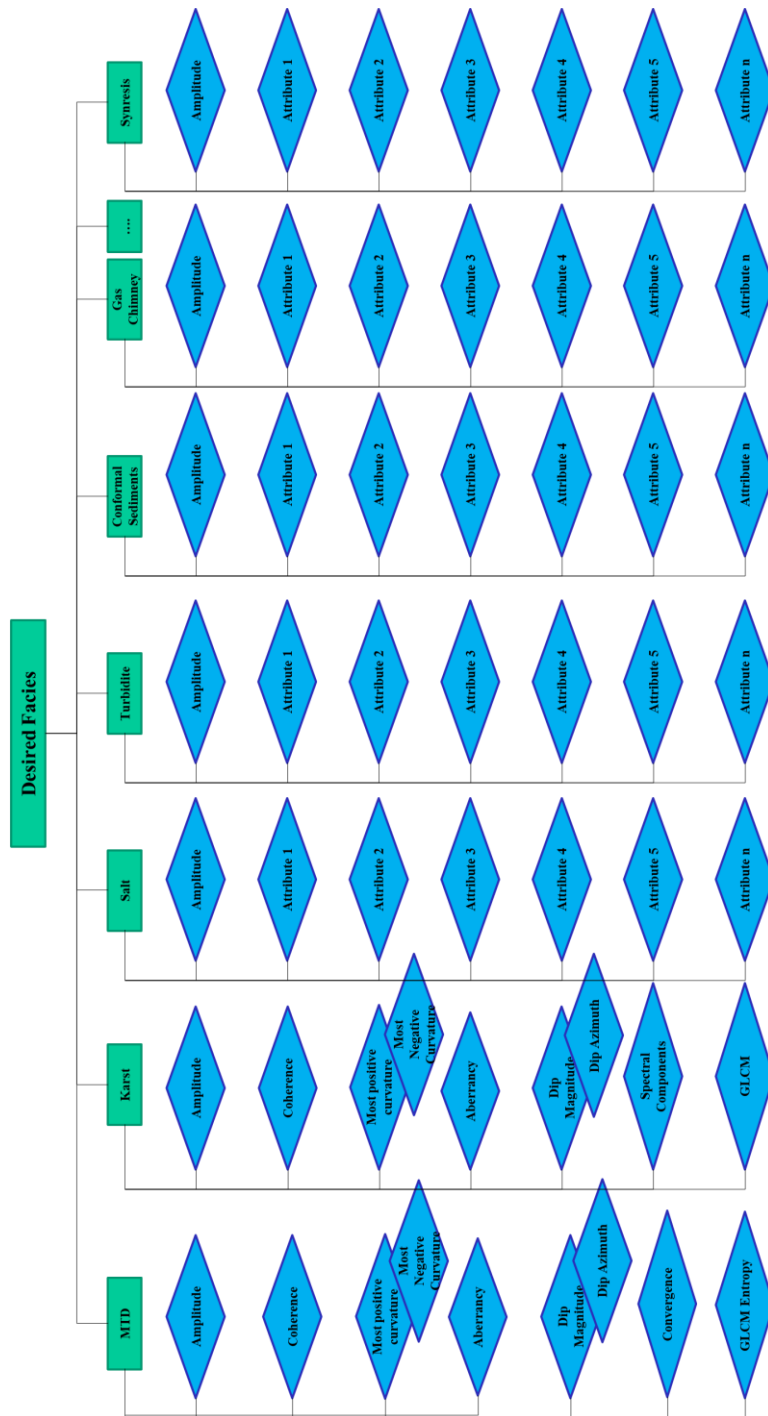


**Figure 35.** This figure is a database diagram of the facies and the attributes that best suit them. At present, the only facies investigated in this thesis are karst and MTDs. More geologic features will be added in the future.

## Chapter 6. Decision Trees

The earliest versions of geoscience decision trees were handbooks written by what are now called specialty domain experts on seismic processing and well log analysis. Since that time, decision trees have evolved into a supervised learning method used for classification and regression of large-scale data sets. The decision tree utilizes a predictive model from data points or observations guided by a series of questions to lead to a final solution (Figure 38). Decision trees built by experts provide a means to capture and disseminate best practices to a non-expert community, or if programmed, provide a means to accelerate simpler, more mundane, components of the interpretation process. Figure 38 provides an example of a decision tree that captures the interpretation process used in interpreting structural deformation. An example of a decision-tree application in seismic data is the implementation of automatic horizon picking.

The goal of this thesis is to build a more modern version of a seismic interpretation “attribute handbook,” focusing on only a few branches of the tree, or seismic facies including karst collapse and mass transport complexes. There are several advantages to a web-based system. First, it is not limited to a 2-dimensional table but rather can sort n-dimensional relations by seismic facies, by attribute, by depositional environment or by exploration objectives. Second, a web-based system can be populated by seismic 3D animations for higher quality information which can link the geologic feature to a 3-dimensional view. The examples and definitions of the seismic attributes have references to further the density of information for the user. These

references will help define the subjects that may be unclear to the user as the expected user will range in educational levels.

### **6.1 Decision Tree Background**

As the name suggests, there will be branches that are classified further into nodes (Figure 38) (Song and Lu, 2015). There are three types of nodes within a decision tree. The first is a root node which represents a choice that will result in the subdivision of all records into two or more mutually exclusive subsets. The secondary nodes are internal nodes which represent the possible choices available from that point in the tree. Finally, there are leaf nodes which encompass the final solutions. In Figure 38 the root node is the first question asked, the internal nodes are the questions that come after the root node and the leaf nodes are the final solutions or the red cylinders. The branches connect the nodes to finally come to the leaf node solution.

The larger branches may be defined by their tectonic, depositional and diagenetic geologic expression (Figure 39). There will then be subdivisions of these larger branches by the type of geologic setting such as compressional versus extensional for tectonic and lacustrine or marine environment of deposition. As the tree grows, the branches become more specific, allowing an expert interpreter to associate a given feature with one or more attributes.

In this case, the decision tree will be a support tool that utilizes data objects based on predefined input knowledge of previous work captured by journals and software packages. The decision tree within this project will go through facies, structures, and attributes that are most common elements within a geologic system. The decision tree will then be applied to a web-based application for seismic facies

interpretation. Then the decision tree will predict the “values” or geologic features of interest (Figure 40), which will serve as input to a machine learning tool (Figure 41). The user is able to use the features of the dataset within the web-based application to answer questions defining the geologic facies, the amplitude expression, and the attribute expression. The web application is used in order to identify facies using data that has already been interpreted and has applied attributes. The role of the decision tree in this work is simply to choose those attributes that are good candidates for subsequent machine-learning facies prediction using a random decision tree method (Kim, 2018) (Figure 40).

#### *6.1.1 Random Forest Decision Tree Application*

Kim (2018) utilizes a random forest algorithm utilizing an ensemble of decision trees, in this case trained by a bagging or bootstrap aggregation. The benefit of a decision tree is the ability to identify redundant and pertinent attributes with a quantitative measure for each attribute for a given facies. While a decision tree is a white box algorithm, a random method takes advantage of decision trees but alleviates overfitting of training data. The Random Forest decision tree application is less biased than a decision tree alone since it integrates individual trees rather than a whole tree. The application of a decision tree forest results in a higher accuracy rate of predication. Both the decision tree and the random forest algorithms predict multiple classes that are available rather than one individual class.

The random forest method takes many decision trees which have a root node to a leaf node to make repeated predictions of the training data as the input (Breiman, 2001). Breiman defines random forest as a “classifier consisting of a collection of tree-structured

classifiers  $\{h(x, k), k = 1, 2, \dots\}$  where the  $\{k\}$  are independent identically distributed random vectors and each tree casts a unit vote for the most popular class at input  $x$ ." The random forest method uses a subset of training data that are randomly chosen and then replaced for several times equal to the number of trees in the ensemble (Carranza and Laborte, 2014). The random forest decision tree method is the bootstrap aggregation method for random decision trees. This allows two thirds of the training samples to be used for prediction accuracy. For each split in the decision tree, a random selection of the predictor variables is made. Then the prediction output is based on the average of the predictors of all the regression trees.

The random forest method has been utilized in predicting surface lithology classes from airborne geophysical data, topographic data for mineral locations, or remote sensed satellite data (Ham et al., 2005; Pal, 2005; Waske et al., 2009; Duro et al., 2012; Carranza and Laborte, 2014). Uncertainty estimates in prediction of lithology contact zones or in lithology mapping suggest random forest algorithm recovers data points better than inherent dependencies over spatially varying input data than support vector machine algorithm (Cracknell and Reading, 2016).

The byproduct of random forest algorithms is variable importance (Breiman, 2001b; Liaw and Wiener, 2002). Some attributes are more efficient and accurate predictors, and other attributes may include little information for prediction. Selecting attributes which contribute best to classification can speed up the process and improve prediction accuracy. 3D seismic in geophysical exploration are large-scale data. Since computation time is proportional to the number of variables and size of the data set, reducing dimensionality is crucial for learning algorithms. Selecting appropriate features

is important in machine learning algorithms. Some features are more powerful for classification, and others may be redundant. Reduction of dimension based on feature selection can speed up the learning process, as well as improve prediction accuracy. For this process the most pertinent attributes and facies are identified by the random forest decision tree method.

Botanical trees are three dimensional. Our decision tree will in general be higher dimensional. In addition to the tree major branches described above, knowledge of the geologic environment will provide improved interpretation. In terms of structural features, are we in a compressional, extensional, or strike-slip regime? Are we in environment conducive to carbonate, evaporite, or volcanic features? Is the environment fluvial, lacustrine, or deep water? These additional “dimensions” are routinely used by human interpreters to set the context for observed seismic features.



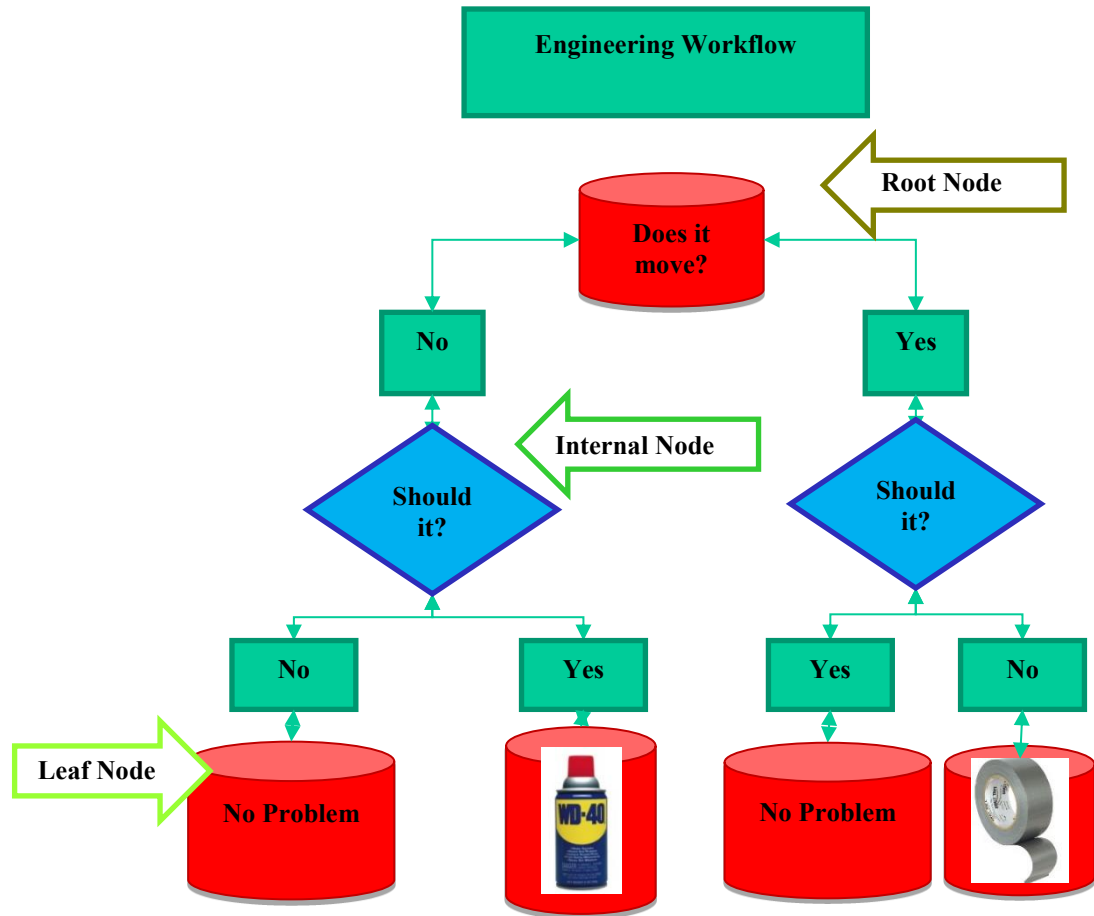


**Figure 36.** A simplified example of a decision tree to identify the root node, the internal nodes, and the leaf node.

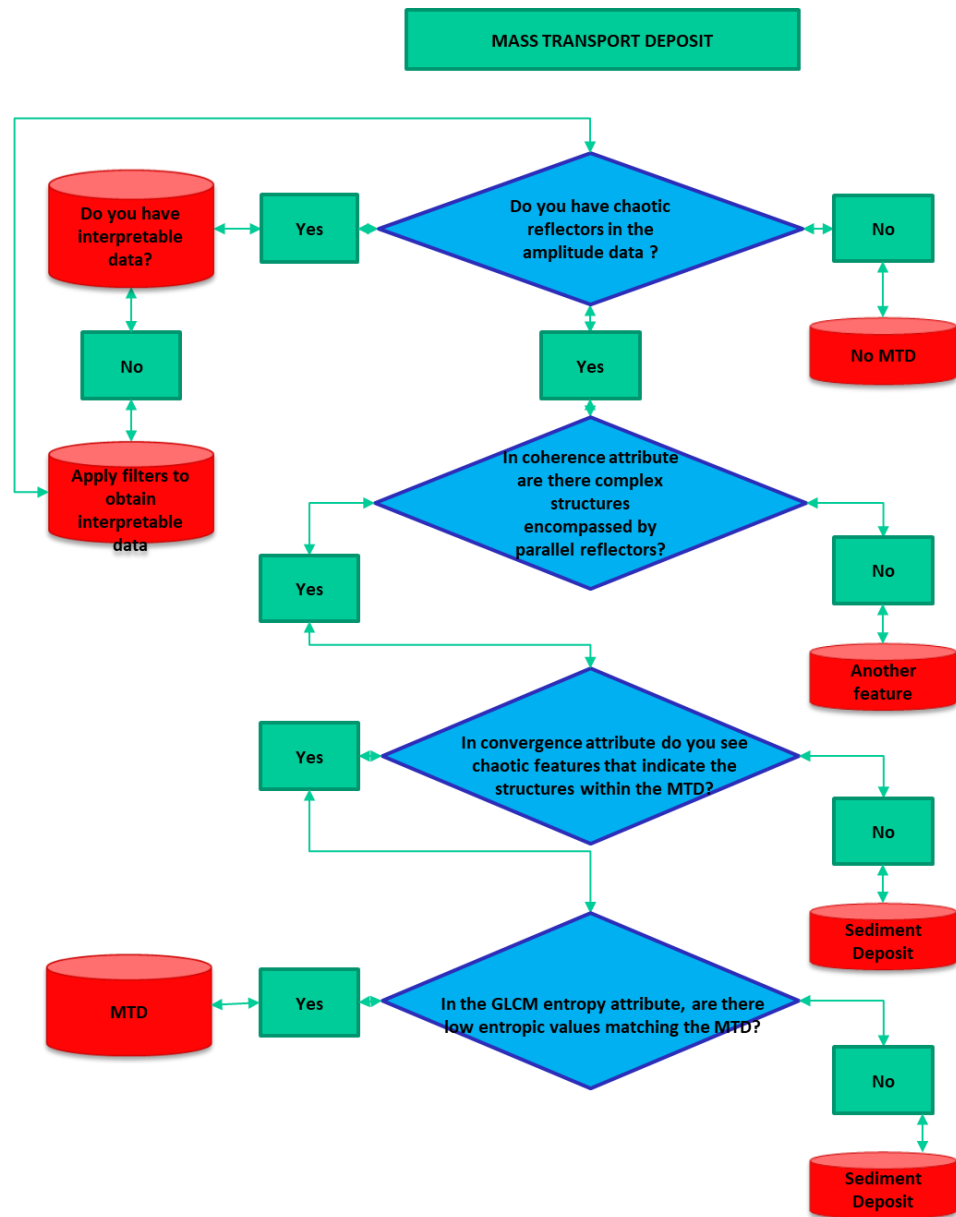


**Figure 37.** A simplified decision tree for MTD identification within seismic datasets.

The decision tree in this figure depicts the nature of a decision tree as well as the thought processes of a seismic interpreter to identify the geologic feature of interest utilizing seismic attributes.

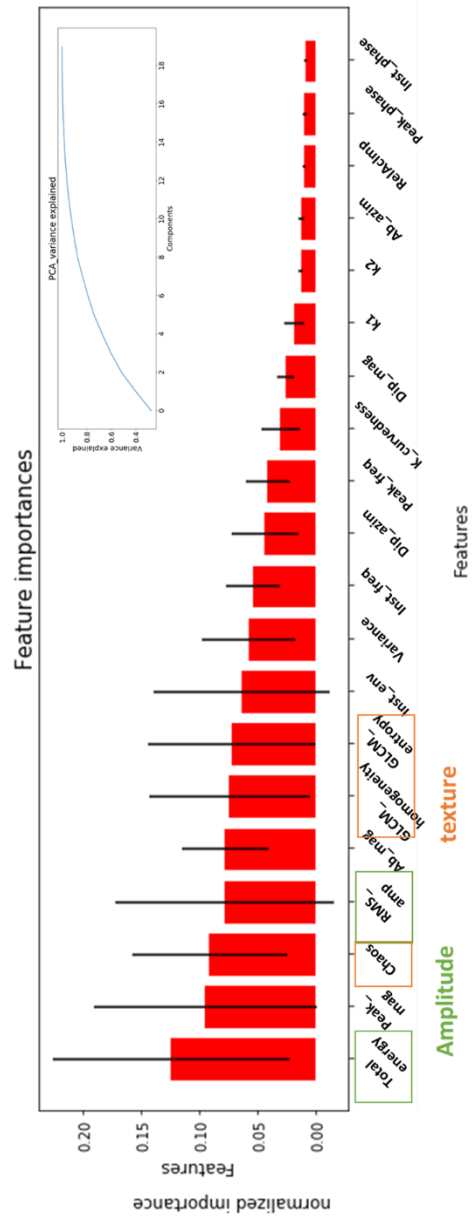


**Figure 38.** A chart of the normalized features regarding the attributes. The best attribute identified by Kim (2018) are total energy, peak magnitude, chaos, RMS (root mean square) amplitude, absolute magnitude and GLCM entropy and homogeneity.

## Chapter 7: Limitations and Conclusions

The most challenging aspect in constructing such an application are the thought processes (geopsychological analysis) of the skilled interpreter – what do they see when they identify a specific geological feature, and how can this pattern be quantified by seismic attributes or a decision tree workflow?

Seismic data quality can be as important as geology in attribute selection. While some features, such as faults and karst collapse can be classified voxel by voxel, other features, such as progradations and meandering channels need to be placed in context of the geologic features seen above, below and around the target of interest to confirm the interpretation. Such *in context* analysis falls into the computer vision domain of *scene analysis*.

Seismic attributes capture and quantify many of the variations in seismic amplitude, continuity, orientation, and texture used by human interpreters. However, human interpreters typically analyze such features in context with surrounding facies coupled with an understanding of the depositional environment. To be useful for simple machine learning techniques, these attributes must be able to differentiate the target facies at a voxel-by-voxel granularity. Post attribute processing, such as Kuwahara filtering proposed by Qi et al. (2016) partially addresses this challenge. Convolutional neural networks may provide similar advantages. In the meantime, we have constructed the first web page to link a given seismic facies to the attributes that delineates the features expressed in this thesis.

The web-based application applies the knowledge of previously published papers and current attribute application practices to create a workflow, a database, and

an attribute taxonomy to answer the question “what attribute identifies the desired facies from the surrounding facies?” The web-based application is limited to two facies which are MTDs and karst seismic facies. These facies are expressed well in seismic data and exhibit distinct attribute expression in geometric-based attributes as well as textural attributes.

In the future, I would like to see this website evolve into a larger database and workflow for more facies and attribute application to develop a SEG Wiki. This will be the most useful tool to create a database for machine learning or to apply this knowledge to SOM, ICA, or PCA. As this website grows into a living documentation of seismic facies and attributes it can be applicable to many questions that are being asked by professionals, students and academics.

## References

- Amtmann, J., C. Eichkitz, and M. Schreilechner, 2013, Seismic attribute database for selective use of seismic attributes for a given application: AAPG Search and Discovery #41163, [http://www.searchanddiscovery.com/pdfz/documents/2013/41163amtman/ndx\\_amtmann.pdf.html](http://www.searchanddiscovery.com/pdfz/documents/2013/41163amtman/ndx_amtmann.pdf.html)
- Barnes, A., and K. J. Laughlin, 2002, Comparison of methods for unsupervised classification of seismic data: 64<sup>th</sup> Annual Meeting of the EAGE, Expanded Abstracts.
- Barnes, A., 2016, Handbook of Poststack Seismic Attributes: Geophysical Reference Series **21**.
- Barnes, A., 2007, Redundant and useless seismic attributes: Geophysics, **72**, P33-P38, <https://doi.org/10.1190/1.2716717>
- Barnes, A.E. 2001, Seismic attributes in your facies: CSEG Recorder, **26**, P41-47, accessed 19, April 2018; <http://74.3.176.63/publications/recorder/2001/09sep/sep01-seismic-attributes-facies.pdf>.
- Brown, A. R., 2001, Seismic attributes and their classification: Geophysics, **66**, P47-48, doi: <https://doi.org/10.1190/1.1437208>.
- Breiman, L., 2001, Random forests: Machine Learning, **45**, 5-32.
- Bull, S., J. Cartwright, and M. Huuse, 2009, A review of kinematic indicators from mass transport complexes using 3D seismic data: Marine and Petroleum Geology, 1132-1151, doi: <https://doi.org/10.1016/j.marpetgeo.2008.09.011>.
- Carranza, E.J.M, and A. Laborte, 2014, Random forest predictive modeling of mineral prospectivity with small number prospects and data with missing values in Abra (Philippines): Computers and Geosciences, **74**, 60-70, doi: <https://doi.org/10.1016/j.cageo.2014.10.004>.
- Cazarin, C., R. Ennes-Silvia, F. Bezerra, L. Borghi, A. Auler, and A. Klimchouk, 2016, Hypogenic karst dissolution in carbonate rocks has implications for karstified carbonate reservoirs: Annual Convention and Exhibit with SEPM, AAPG, Article 41792, doi: 10.13140/RG.2.1.3115.3761.
- Chen, Q., and S. Sidney, 1997, Advances in seismic attribute technology: 77<sup>th</sup> Annual International Meeting of the SEG, Expanded Abstracts, 730-733, accessed on 19, April 2018, <https://doi.org/10.1190/1.1886114>.

- Chopra, S., and K. J. Marfurt, 2007, Seismic Attributes for Prospect Identification and Reservoir Characterization: Geophysical Development Series **11**, Society of Exploration Geophysics, doi: <https://doi.org/10.1190/1.9781560801900>.
- Coléou T., M. Poupon, and K. Azbel, 2003, Unsupervised seismic facies classification: A review and comparison of techniques and implementation: The Leading Edge, **22**, 942-953, accessed on 19, April 2018, doi: <https://doi.org/10.1190/1.1623635>.
- dGB Earth Sciences, 2018, OpenDtect, [http://doc.opendtect.org/5.0.0/doc/dgb\\_userdoc/Default.htm#def\\_attr\\_sets/def\\_attr\\_sets/def\\_attr\\_sets.htm](http://doc.opendtect.org/5.0.0/doc/dgb_userdoc/Default.htm#def_attr_sets/def_attr_sets/def_attr_sets.htm), accessed 15 April 2018.
- Duro, D., 2012, Multi-scale object-based image analysis and feature selection of multi-sensor earth observation imagery using random forests: International Journal of Remote Sensing, **33**, 4502-4526, doi: <https://doi.org/10.1080/01431161.2011.649864>.
- Gong, Y. Wang, D. M. Hodgson, W. Zhu, W. Li, Q. Xu, and D. Li, 2014, Origin and anatomy of two different types of mass-transport complexes: A 3D seismic case study from the northern South China Sea margin: Marine and Petroleum Geology, **54**, 198-215, doi: <https://doi.org/10.1016/j.marpetgeo.2014.03.006>.
- Ham, J., Y. Chen, M. M. Crawford, and J. Gosh, 2005, Investigation of the random forest framework for classification of hyperspectral data: IEEE Transactions, Geoscience and Remote Sensing, **43**, 492-501, accessed 19, April 2018; <https://ieeexplore.ieee.org/stamp/stamp.jsp?tp=&arnumber=1396322>.
- Henderson J., S. J. Purves, G. Fisher, and C. Leppard, 2008, Delineation of geological elements from RGB color blending of seismic attribute volumes: The Leading Edge, **27**, 342-350, doi: <https://doi.org/10.1190/1.2896625>.
- Infante-Paez, L., and K. J. Marfurt, 2017, Seismic expression and geomorphology of igneous bodies: A Taranaki Basin, New Zealand case study: Interpretation, **5**, SK121-SK140, doi: <https://doi.org/10.1190/INT-2016-0244.1>.
- Kalkomey, C.T, 1997, Potential risks when using seismic attributes as predictors of reservoir properties: Leading Edge, **16**, 247-251, doi: <https://doi.org/10.1190/1.1437610>.
- Liaw, A., and M. Wiener, 2002, Classification and regression by random forest: R News, **2/3**, ISSN 1609-3631.

- Loucks, R. G., 2008, Review of the lower Ordovician Ellenburger group of the Permian basin, West Texas, [http://www.beg.utexas.edu/resprog/permianbasin/PBGSP\\_members/writ\\_synth/Ellenburger%20report .pdf](http://www.beg.utexas.edu/resprog/permianbasin/PBGSP_members/writ_synth/Ellenburger%20report.pdf), accessed 9 April 2018.
- Lubo-Robles, D., and K. Marfurt, 2017, Delineation of thick incised canyons using spectral-decomposition analysis, curvature and self-organizing maps in the Exmouth Plateau, Australia: 87<sup>th</sup> Annual International Meeting of the SEG, Expanded Abstracts, 2420-2424, doi: <https://doi.org/10.1190/segam2017-17790008.1>.
- Marfurt, K., and T. M. Alves, 2015, Pitfalls and limitations in seismic attribute interpretation of tectonic features: Interpretation, **3**, SB5-SB15, doi: <https://doi.org/10.1190/INT-2014-0122.1>.
- Marfurt, K., 2015, Techniques and best practices in multiattribute display: Interpretation, **3**, B1-B23, doi: <https://doi.org/10.1190/INT-2014-0133.1>.
- Milad, B., 2017, The Effect of karsting on natural fracture, hardness, and brittleness of the Hunton Limestone and paleo-deposition of the Woodford Shale: A study using 3-D seismic, outcrop, well log, and core data: AAPG Search and Discovery Article #51417.
- Milad, B., and R. Slatt. 2017, Integrated 3-D seismic, outcrop, and core data for characterization of natural fractures of the Hunton Limestone and the Woodford Shale in Central Oklahoma: AAPG Search and Discovery Article #51382.
- Meldahl, P., and R. Heggland, 1999, The chimney cube, an example of semi-automated detection of seismic objects by directive attributes and neural networks: Part I; methodology: 69<sup>th</sup> Annual International Meeting of the SEG, Expanded Abstracts, 931-934, doi: <https://doi.org/10.1190/1.1821262>.
- Meldahl, P., R. Heggland, B. Bril, and P. de Groot, 2001, Identifying faults and gas chimneys using multiattributes and neural networks: The Leading Edge, **20**, 474-482, <https://doi.org/10.1190/1.1438976>.
- U.S Department of the Interior, 2007, Natural Resource Report, 2007, Carlsbad Caverns National Park, accessed 19, April 2018; [https://nature.nps.gov/geology/inventory\\_embed/publications/reports/cave\\_gr\\_pt\\_body\\_print.pdf](https://nature.nps.gov/geology/inventory_embed/publications/reports/cave_gr_pt_body_print.pdf)
- Olafiranye, K., C.A.-L. Jackson, and D. M. Hodgson, 2013, The role of tectonics and mass-transport complex emplacement on upper slope stratigraphic evolution: A



3D seismic case study from offshore Angola: *Marine and Petroleum Geology* **44**, 196–216, doi: <https://doi.org/10.1016/j.marpetgeo.2013.02.016>.

- Pal, M., 2005, Random forest classifier for remote sensing classification: *International Journal of Remote Sensing*, **26**, 217–222, doi: <https://doi.org/10.1080/01431160412331269698>.
- Pigott, J.D., M-H. Kang, and H-C. Han, 2013, First order seismic attributes for clastic seismic facies interpretation: examples from the East China Sea: *Journal of Asian Earth Science*, **66**, PG 34-54, doi: <https://doi.org/10.1016/j.jseaes.2012.11.043>.
- Qi, J., T. Lin, T. Zhao, F. Li, and K. Marfurt, 2016, Semisupervised multiattribute seismic facies analysis: *Interpretation*, **4**, no. 1, SB91-SB106, doi: <https://doi.org/10.1190/INT-2015-0098.1>.
- Qi, J., G. Machado, and K. Marfurt, 2017, A workflow to skeletonize faults and stratigraphic features: *Geophysics*, **82**, 1–14, doi: <https://doi.org/10.1190/segam2017-17675414.1>.
- Qi, J., H. Gu, F. Li, and K. Marfurt, 2017, Multiazimuth coherence: 87<sup>th</sup> Annual International Meeting of the SEG, Expanded Abstracts, 2096-2101.
- Qi, X., and K. Marfurt, 2018, Volumetric aberrancy to map subtle faults and flexures: *Interpretation*, **6**, no. 2, T349-T365, doi: <https://doi.org/10.1190/segam2017-17632807.1>.
- Qi, X., K. J. Marfurt, M. Pranter, and S. Cook, 2017, Calibrating volumetric aberrancy fracture prediction using borehole image logs and mud logs, application to the Mississippian limestone: 87<sup>th</sup> Annual International Meeting of the SEG, Expanded Abstracts, 2400-2404, doi: <https://doi.org/10.1190/segam2017-17633192.1>.
- Roy, A., T. Zhao, V. Jayaram, and D.K. Devegowda, 2015, Well performance predictions from geologic, petrophysical and completions-related parameters using generative topographic mapping: A field case study: 85<sup>th</sup> Annual International Meeting of the SEG, Expanded Abstracts, 2853-2857, doi: <https://doi.org/10.1190/segam2015-5916229.1>.
- Russell, B., D. Hampson, J. Schuelke, and J. Quirein, 1997, Multiattribute seismic analysis: *The Leading Edge*, **16**, no. 10, 1439-1444, doi: <https://doi.org/10.1190/1.1437486>.

- Slatt, R., 2006, Stratigraphic Reservoir Characterization for Petroleum Geologists, Geophysicists, and Engineers, Elsevier Inc.
- Stafford, K., R. Nance, L. Rosales-Lagarde, and P. Boston, 2008, Epigene and hypogene gypsum karst manifestations of the Castile Formation: Eddy County, New Mexico and Culberson County, Texas, USA: *International Journal of Speleology*, **37**, 83-98.
- Taner, M., 2003, Attributes Revisited, *Rock Solid Attributes*; <http://www.rocksolidimages.com/attributes-revisited/>.
- Torres-Parada, E., R. M. Slatt, K. Marfurt, L. Infante, and L. Castillo, 2017, Identification of potential lacustrine stratigraphic intervals in the Woodford Shale, Oklahoma, using multi-attribute 3-D seismic displays and a supervised neural network: Unconventional Resources Technology Conference, Extended Abstract, 2802-2814.
- Waske, B., 2009, Classifier ensembles for land cover mapping using multitemporal SAR imagery: *ISPRS Journal of Photogrammetry and Remote Sensing*, **64**, 433-512, doi: <https://doi.org/10.1016/j.isprsjprs.2009.01.003>.
- West, B., S. R. May, J. E. Eastwood, and C. Rossen, 2002, Interactive seismic facies classification using textural attributes and neural networks: *The Leading Edge*, **21**, P1042-1049, doi: <https://doi.org/10.1190/1.1518444>.
- Zhao, T., J. Zhang, F. Li, and K. Marfurt, 2016, Characterizing a turbidite system in Canterbury Basin, New Zealand, using seismic attributes and distance-preserving self-organizing maps: *Interpretation*, **4**, SB79-SB89, doi: <https://doi.org/10.1190/INT-2015-0094.1>.

## **Appendix A: Data Conditioning**

The 3D seismic dataset used for MTD facies analysis covers an area of 8000 km<sup>2</sup> offshore Louisiana's shelf edge. The seismic data were acquired by PGS using towed streamers with two sources and three receiver cables with a maximum offset of 6000 m. The seismic data contains large minibasins formed from salt withdrawal. The salt withdrawal created large diapiric salt structures resulting in sediment destabilization resulting in massive gravity flows or MTDs. Migration aliasing and other limitations in the acquisition and processing gave rise to high-amplitude cross-cutting noise cutting lower-amplitude stratigraphic reflector. Multiples converted waves, and migration artifacts contaminate the interior of the salt domes with steeply dipping, chaotic events. In both cases, relatively strong, steeply dipping noise events can juxtapose weaker, relatively flat stratigraphic reflectors, resulting in high amplitude curvature impulse responses (Figure A1). To mitigate this problem, I first applied a lower-upper-median (LUM) filter to the volumetric dip components and then applied a structurally oriented filter to the seismic amplitude data (Figure A2). Figure A3 shows that these artifacts are no suppressed.

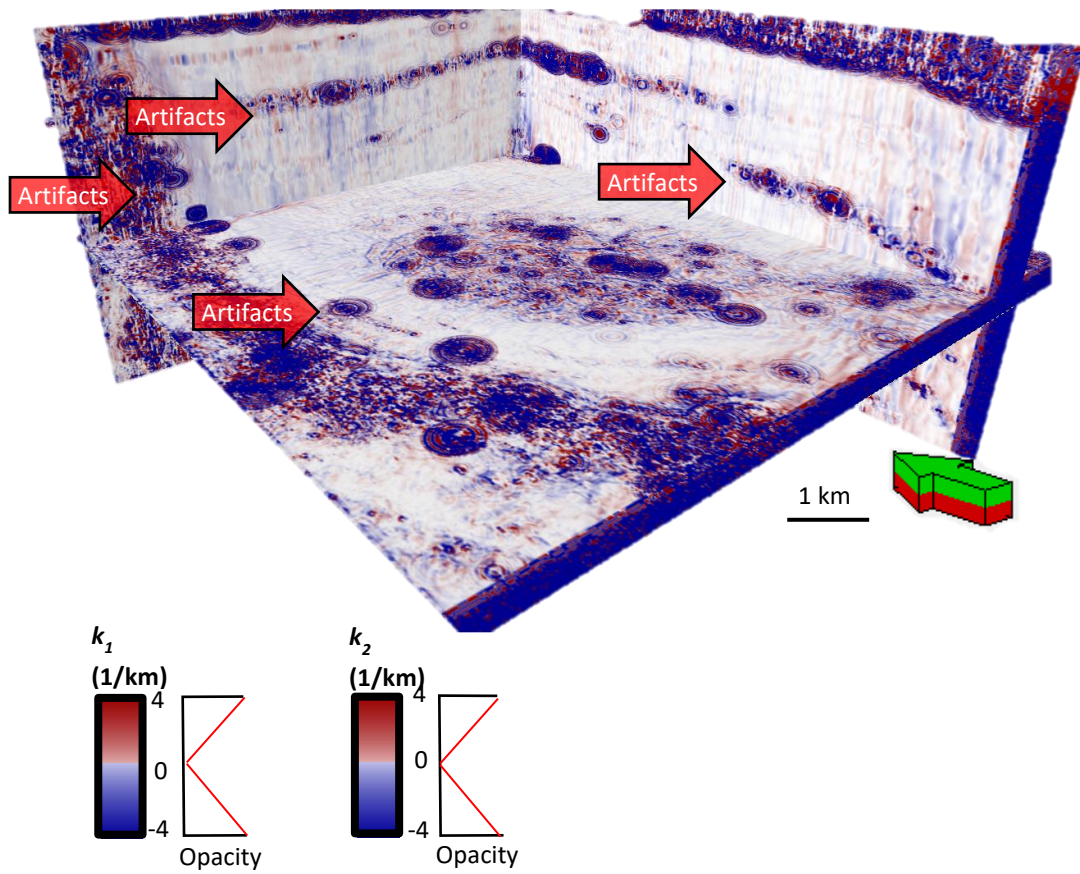


**Figure A1.** Vertical slices with a time slice at  $t=1.180$  s through co-rendered most-positive and most-negative curvature volumes. Red arrows indicate artifacts due to rapid lateral changes in structural dip, usually associated with high-amplitude cross-cutting noise cutting a low-amplitude stratigraphic reflector.

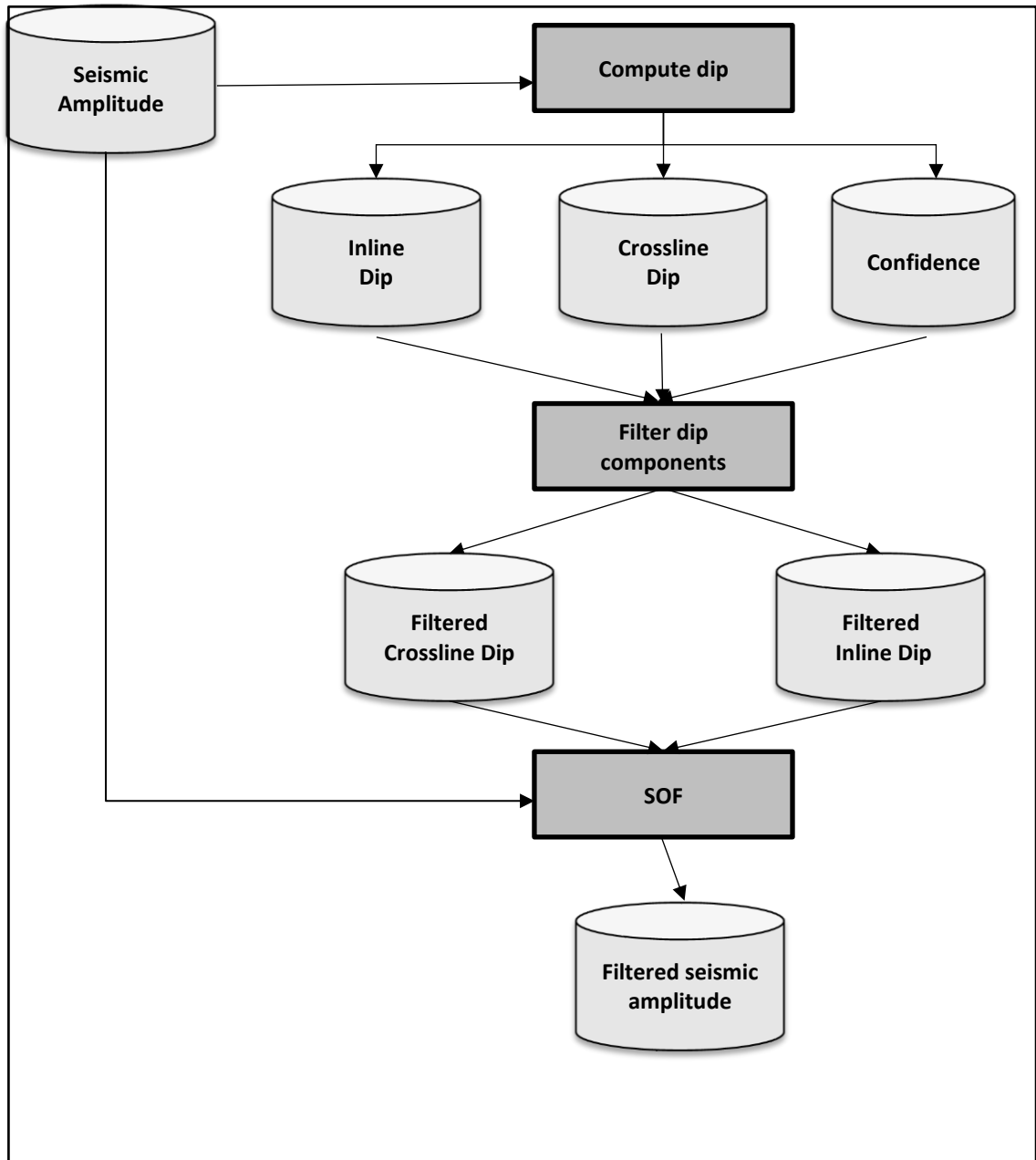


**Figure A2.** Structure-oriented filter workflow that suppresses both erratic dip estimates and crosscutting noise in the seismic amplitude volume. If necessary, the filtered seismic data may be used as input for a second pass of filtering.

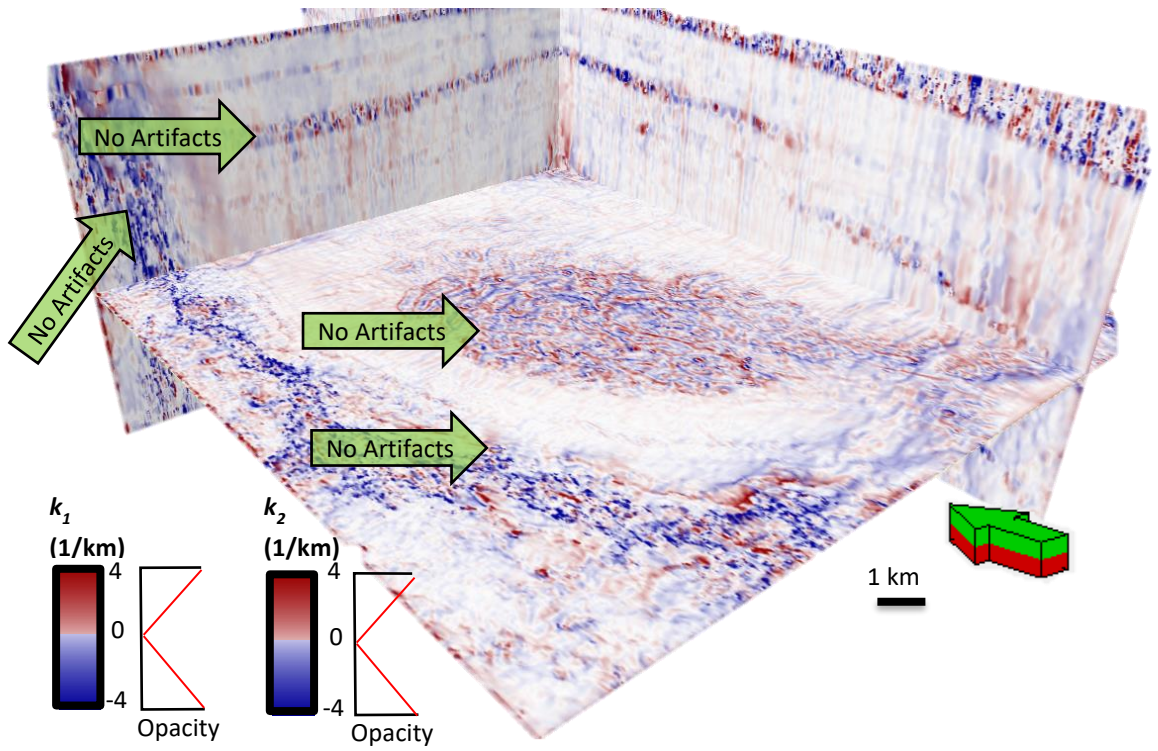
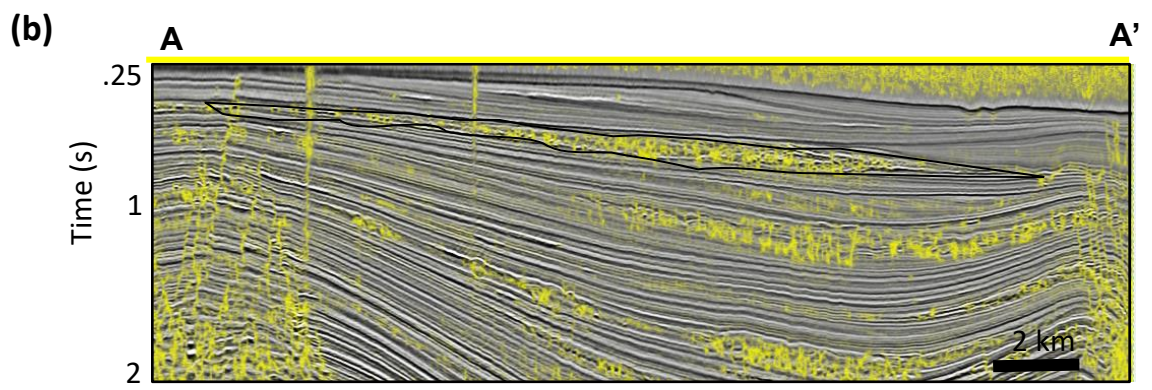
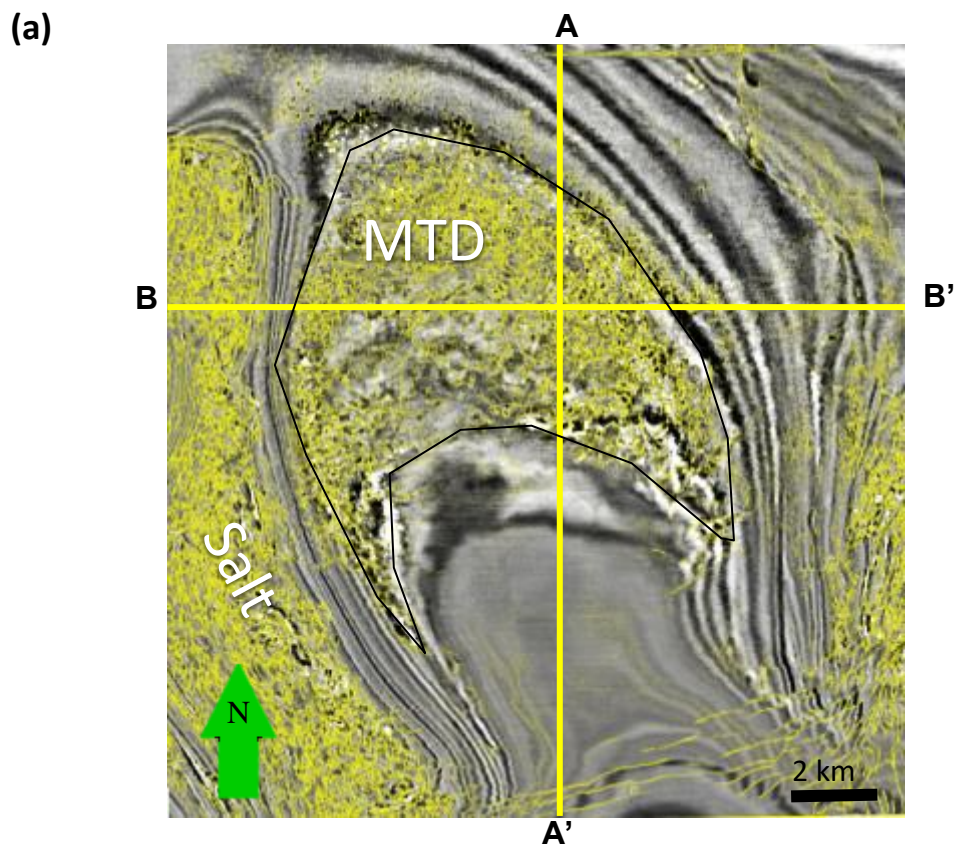


**Figure A3.** Vertical slices with a time slice at  $t=1.180$  s through the structural curvature volume. The green arrows indicate areas where artifacts have been removed by the workflow in Figure A1.

## **Appendix B: Attribute Expression of a Mass Transport Deposit**

In this appendix I provide images of a Gulf of Mexico mass transport deposit for the suite of attributes listed in Table 5.







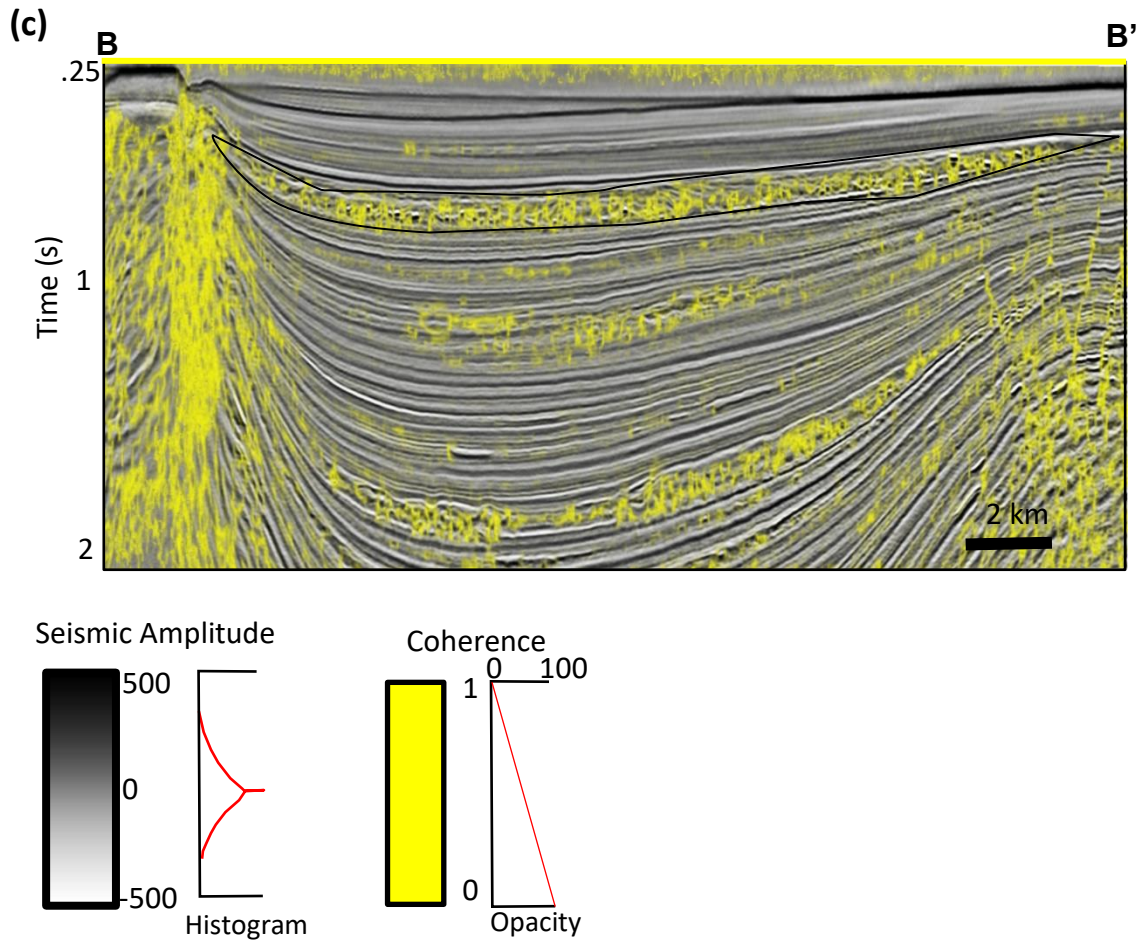
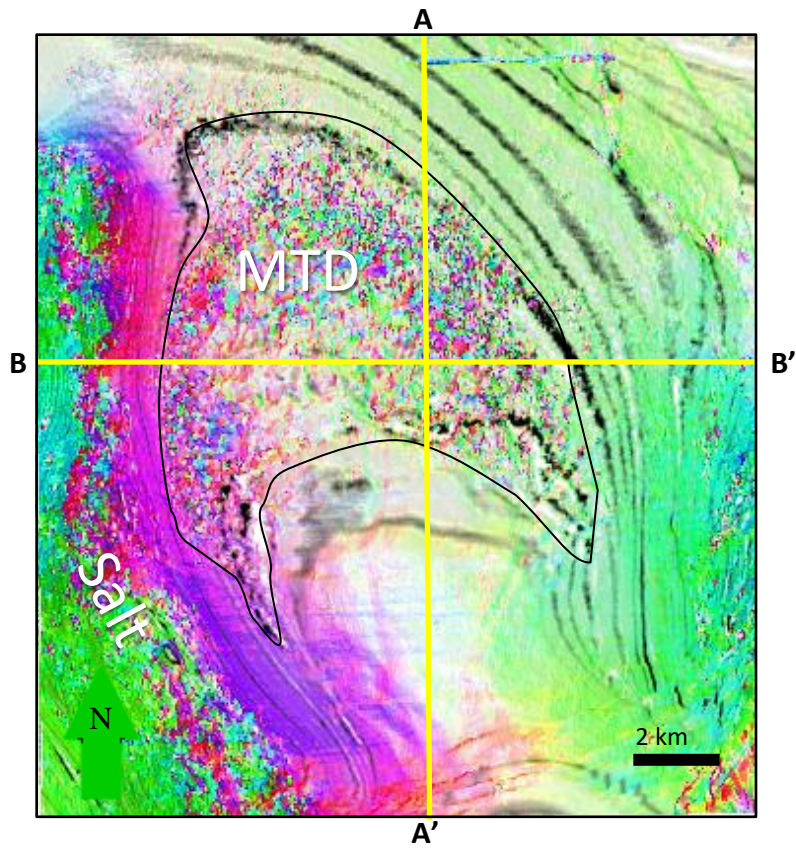
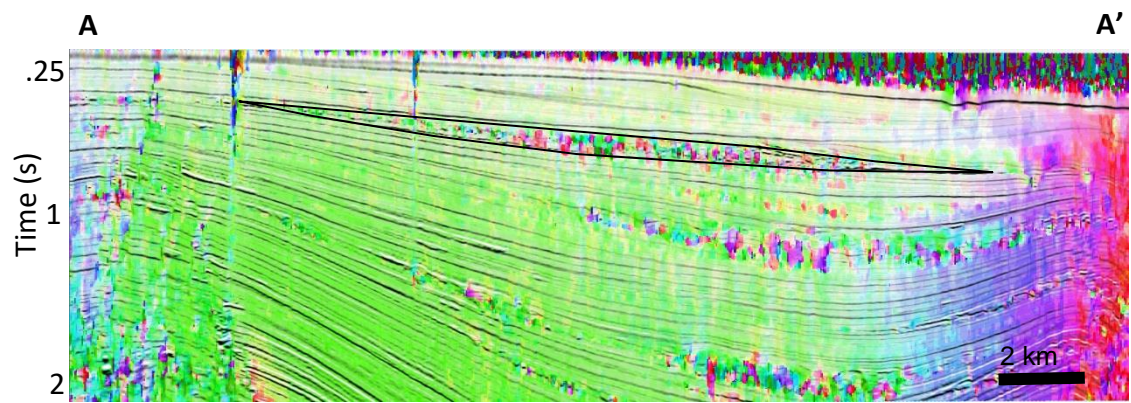


**Figure B1.** Co-rendered seismic amplitude and coherence seen on (a) a time slice at  $t=0.608$  s (b) along line A-A, and (c) along line B-B'. The MTD is highlighted by the black polygon. The MTD exhibits low coherence.

(a)



(b)



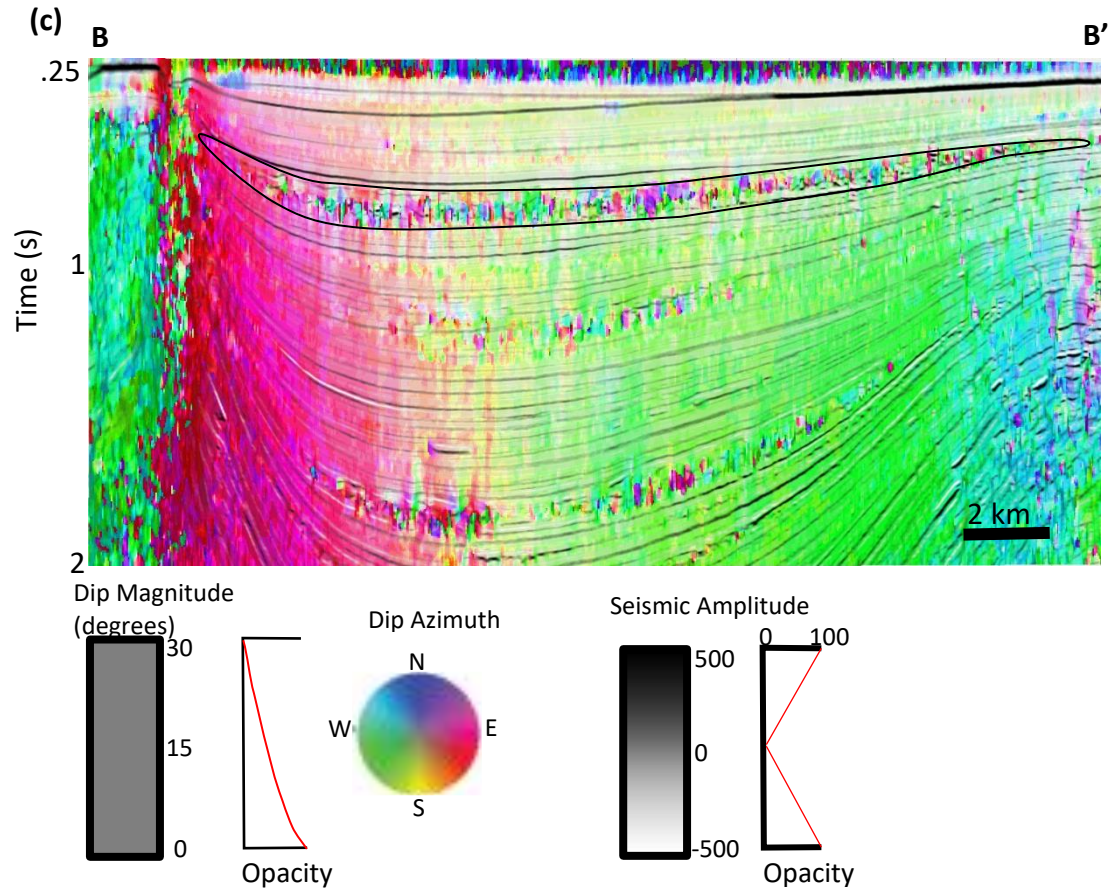
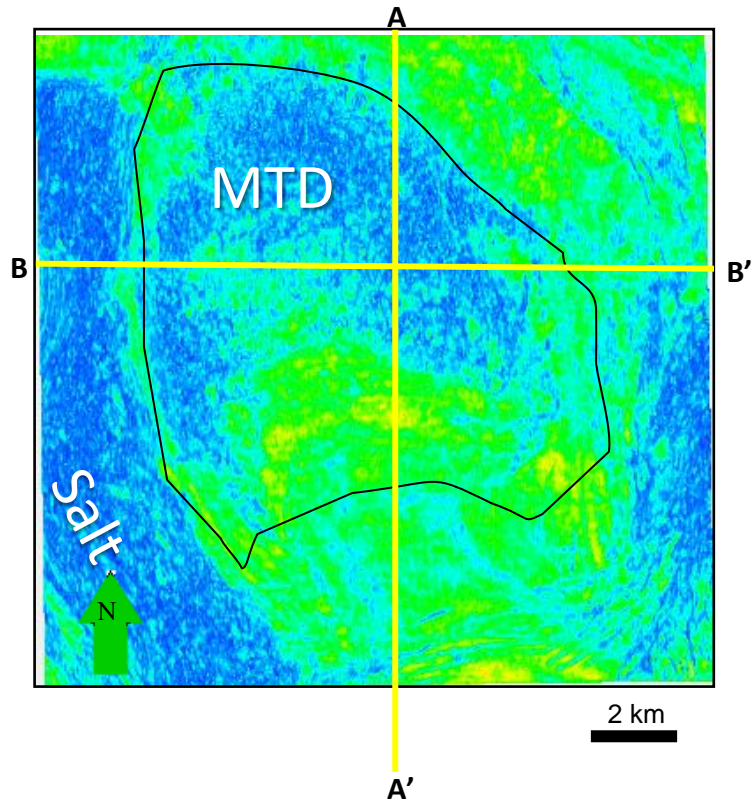


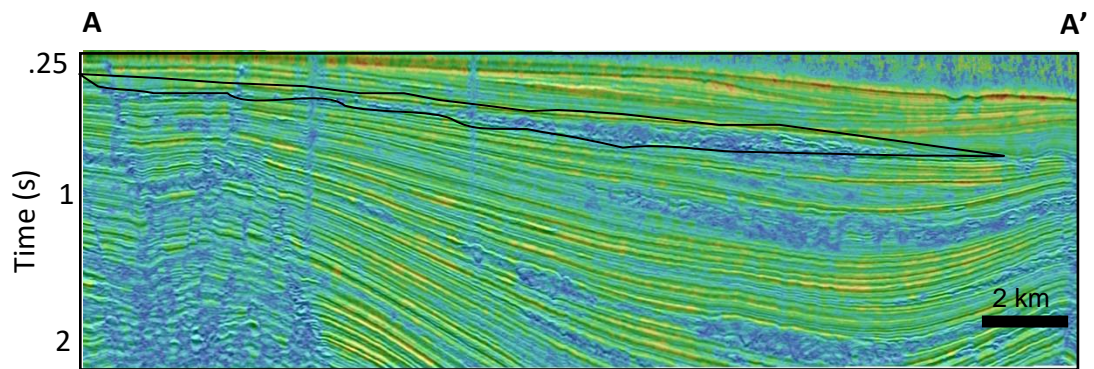
**Figure B2.** Co-rendered seismic amplitude dip azimuth and dip magnitude seen on (a) a time slice at  $t=0.608$  s (b) along line A-A, and (c) along line B-B'. The MTD is highlighted by the black polygon. The MTD exhibits variable dip azimuth response due to the large structural variability within the deposit.

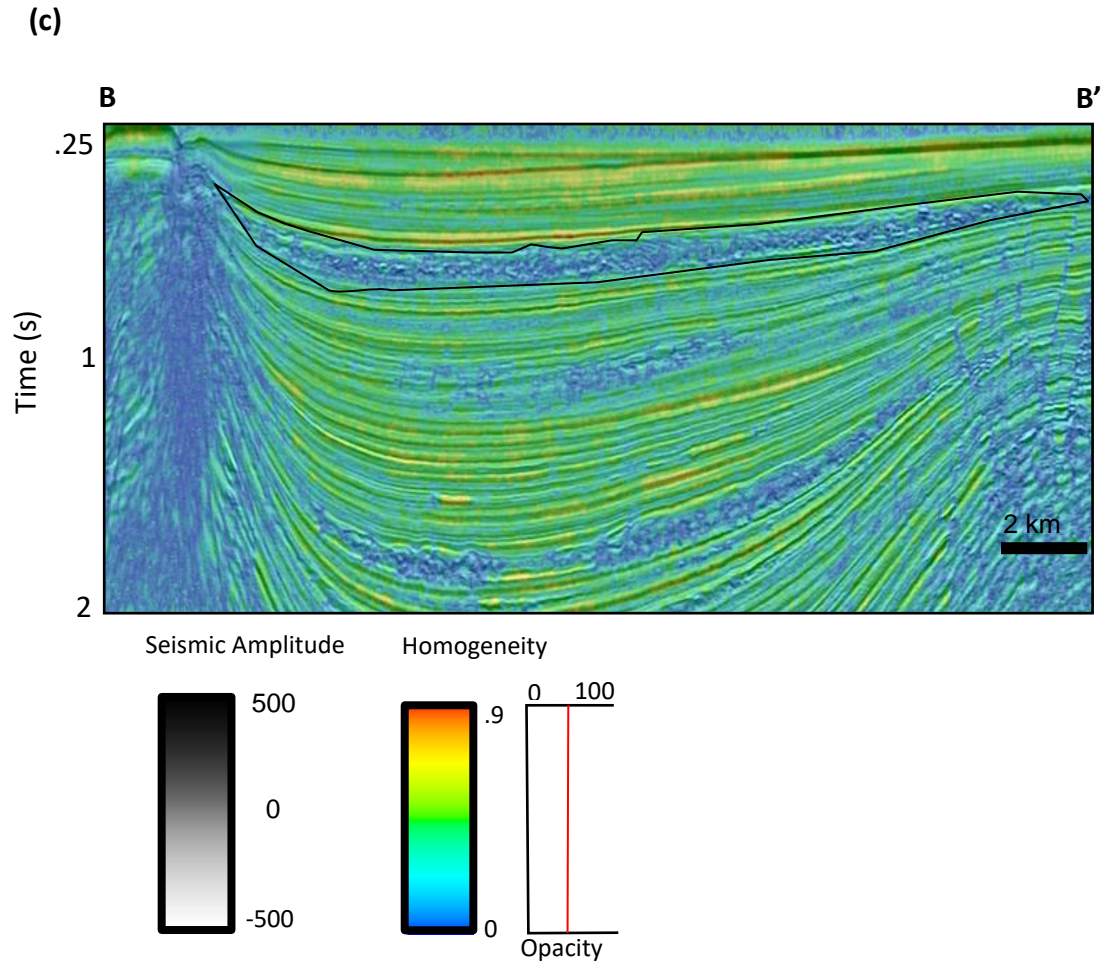


(a)

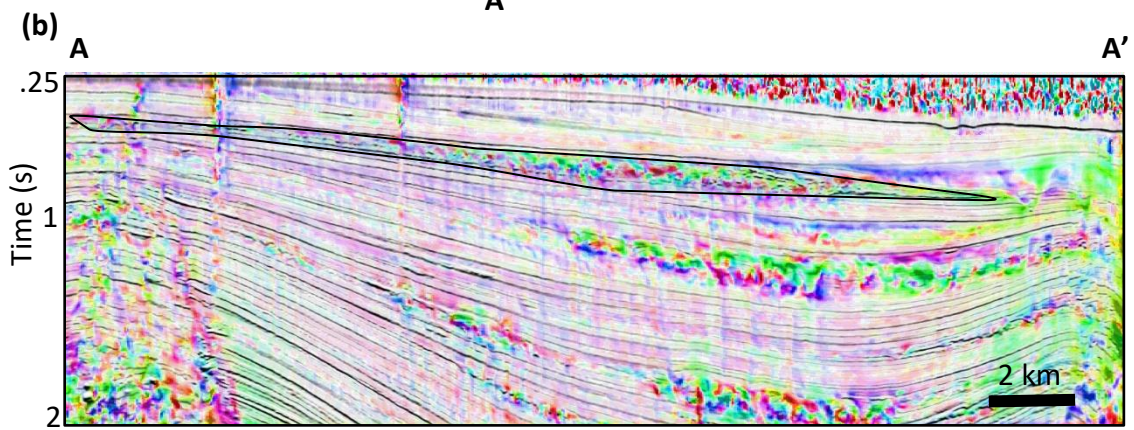
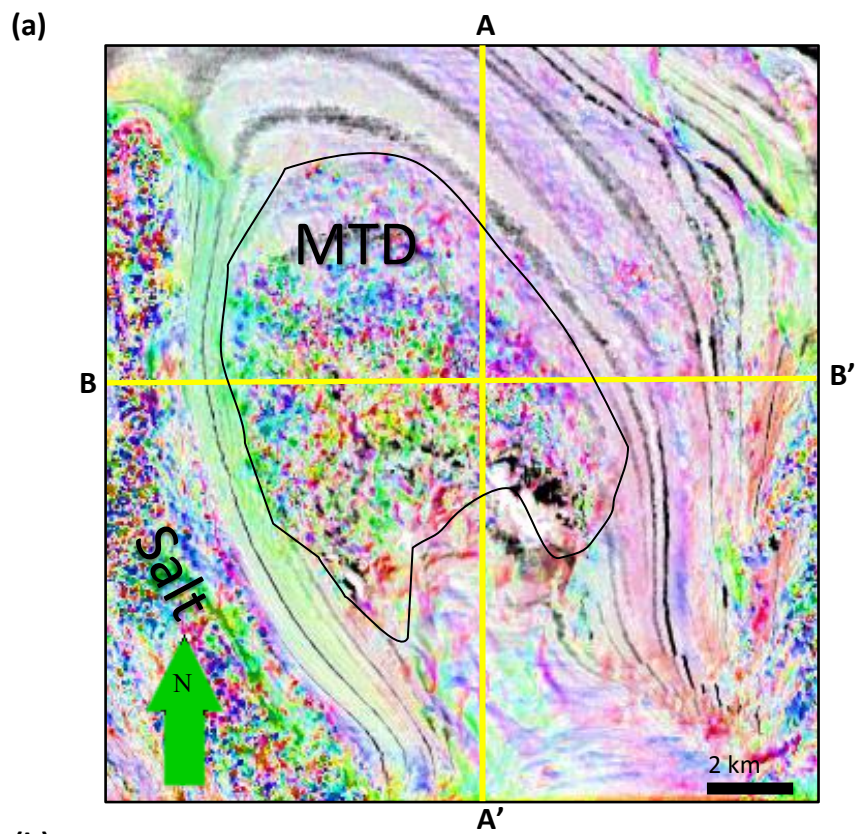


(b)

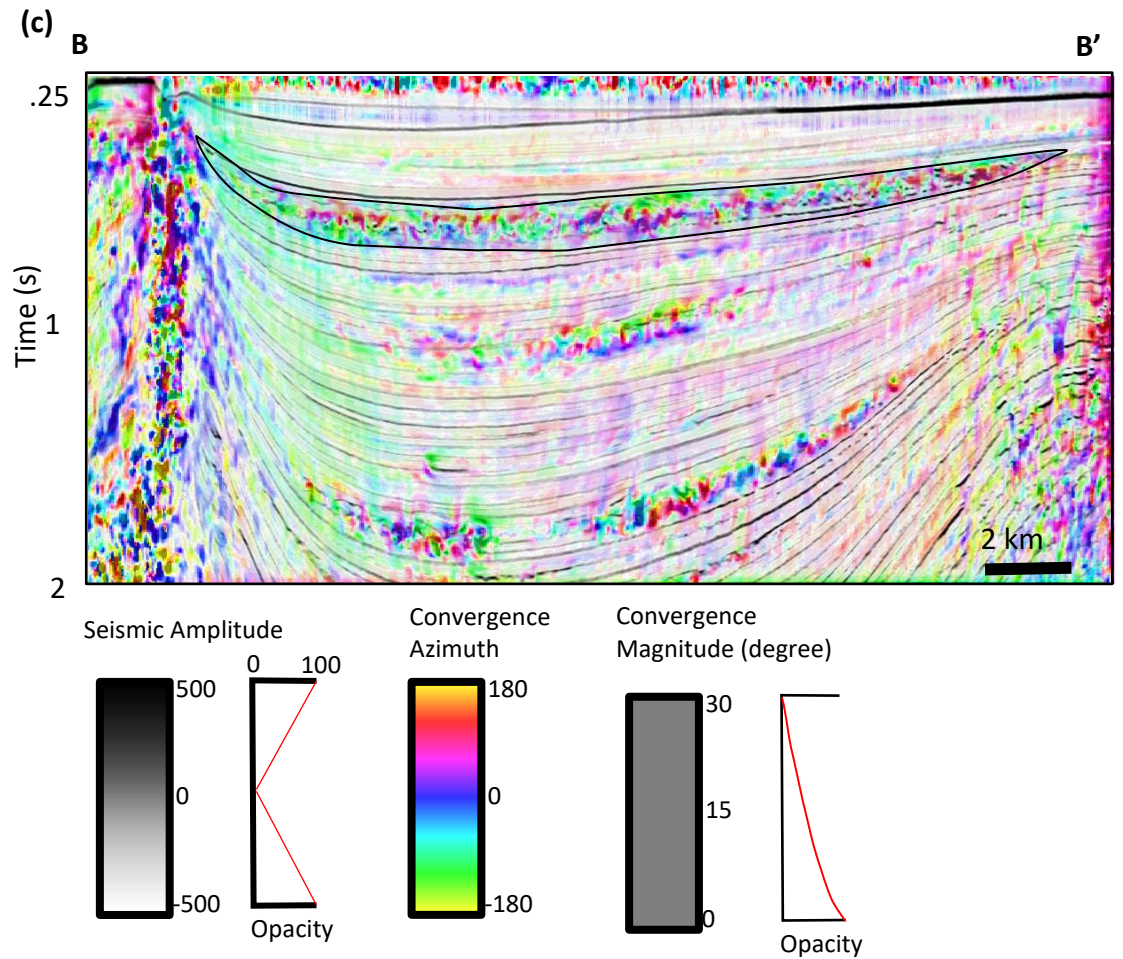




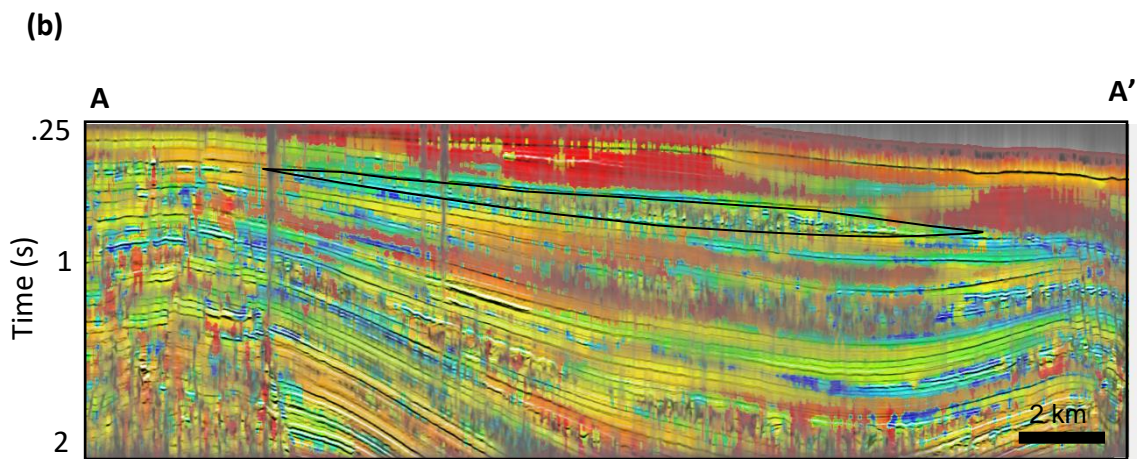
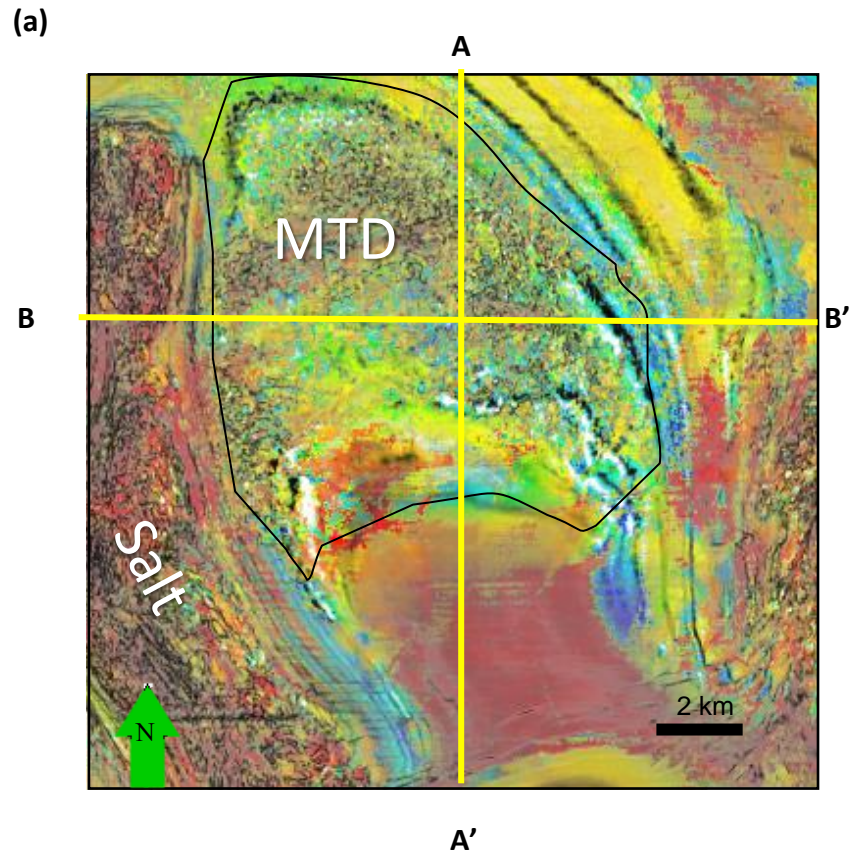
**Figure B3.** Co-rendered seismic amplitude and homogeneity seen on (a) a time slice at  $t=0.608$  s (b) along line A-A, and (c) along line B-B'. The MTD is highlighted by the black polygon. MTD displays low homogeneity values due to large variations of sediments and structure internal to the deposit.



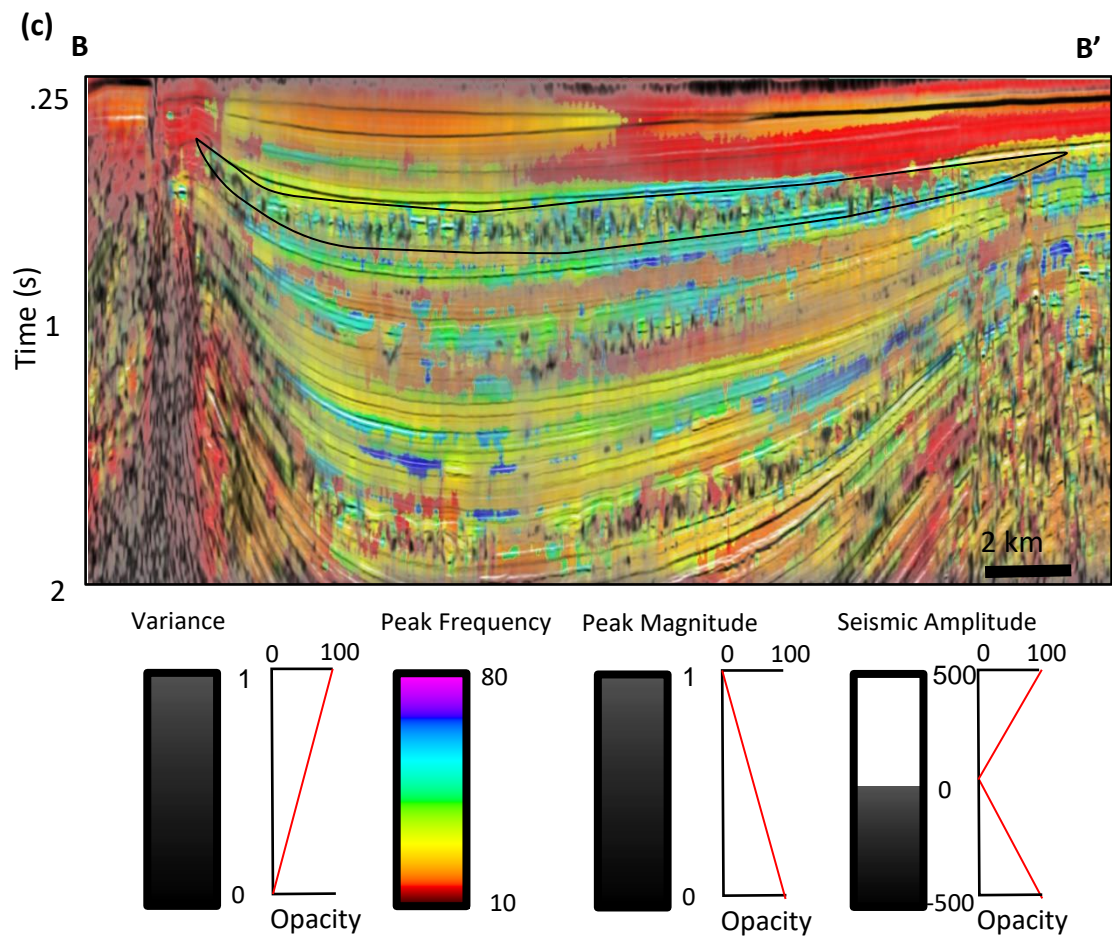




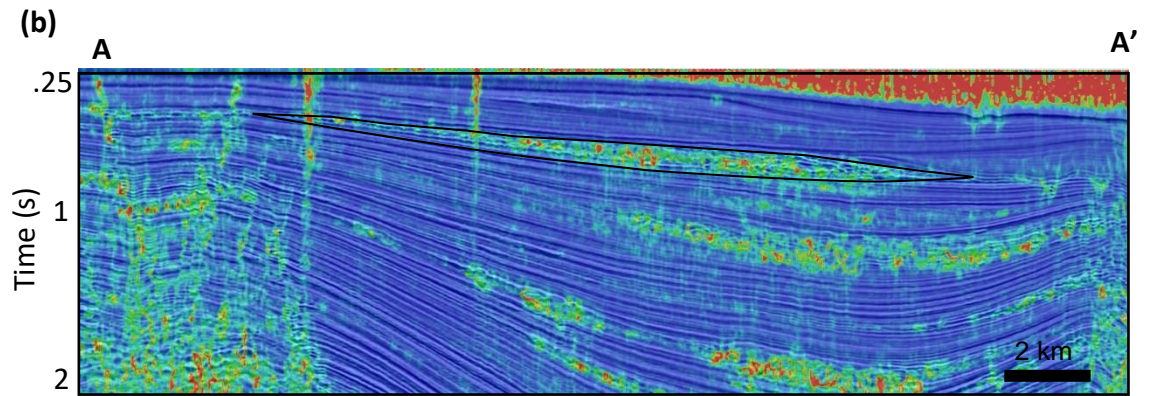
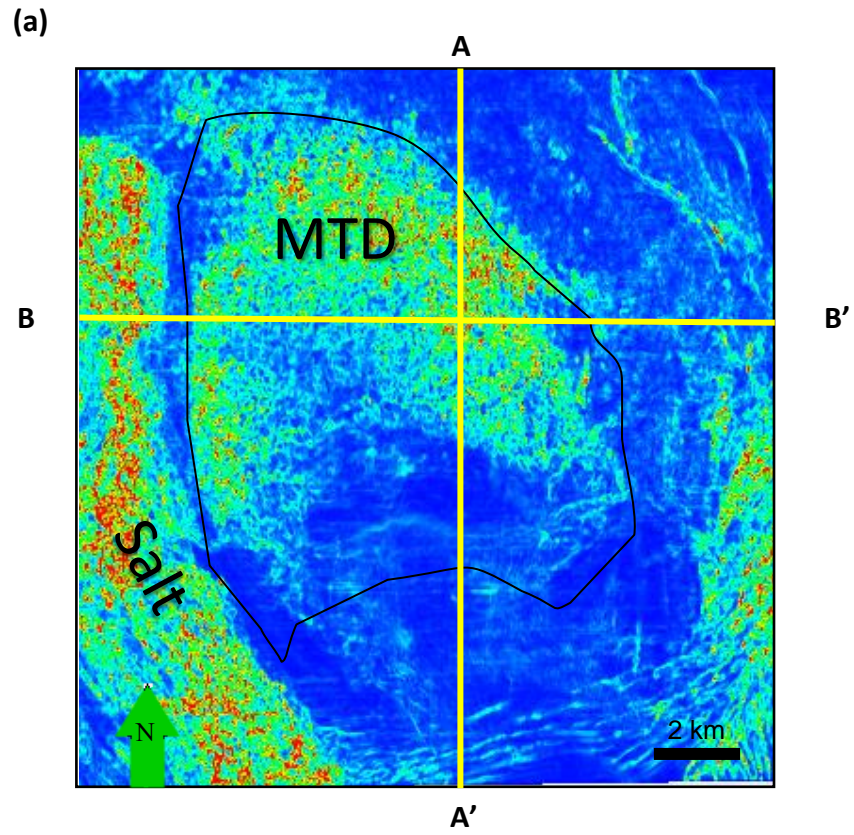
**Figure B4.** Co-rendered seismic amplitude, convergence azimuth and magnitude seen on (a) a time slice at  $t=0.608$  s (b) along line A-A, and (c) along line B-B'. The MTD is highlighted by the black polygon. The MTD, outline by the black polygon, displays variable convergence azimuth values due to the highly chaotic structures within the MTD.

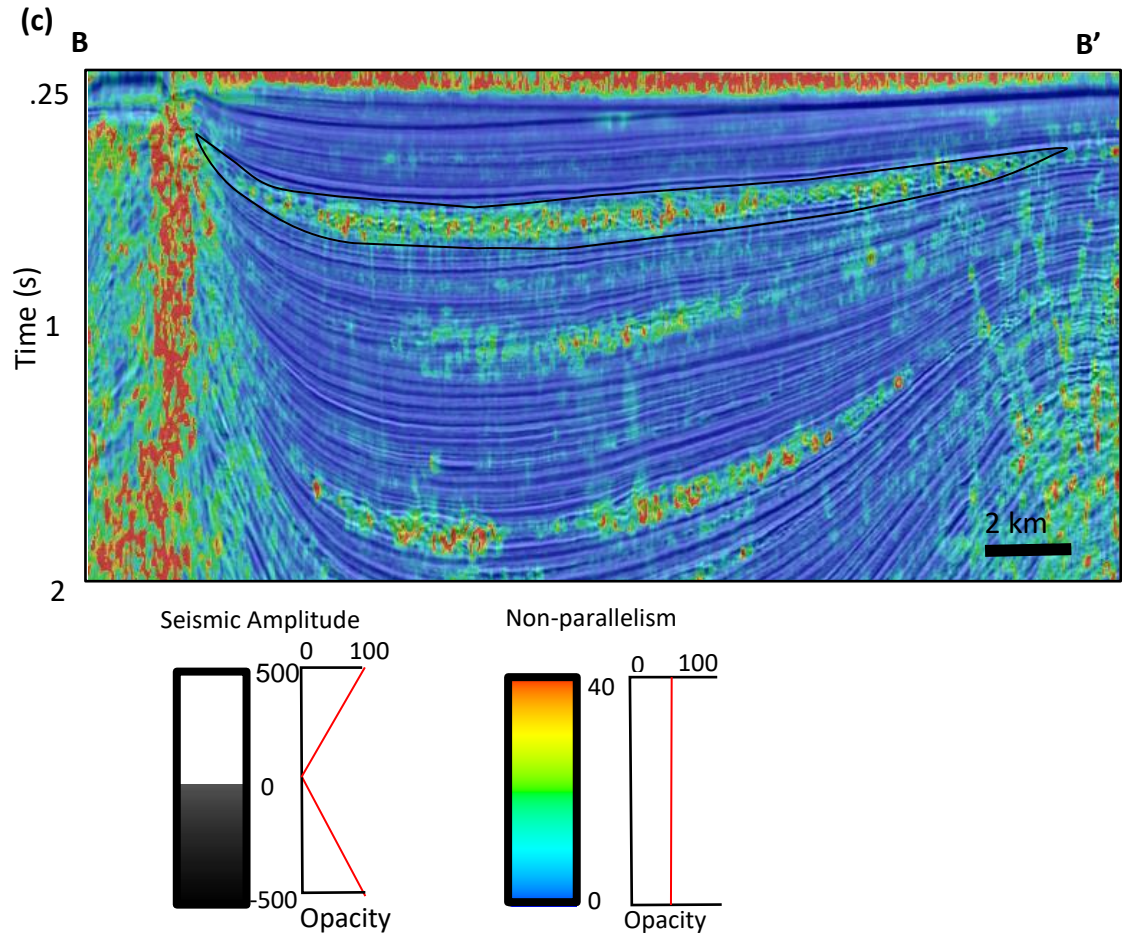






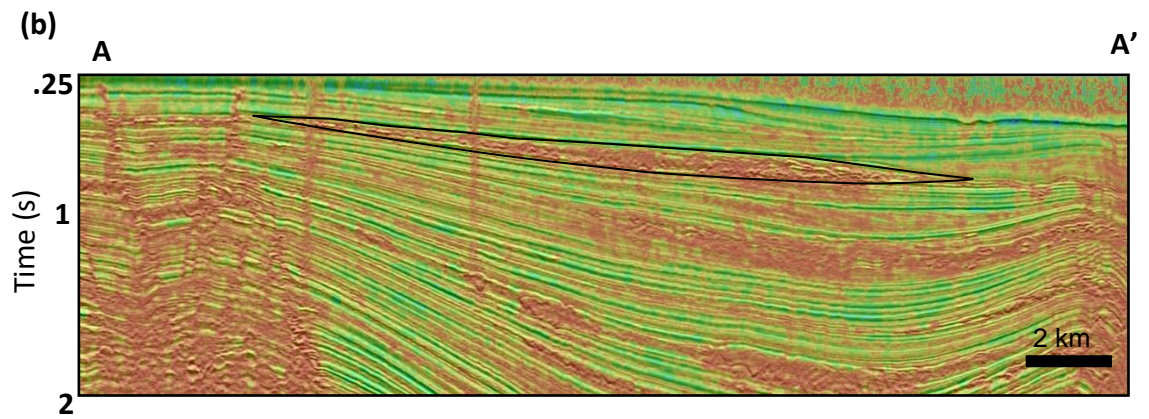
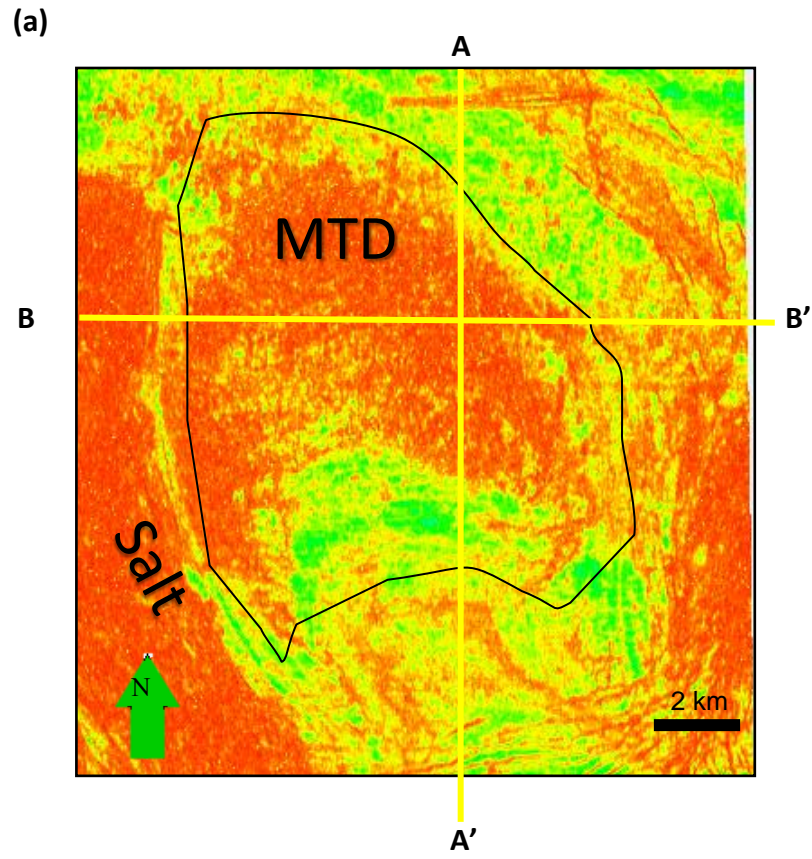
**Figure B5.** Co-rendered seismic amplitude, variance, peak frequency, peak magnitude seen on (a) a time slice at  $t=0.608$  s (b) along line A-A, and (c) along line B-B'. The MTD is highlighted by the black polygon. The MTD, outline by the black polygon, displays variable frequency responses that does not delineate the MTD from surrounding sediments.





**Figure B6.** Co-rendered seismic amplitude and non-parallelism seen on (a) a time slice at  $t=0.608$  s (b) along line A-A, and (c) along line B-B'. The MTD is highlighted by the black polygon. The MTD, outline by the black polygon, displays variable magnitude responses that does not delineate the MTD from surrounding sediments.





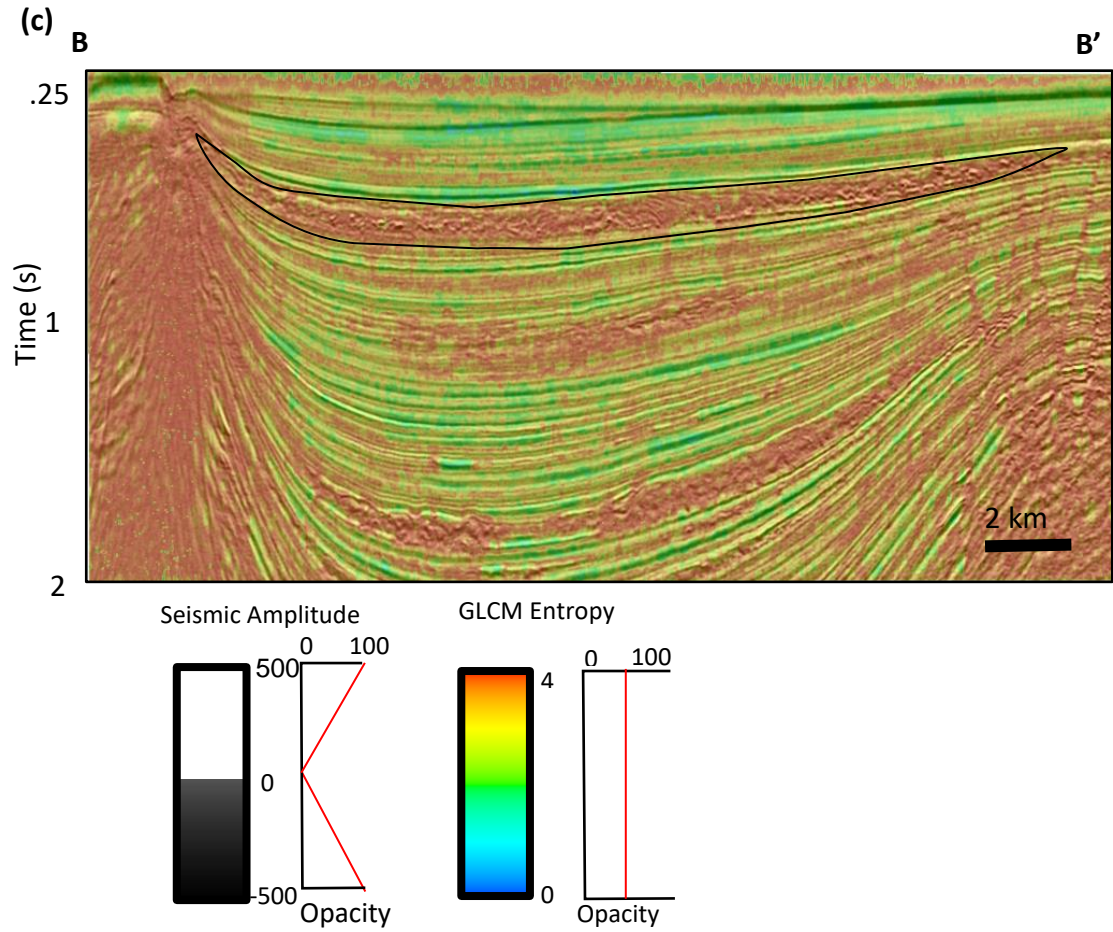
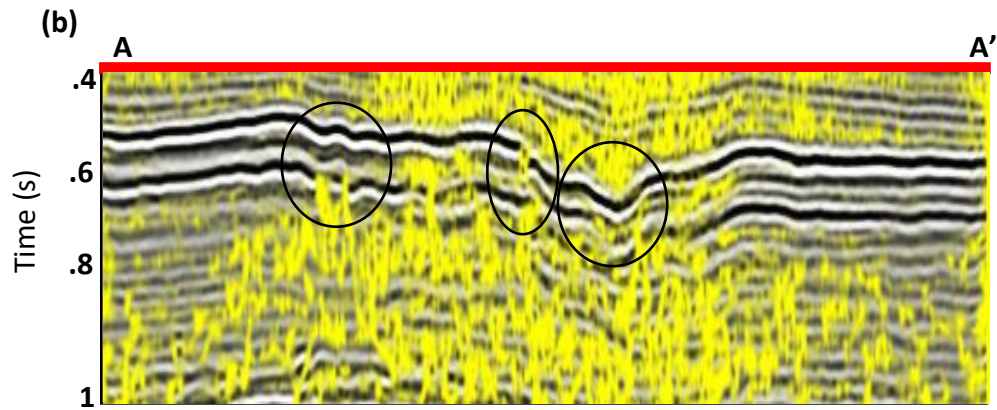
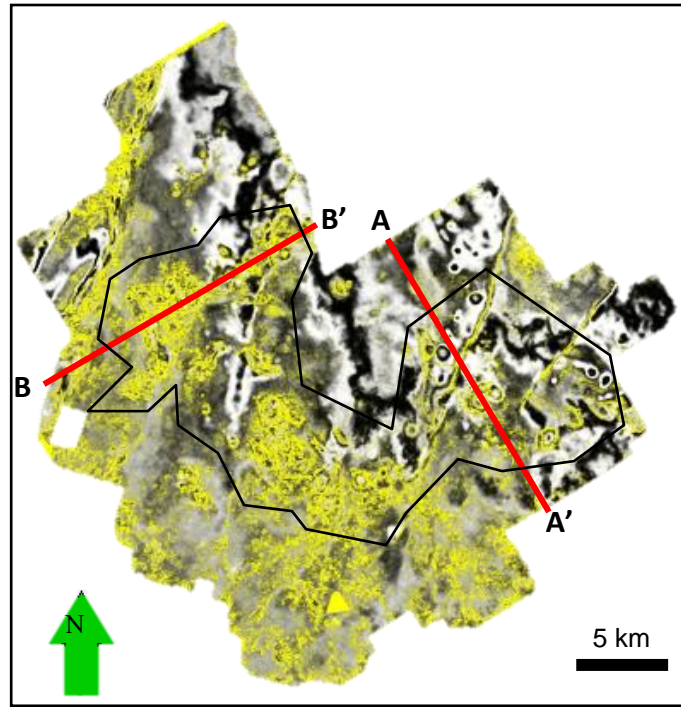


**Figure B7.** Co-rendered seismic amplitude and GLCM entropy seen on (a) a time slice at  $t=0.608$  s (b) along line A-A, and (c) along line B-B'. The MTD is highlighted by the black polygon. The MTD is characterized by the high entropic response due to variable internal structures.

## **Appendix C: Attribute Expression of Karst**

In this appendix I provide images of a Harris karsts for the suite of attributes listed in Table 5.

(a)





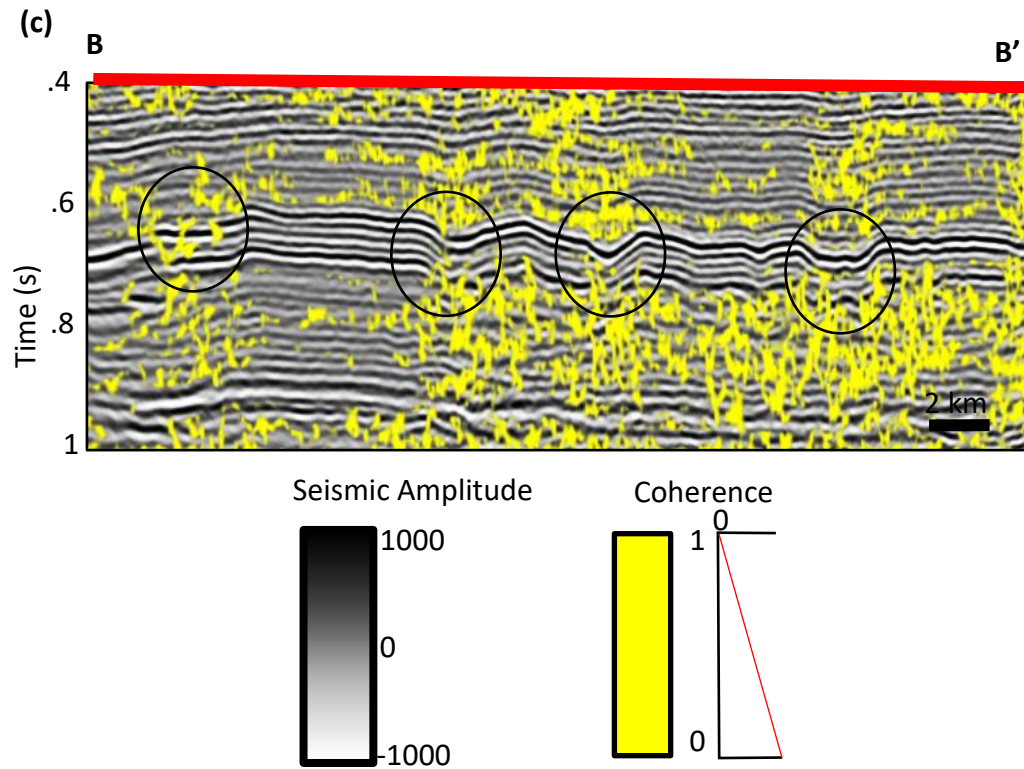
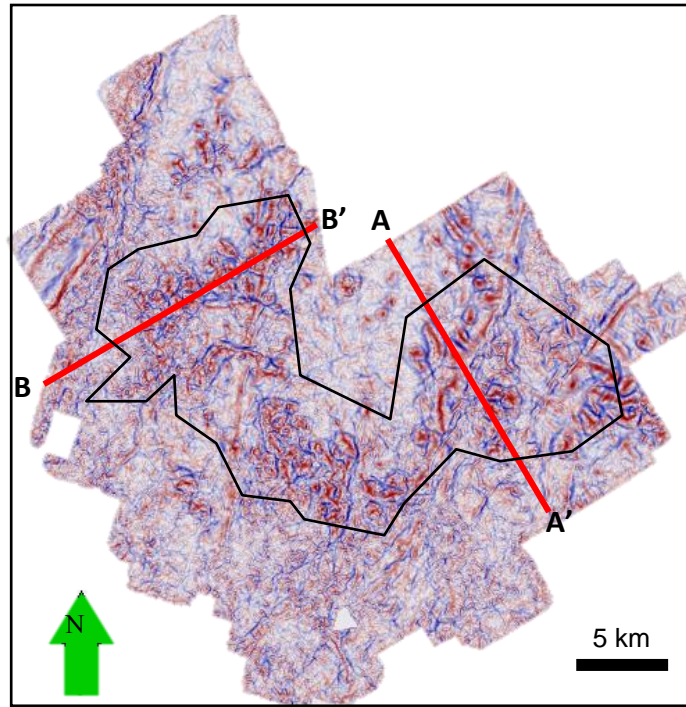


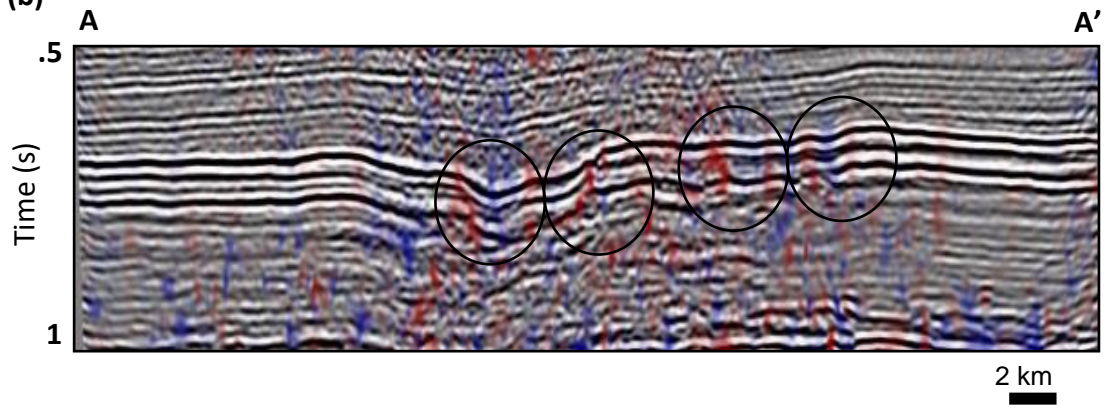
**Figure C1.** Co-rendered seismic amplitude and coherence seen on (a) a time slice at  $t=0.75$  s (b) along line A-A, and (c) along line B-B'. The karst is highlighted by the black polygon. The karst features, outline by the black polygon, displays low coherence responses due to the collapse structures and polygonal faults.



(a)



(b)



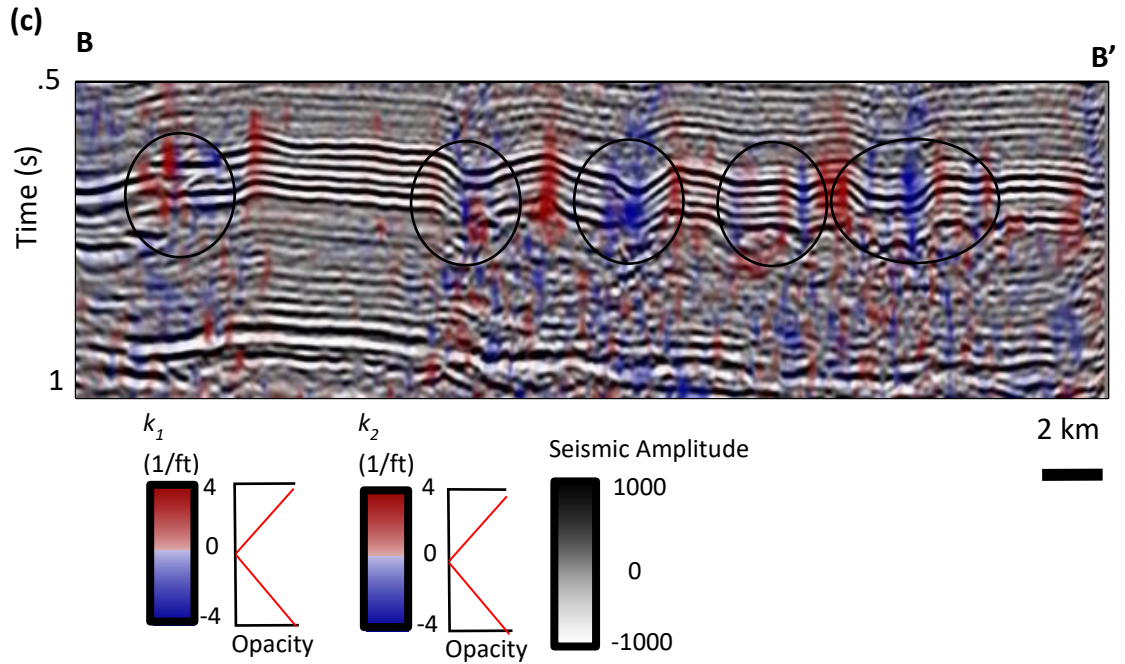
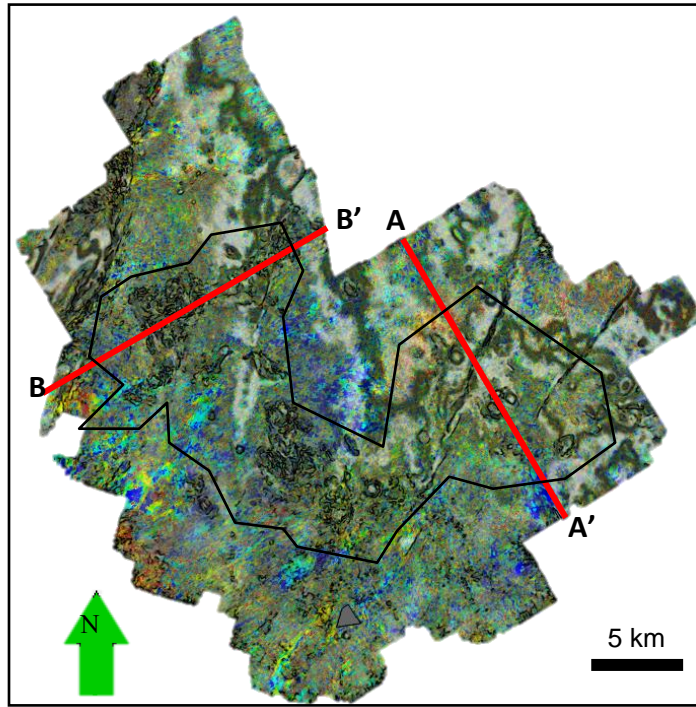
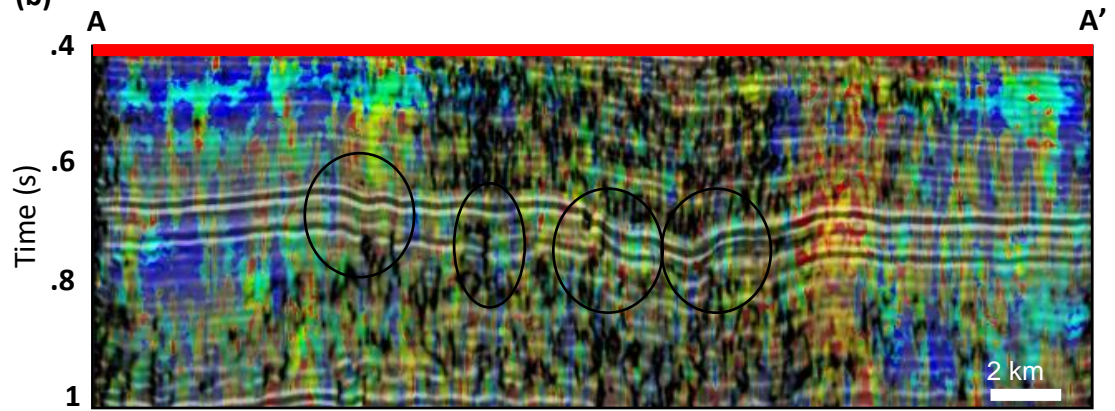


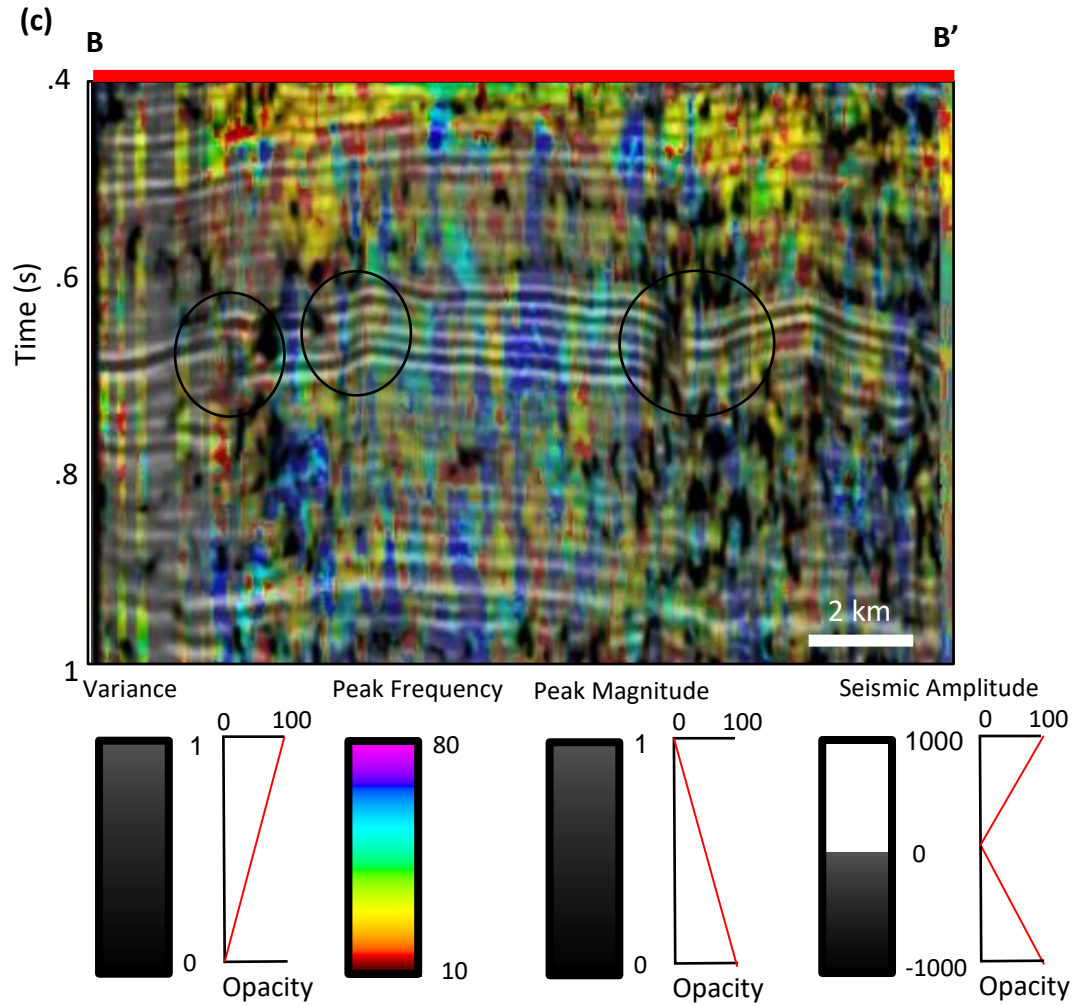
**Figure C2.** Co-rendered seismic amplitude  $k_1$  (most positive curvature) and  $k_2$  (most negative curvature) seen on (a) a time slice at  $t=0.608$  s (b) along line A-A, and (c) along line B-B'. The karst is highlighted by the black polygon. The karst features are highlighted by black circles. The curvature response in time shows high curvature values outside the collapse and low curvature values in the collapse features. The polygonal faults have a positive value on the up thrown side of the block and a negative value on the down thrown block.

(a)



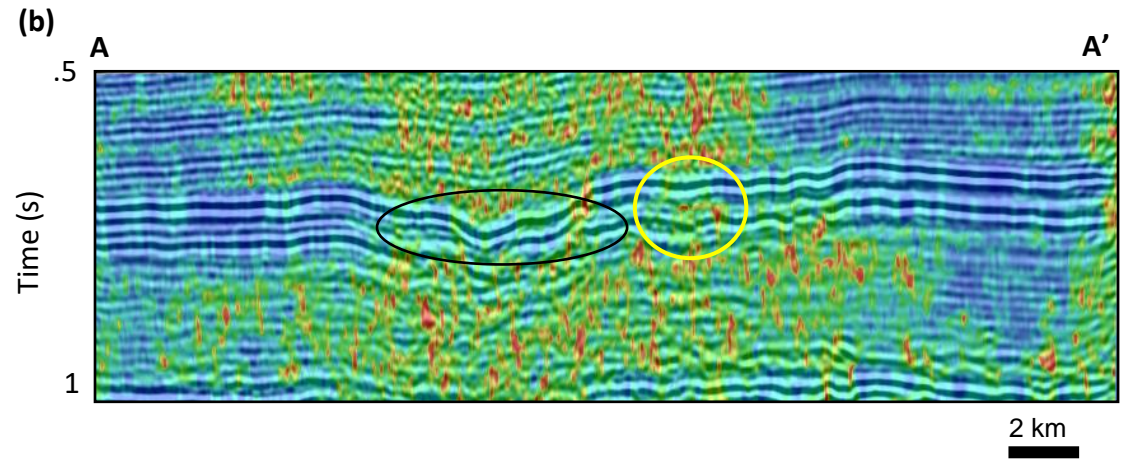
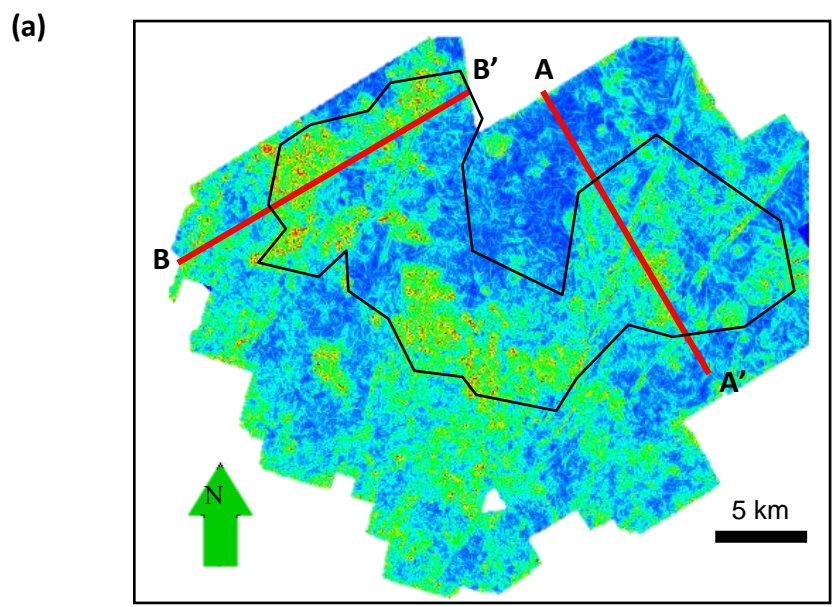
(b)

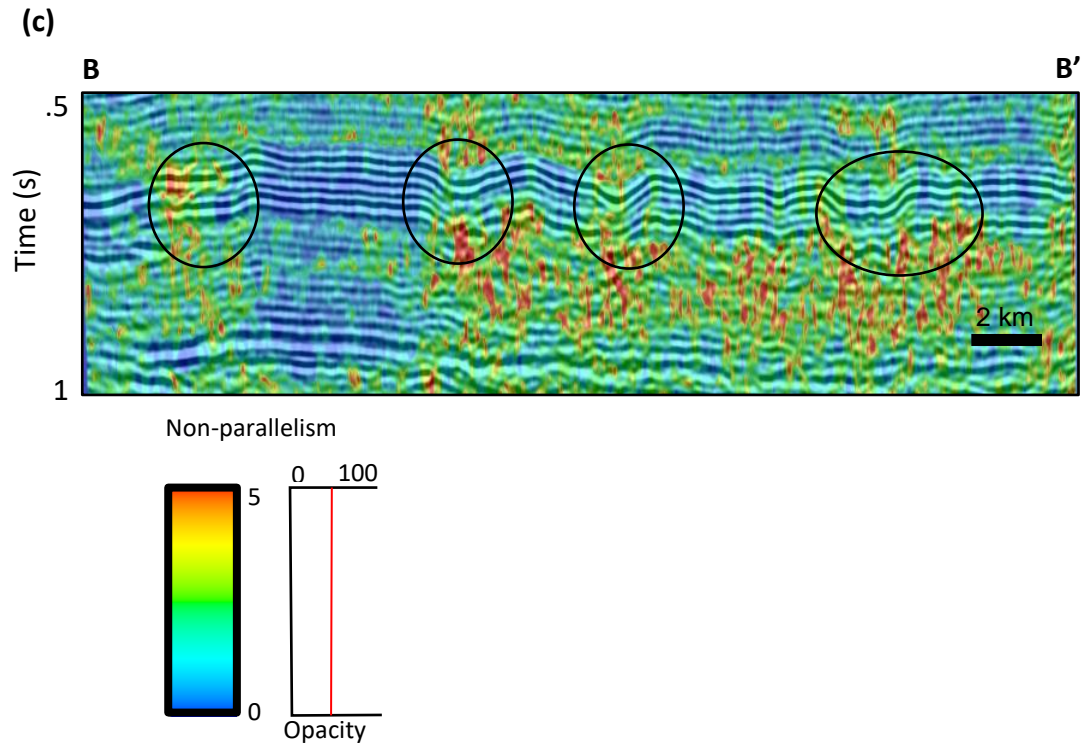




**Figure C3.** Co-rendered seismic amplitude, variance, peak frequency, peak magnitude seen on (a) Seismic time slice at  $t=0.75$  s. (b) A-A' cross-section. (c) B-B' cross-section. The karst features are highlighted by black circles. Karst display high variance responses as well as low frequency values

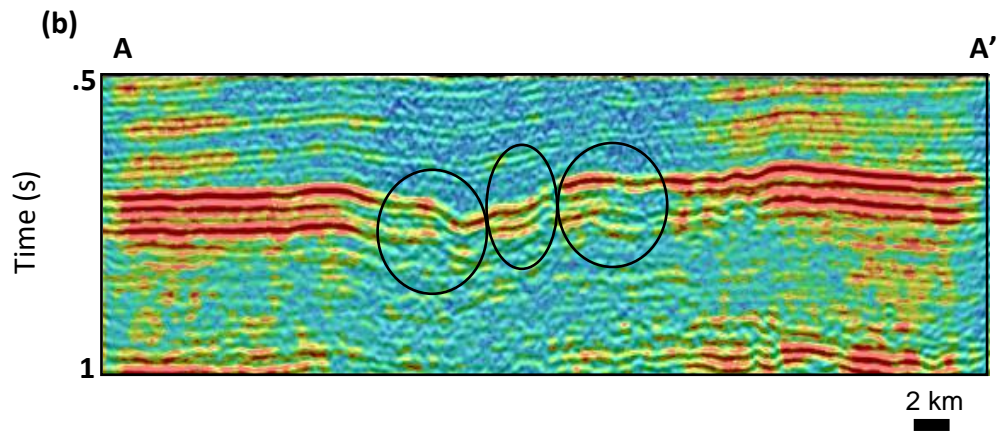
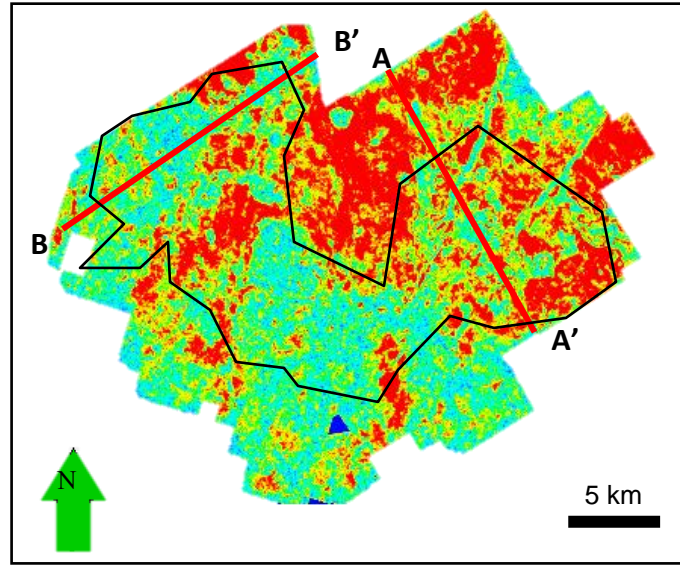


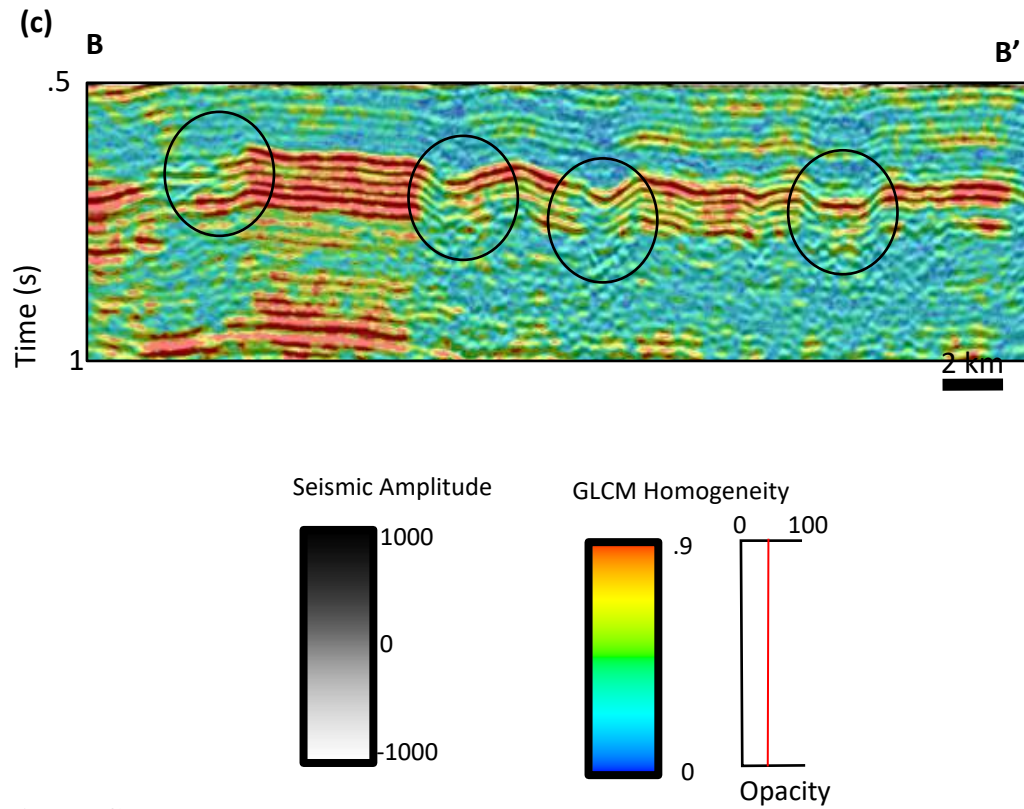




**Figure C4.** Co-rendered seismic amplitude and non-parallelism (a) Seismic time slice at  $t=0.75$  s. (b) A-A' cross-section. (c) B-B' cross-section. The karst features are highlighted by black circles and yellow circles. Karst collapse features, highlighted by the yellow circle, high non-parallel values while the layers surrounding, highlighted by black circles, are expressed as low values.

(a)

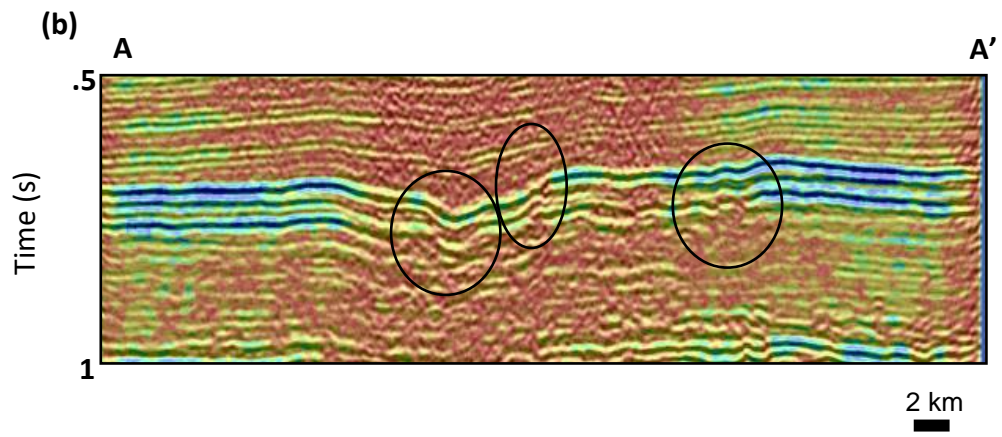
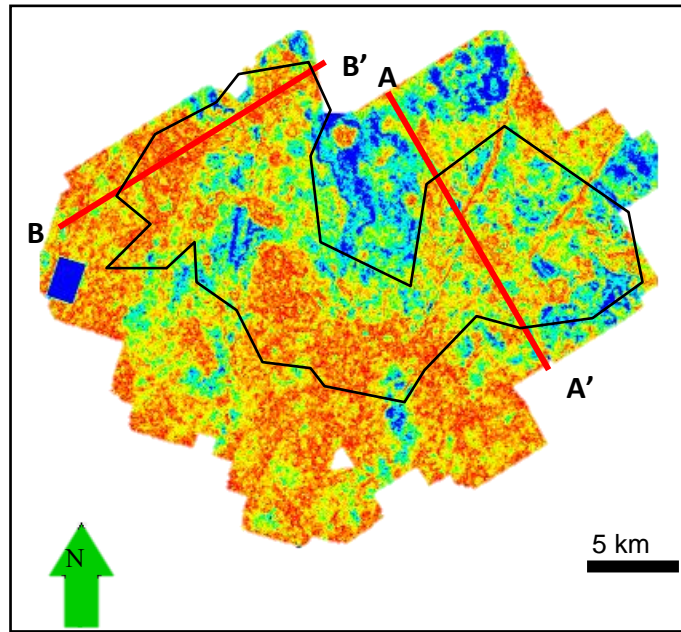




**Figure C5.** Co-rendered seismic amplitude and GLCM homogeneity (a) Seismic time slice at t=0.75 s. (b) A-A' cross-section. (c) B-B' cross-section. The karst features are highlighted by black circles. Karst collapse features exhibit low homogeneous values.



(a)



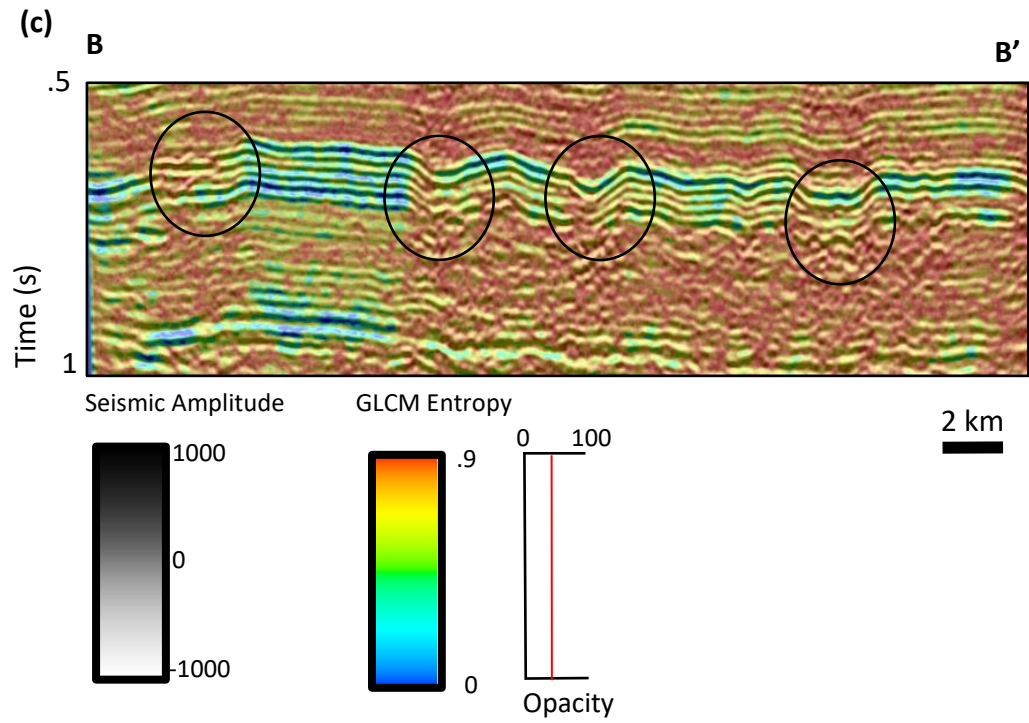


**Figure C6.** Co-rendered seismic amplitude and GLCM entropy (a) Seismic time slice at  $t=0.75$  s. (b) A-A' cross-section. (c) B-B' cross-section. The karst features are highlighted by black circles. Karst collapse features exhibit high entropic values.